



AUJUS

Auburn University Journal of Undergraduate Scholarship

Spring 2013 Volume 2

Effectiveness of Continuous-Catch
Doors for Removing Wild Pigs

Parameter Estimation and Simulation
Using Virtual Elevation Methods for
Race Cycling

The Trial of Euphame MacCalzean:
Female Inheritance and the Patriarchal
Society in the Scottish
Witch-Craze of 1590-1591

Pathoadaptive Variants of
Pseudomonas aeruginosa

AUJUS cover design image by Christine Zambetti.

Auburn University is an equal opportunity educational institution/employer.

AUJUS

Auburn University Journal of Undergraduate Scholarship

Table of Contents

Volume 2 • Spring 2013

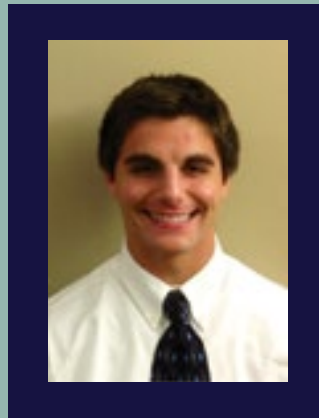
- 1 **Letters from Editors-in-Chief**
- 2 **Mentor of the Year: Dr. Martha Escobar**
Gabrielle Bates
- 3 **Identification of Endometrial Cell Compartment-specific Expression of Estrogen Receptor-alpha Using Multispectral Imaging and Digital Image Processing**
Kimberly E. Roberts, Meghan L. Davolt, Dori J. Miller, Anne A. Wiley, and Frank F. Bartol
- 8 **Parameter Estimation and Simulation Using Virtual Elevation Methods for Race Cycling**
William D. McGinnis
- 16 **The Trial of Euphame MacCalzean: Female Inheritance and the Patriarchal Society in the Scottish Witch-Craze of 1590-1591**
Yvette M. Jones and Adam J. Jortner
- 21 **Precision of the Neubauer Hemocytometer in Quantifying Concentration of Canine Spermatozoa Within and Between Operators of Differing Experience Levels**
Kaitlyn Caraway, Robyn Wilborn, Aime Johnson, Jay Barrett, and Todd Steury
- 26 **Frictional Properties of Ground Loblolly Pine Chips**
Jacob Wadkins, Anshu Shrestha, Oladiran Fasina, Sushil Adhikari, and Steven Taylor
- 32 **Pathoadaptive Variants of *Pseudomonas aeruginosa***
Heather C. Eggleston, Sarah B. Chaney, and Daniel J. Wozniak
- 37 **Comparison of Articular Cartilage Thickness in Cadaveric Equine Limbs**
W. Grant Kirkland, Ryan N. Whitmore, Hannah E. Young, A. J. Richardson, Robert L. Jackson, and R. Reid Hanson
- 42 **Microwave Effects Relevant to Antimatter Traps**
K. A. Niffenegger, P. H. Donnan, and F. Robicheaux
- 48 **Mapping Social Vulnerability for Earthquake Hazards in Salt Lake County, Utah**
Ryan Hile and Philip L. Chaney
- 54 **Effectiveness of Continuous-catch Doors for Removing Wild Pigs**
Trenton N. Smith and Mark D. Smith
- 59 **Generation of Liquid Fuel Microdroplets for Combustion Imaging**
Stephen Giles, Vignesh Venkatasubramanian, Jingran Duan, and Steve R. Duke
- 63 **Student Author Bios**
- 65 **Call for Submissions**

About the Editors

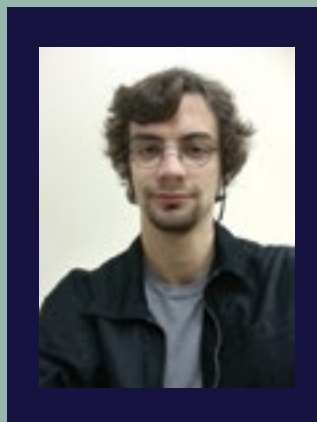
Robert Elrod is a junior studying Biomedical Sciences with a minor in English. His research focused on utilizing open source intelligence to track recent trends in the West Nile outbreak in the United States. In addition to his position for AUJUS, he currently serves as a Writing Consultant at the Miller Writing Center, as a Project Coordinator for the volunteer organization IMPACT, and as a member of the Junior Honor Society, Cardinal Key. Robert spent summer of 2012 studying English at Regent's College in London, and plans to attend medical school following graduation.



Hunter Hayes is a junior pursuing degrees in Business Administration in Finance and Accounting as well as Music in Piano Performance. Hunter has been involved on Auburn's campus in Omicron Delta Kappa Society, Lambda Sigma Honorary, College of Business Executive Society, Beta Gamma Sigma, Music Teachers National Association, and several other organizations. He also competes at the Varsity level for Auburn's Cross Country and Track and Field teams. Hunter will be doing his senior research on music literature and plans to continue his education in business, law, or music following graduation.



Stephen Giles is a senior studying Chemical Engineering. He is currently writing an undergraduate Honors thesis which explores combustion properties of alternative liquid fuel microdroplets. He is also working on the use of cellulose nanocrystal thin films for next-generation, low-cost microelectromechanical systems. He is a 2011-2012 Auburn University Undergraduate Research Fellow, a 2012 National Science Foundation Research Experiences for Undergraduates Fellow at Clemson University, and won 2nd place for a poster presentation at the 2012 American Institute of Chemical Engineers National Conference.



Katherine Hendrickson is a senior studying Mathematics, and is currently preparing a research article for publication on the issue of technocracy. She enjoys traveling and has participated in an Honors College Study Abroad trip to Costa Rica and taught an English as a Second Language children's camp in Spain. She stays busy on Auburn's campus with the AU Students for Life group and the AU Mathematics Club. Interested in finding new solutions to complex social problems, Katherine hopes to pursue a graduate degree and career in Operations Research.



Kimberly Roberts is a senior studying Animal Science. She is currently writing her undergraduate Honors thesis centered on her research on neonatal uterine development in pigs. She has participated in the AU Cellular and Molecular Biosciences Undergraduate Summer Research Scholars program, and won Best Undergraduate Poster at the 2012 AU Phi Zeta Research Emphasis Day. In addition to her research, she spent one month studying abroad in Belize, and is an Undergraduate Teaching Assistant for Anatomy and Physiology labs. Kimberly is looking forward to pursuing joint degrees in Veterinary Medicine and Public Health this coming year.



Erika Kolakowski is a junior studying Biomedical Sciences with a minor in Spanish language. In addition to her role with AUJUS, she is active in veterinary medical research studying bleeding disorders in dogs. She has served as the captain of the Auburn Cross Country team for two years and has competed on the Track and Field team. She is a member of Alpha Epsilon Delta Pre-Health Organization and Sigma Delta Pi National Spanish Honor Society. Erika aspires to continue her education by attending medical school with the goal of specializing in internal medicine.



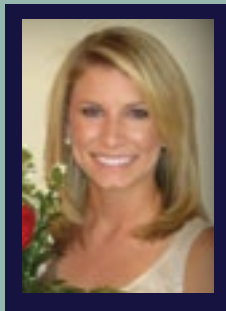
Casey Ruark is a senior pursuing a Molecular Biology degree. Her primary research interests concern plant-pathogen interactions. She has held internships at HudsonAlpha Institute for Biotechnology and NC State University, as well as an AU Undergraduate Research Fellowship. Since her freshman year at Auburn, Casey has had extensive research experience involving bacteria, viruses, fungi, and nematodes. She is also a member of Phi Kappa Phi Honor Society and has been a peer instructor for the Microbiology Learning Community. Casey's future plans involve pursuing a doctorate in Molecular Plant Pathology.



Production Team



Erin Albright, Junior
Graphic Designer



Olivia Sprunger, Senior
Graphic Designer

AUJUS Advisory Board

David Carter, Associate Professor, History

Donald Conner, Professor and Head,
Poultry Science

Dafni Green, Advisor, Student Affairs

Ross Heck, Professor,
Graphic Design

Jay Lamar, Director,
Special Projects for Undergraduate Studies

Amy Hecht Macchio, Assistant Vice
President, Student Affairs

Bonnie MacEwan, Dean, Libraries

Carl Pinkert, Associate Vice President
for Research

Dean Schwartz, Associate Professor,
Anatomy, Physiology and Pharmacy

AUJUS Editors-in-Chief

Margaret Marshall, Director of
University Writing

Lorraine W. Wolf, Director of
Undergraduate Research

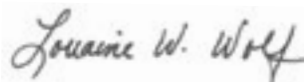
Letter from **AUJUS** Editors-in-Chief

As experienced researchers know, “systematic investigation or inquiry aimed at contributing knowledge by careful consideration, observation, or study of a subject” is incomplete if the results of that investigation are not subjected to rigorous review by experts in the field and then made public. The *Auburn University Journal of Undergraduate Scholarship (AUJUS)* provides an opportunity for undergraduate students to participate in that full cycle of presenting their work for review and, when successful, sharing their work with a public audience.

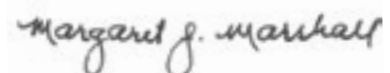
Such a publication could not exist without the many faculty members who mentored the undergraduate researchers throughout the process, the reviewers who read and commented on submissions, the student authors who revised and thereby improved the presentation of their work for a general audience, the student associate editors who managed this process, and the graphic design team who produced the final layout and journal design. We believe the selected articles clearly demonstrate that undergraduate students can make original and important scholarly contributions to their disciplines. We also believe that all of the student authors who submitted their work for consideration gained valuable experience and a deeper understanding of the research process.

Though this second edition of *AUJUS* showcases only a small fraction of the research done by undergraduate students and their faculty mentors, we trust others in the Auburn community will join us in applauding the extraordinary potential of Auburn students and this demonstration of their intellectual accomplishments.

We welcome students of all disciplines to contribute their original research and creative scholarship for consideration for our next issue, and we ask those who are interested in serving as student associate editors or submissions reviewers to contact us. We look forward to seeing what the third issue of *AUJUS* will teach us.



Lorraine W. Wolf
Director of Undergraduate Research
Professor of Geophysics



Margaret J. Marshall
Director of University Writing
Professor of English

An Interview with Dr. Martha Escobar, Recipient of the 2012 Provost's Award For Faculty Excellence in Fostering Undergraduate Research and Creative Scholarship

Gabrielle Bates

Dr. Martha Escobar received her Ph.D. in Cognitive and Behavioral Sciences from the State University of New York (SUNY) at Binghamton. She is now a Lanier Associate Professor of Comparative Psychology and the Director of the Animal Learning and the Human Learning and Memory laboratories in the College of Liberal Arts at Auburn University. She has been an undergraduate research fellow mentor for ten years.

1. What drew you to the field of comparative psychology?

I think every child is curious, but I grew up with a mother who was a chemist and a father who was a mathematician, so there was very little option. I also loved animals, but I didn't want to be a vet. One day, I saw a movie where they were teaching space chimps sign language. From that moment on, I knew I had to be a psychologist, so I could figure out whether or not animals think the way I think.

You can find inspiration in the most random places. For example, I used to have a parrot, and he would repeat what I said. I would wonder, "Does he understand what he's saying? Do words mean the same thing to him that they mean to me?" It's those sort of questions that lead you to comparative psychology.

2. What kind of research do you do here at Auburn?

In our comparative psychology experiments here at Auburn, we use rats, mice, and some invertebrates to try to see the generality of certain processes. Specifically, we are interested in fear: how it is acquired, how it is maintained, and how we can get rid of fear learning. We can do that more easily with animals than with humans. We're not traumatizing them, but we can control the situations better. Once we do it with the animals, we can try to generalize the results to other species.

3. How do you test fear?

First, we train the rats to press a lever to get little drops of water. They learn this quickly. Then we expose them to a sound they have never heard before, which is followed by a very mild electrical stimulus. This stimulus isn't painful, but it is unexpected, so it scares them. The rodents then

associate the sound with the stimulus. Rodents respond to fear by freezing, so we can measure how afraid they are by measuring how long they go without pressing the lever.

4. How long have you been involved in undergraduate research?

Since graduate school. My program required the graduate students to conduct research and train undergraduates to assist with that research, so when I came to Auburn, it seemed natural to continue that process.

5. What do you derive from your involvement with undergraduate research?

The undergraduates give me a fresh perspective. Sometimes we get so wrapped up in the technical aspects of what we're doing that we forget that we need to be able to communicate. Getting a new group of undergraduates forces us to stop for a minute and evaluate whether or not what we are doing makes sense. They all come from such different backgrounds, and they all have something new to contribute. A lot of them become independent after a while, and there's a lot that you can delegate on them.

It's extremely satisfying to start with a young person who does not know anything more than "I would like to do something," and then by the end they are doing things independently and are able to go to a conference and talk to famous people in the field about what they're doing. It's also a source of pride to see how successful they become after they leave here. What I do doesn't make sense if I don't train other people to continue it.

6. What do the undergraduates get out of their involvement with research?

What I hope they get is the capacity to see the things around them, ask questions, and find answers, regardless of what field they go into. Many of my students will not end up doing what I do; they will go on to different careers, but that capacity to be curious is the skill that they should have and that they will benefit from having. I think they get that. I hope they get that.

I stay in contact with most of them after they graduate. Every once in a while I will get a call from someone telling me that what they are doing in graduate school is similar to something that we did here. Or they will tell me that they had an interview, and their potential employer was impressed by the fact that they could talk about the research they did, discuss what it meant, and translate it to something else.

7. How much of a say do the undergraduates have in the research process?

I have had students who come up with interesting twists to what we're doing or their own idea for what they would like to do. These ideas are usually very green, and in most cases their ideas have to do with what we are already doing just because that's what they have been exposed to, but we definitely work with their ideas. By all means the undergraduates are collaborators in the research, but ultimately their roles depend on what the particular undergraduate wants to achieve.

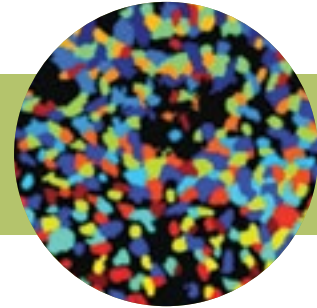
8. How are the undergraduate research fellows different than the other undergraduate research assistants?

I have had several undergraduate research fellows, and in most cases we start with an idea that I propose to them, and then they have to develop it. It becomes their project, and they are the ones who come up with the modifications to the procedure. They are the ones who are interacting with the animals, for example, so they come with their observations and say "I think what we need to do is this."

I have more expectations for the fellows. They have supervision, but essentially the independent research project is theirs. The fellows have to learn how to do literature research, be able to understand all aspects of the research design, learn how to do any sort of equipment programming, test their subjects, and they need to be able to do all of this semi-independently. Then they are expected to present their results at a conference or in writing. They get a stipend to do the research, so I want their time invested wisely.

Identification of Endometrial Cell Compartment-specific Expression of Estrogen Receptor-alpha Using Multispectral Imaging and Digital Image Processing

Kimberly E. Roberts, Meghan L. Davolt, Dori J. Miller, Anne A. Wiley, Frank F. Bartol



ABSTRACT

In the pig (*Sus scrofa domestica*), as in other mammals, uterine development is incomplete at birth (postnatal day = PND 0) and continues postnatally with formation of endometrial glands, or adenogenesis. Uterine endometrium is composed of three cell types including luminal epithelium (LE), glandular epithelium (GE), and stroma (ST). Supported by stromal-epithelial interactions, adenogenesis occurs as GE differentiates from LE and proliferates into underlying stroma. In the pig, adenogenesis is an estrogen-sensitive, estrogen receptor-alpha (ESR1)-dependent process initiated by PND 1. Disruption of adenogenesis can compromise adult uterine function. Understanding endometrial cell compartment-specific ESR1 expression will provide insight into mechanisms driving adenogenesis. Expression of ESR1 can be quantified *in situ* using immunofluorescence (IF), multispectral imaging (MSI) and digital image processing (DIP). Here, objectives were to establish a protocol for: (1) DIP-based identification of endometrial cell compartments (GE, LE and ST) using cytokeratin-8 (CK8) as a marker of epithelium (LE + GE) and ESR1 as a specific marker of nascent GE, and (2) evaluation of cell compartment-specific ESR1 expression. Uterine tissue sections

from one PND 5 gilt were fluorescently stained for ESR1, CK8 and cell nuclei. Images, obtained by MSI, were analyzed using CellProfiler™ and CellProfiler™ Analyst. Quantitative data were subjected to analyses of variance. Procedures enabled DIP-based identification of all three endometrial cell compartments. ESR1 expression levels were higher ($P < 0.001$) in epithelium than in stroma and, for epithelium, both ESR1 expression and labeling index (percent ESR1-positive cells) were higher ($P < 0.001$) in GE than in LE. Procedures enabled cell compartment-specific evaluation of endometrial morphoregulatory gene expression *in situ*.

INTRODUCTION

The neonatal porcine uterus is incompletely developed at birth (postnatal day = PND 0), lacking endometrial glands (Bartol et al., 1993). In adult mammals, including the pig, endometrial glands secrete uterine milk, also called histotroph (Gray et al., 2001). Secretions of endometrial glands include a mixture of proteins vital to the establishment and maintenance of pregnancy in all eutherian mammals (Gray et al., 2001). Failure of proper uterine gland development can compromise reproductive performance in adulthood leading, in some cases, to infertility (Bartol et al., 2006; Bartol

et al., 1999; Cooke et al., 2012). Thus, the course of uterine gland development, or adenogenesis, determines both the structural integrity and functional capacity of adult uterine tissues.

The endometrium, or uterine mucosa, consists of epithelium and stroma, two distinct cell compartments. Success of adenogenesis depends upon communication between these cell compartments (Kurita et al., 2001). In order to advance understanding of mechanisms regulating adenogenesis, roles of epithelium and stroma (ST) must be defined. In the porcine neonate, adenogenesis is an estrogen receptor-alpha (ESR1)-dependent process and, as in other mammals, occurs as glandular epithelium (GE) differentiates from luminal epithelium (LE) shortly after birth (Bazer, 2012; Park et al., 2012; Tarleton et al., 1999). Patterns of ESR1 expression indicative of adenogenesis in the porcine endometrium have been observed by the end of PND 1 (Bartol et al., 2012). Onset of adenogenesis is typically marked by strong expression of ESR1 in nascent GE, whereas LE is effectively ESR1-negative. Cell behaviors supportive of adenogenesis, including patterns of ESR1 expression and cell proliferation (Masters et al., 2007; Tarleton et al., 1998), differ markedly between these two epithelial cell types.

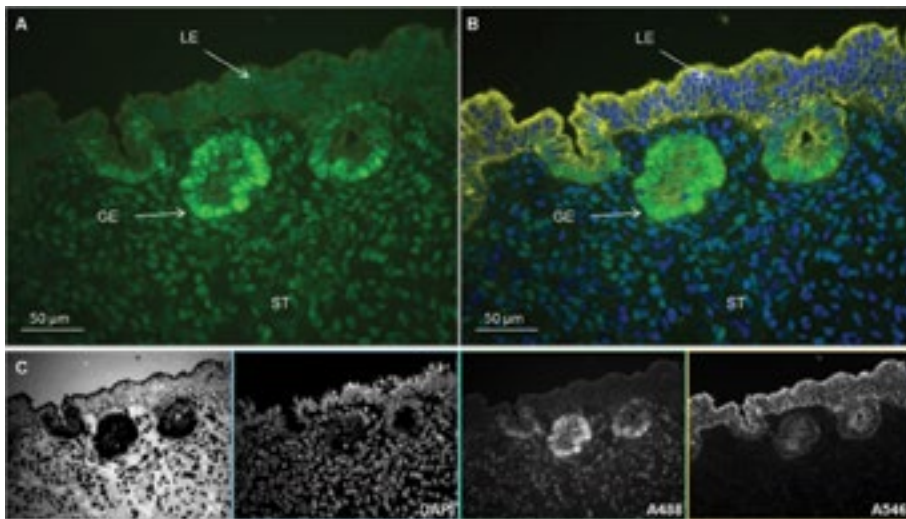


Figure 1. MSI process. Uterine cross-sections were stained with DAPI to identify cell nuclei and subjected to immunohistochemical procedures for IF localization of ESR1 and CK8. Images were captured using a Nuance FX MSI system. Raw images (A) were spectrally unmixed to produce images composed of wavelength-specific data and related composite images (B). Wavelength specific data (C) are illustrated for autofluorescence (AF), cell nuclei (DAPI), ESR1 (A488) and CK8 (A546).

Procedures for evaluation of cellular and molecular events characteristic of GE, LE and ST *in situ* are needed in order to understand the process of endometrial morphogenesis and cytodifferentiation of endometrial cells.

Uterine gland development can be better understood by evaluating the expression of molecules recognized to play a role in mediation of adenogenesis, such as ESR1 (Bazer, 2012). Using immunofluorescence (IF), multispectral imaging (MSI), and digital image processing (DIP), expression patterns for such morphoregulatory gene products can be evaluated in endometrial tissues precisely, efficiently and on a tissue compartment-specific basis. Immunofluorescent images captured using MSI technology, coupled with indirect, non-amplified IF procedures, can provide both qualitative and quantitative data. The latter, obtained from captured images, can be extracted using DIP. Collectively, these technologies provide the tools with which to establish a protocol for assessment of endometrial cell compartment-specific gene expression associated with neonatal uterine adenogenesis, as necessary to understand this process more completely. Here, objectives were to use IF, MSI and DIP in developing a protocol designed to automate: (1) procedures for delineation of endometrial cell compartments (GE, LE and ST) using cytokeratin-8 (CK8) expression as a mask for epithelium and ESR1 expression within this mask to identify GE, and (2) assessment of ESR1 expression in neonatal porcine endometrial GE, LE and ST.

MATERIALS AND METHODS

Tissue Processing and Immunofluorescent Staining

In order to eliminate animal variability in this protocol development and validation study, uterine tissue was collected from a single neonatal gilt at PND 5. Tissues were immediately embedded in Optimum Cutting Temperature (OCT) compound, frozen in liquid nitrogen and stored at -80°C . Embedded tissues were cryosectioned at $7\mu\text{m}$, dried for 5 min using warm air, and fixed in cold 4% paraformaldehyde (PAF) for 10 min. Slides were rinsed with water and washed twice in phosphate-buffered saline (PBS, pH 7.4). A blocking solution of 10% non-immune goat serum in PBS was applied to all sections, which were incubated for 20 min in a humidified chamber. Primary antibodies were applied simultaneously as a cocktail including anti-ESR1 (mouse monoclonal IgG1, sc-56833, Santa Cruz Biotechnology, 1:50) and anti-CK8 (ab94894, Abcam, 1:250). Next, slides were incubated at room temperature for one hour and washed twice in PBS. Matched fluorescently-labeled secondary antibodies of the Alexafluor series, including Alexafluor 488 (A488 goat anti-mouse IgG1, A-21121, Invitrogen, 1:400) for ESR1 and Alexafluor 546 (A546 goat anti-rabbit IgG, A-11010, Invitrogen, 1:400) for CK8, were then applied simultaneously. Tissues were incubated in a humidified chamber for one hour and then washed twice in PBS. Coverslips were mounted using mounting

medium with DAPI (Vector Laboratories; Burlingame, CA) to stain cell nuclei. All sections from which data were collected were processed together in a single batch. Tissues were stored overnight at 4°C before imaging.

Multispectral Imaging (MSI)

Fluorescently labeled neonatal porcine endometrial cross-sections were imaged in one session using a Nuance FX MSI system (Caliper Life Sciences, Hopkinton, MA) affixed to a Molecular Machines and Industries (MMI) CellCut Workstation using a Nikon TE-2000U inverted microscope (MMI, Haslett, MI). This system captured emission wavelength-specific images of fluorescent signals *in situ* using long-pass emission filter cubes optimized for DAPI, A488, and A546 (Chroma Technology Corp., Bellows Falls, VT). To distinguish each target signal, image data were spectrally unmixed to produce component images based on a spectral library of emission wavelengths using Nuance FX software. Development of the spectral library involved collection of wavelength-specific data from tissue sections treated with either anti-ESR1 or anti-CK8 primary antibodies and matched secondary antibodies (A488 or A546), or that were stained with DAPI alone. Negative controls included the omission of primary antibodies, resulting in a total lack of corresponding immunoreactivity. Procedures permitted removal of autofluorescence and collection of wavelength-specific data from all captured images.

Digital Image Processing (DIP) and identification of endometrial cell compartments

Exported, wavelength-specific data were analyzed using CellProfilerTM and CellProfilerTM Analyst (CPA; www.cellprofiler.com). Using this DIP software, a series of steps was defined in order to establish a protocol for automated identification of GE, LE and ST. Each wavelength-specific channel corresponded to a specific targeted signal. Cytokeratin-8, an epithelial-specific structural marker, was used as a mask to highlight epithelium (intensity threshold range 0.00-1.0 relative intensity units; RIU). Images were captured such that only epithelial and stromal compartments appeared in the field of view. Therefore, all cells not masked by CK8-specific signal were defined as ST by default and masked accordingly, revealing cells of the epithelium (GE + LE). The ESR1 channel was set at a high intensity threshold range (0.02-1.0 RIU) and used alone as the mask for GE, or in combination with CK8-specific signal to identify LE. All objects in a field were identified using a nuclear counterstain (DAPI) based upon measurement ranges of object size (20-150 pixels in diameter) and relative intensity (0.0-1.0 RIU). Merged objects were distinguished using relative intensity calculations.

With the DIP protocol established, data collected for each cell compartment (GE, LE and ST) included: (1) mean signal intensity indicative of ESR1, expressed in RIU (RIU x 103); and (2) ESR1 labeling index (LI), defined as the percentage of

cells in a given compartment determined to express ESR1 at or above a signal (A488) threshold. The signal threshold used in LI calculations was determined empirically for epithelium and stroma by means of machine-learning algorithms developed using CPA (Ljosa and Carpenter, 2009). Factors considered included measures of A488 intensity and objectively excluded other factors such as object shape, size, and texture. A total of 11 images of both mesometrial and anti-mesometrial endometrium were captured from five non-sequential sections. Procedures enabled identification and scoring of 2,132 epithelial cells and 3,498 stromal cells as being either ESR1-positive (ESR1+) or ESR1-negative (ESR1-).

Statistical Analyses

Quantitative data were visualized and subjected to analyses of variance using JMP/SAS software (SAS Institute, Inc. Cary, NY; version 9.2). Statistical models considered variation due to cell (GE, LE and ST), tissue section, area within each section, and appropriate interactions. To determine if ESR1 expression and/or ESR1 LI were endometrial cell compartment-specific, pre-planned orthogonal comparisons were performed to compare responses of epithelium (GE + LE) to stroma and GE to LE. Data are presented as least squares means with standard errors.

RESULTS

Steps in the MSI process for evaluation of neonatal porcine endometrial histology and immunolocalization

of CK8- and ESR1-positive cells are illustrated in Figure 1. Raw images (Figure 1a) were spectrally unmixed to reveal composite images (Figure 1b), showing uniquely CK8-positive epithelial cells (GE and LE) supported by underlying, CK8-negative stroma. Procedures enabled extraction of autofluorescence, as well as wavelength-specific data indicative of cell nuclei (DAPI), ESR1 (A488) and CK8 (A546; Figure 1c). As expected, signal indicative of ESR1 was observed primarily in nascent GE and stroma.

The DIP protocol enabled automated identification of total endometrial nuclei (Figure 2a). Masking procedures applied to discriminate between epithelium and stroma, as well as epithelial cell types, further enabled automated identification of total epithelial nuclei (Figure 2b), stromal nuclei (Figure 2c), and both glandular (Figure 2d) and luminal (Figure 2e) epithelial nuclei. Preliminary data indicating that results effectively identical to those reported here can be obtained when tissue compartments are identified manually, suggest that this automated protocol is histologically accurate. Raw data, collected from the complete set of digital images for ESR1, illustrating information collected from 5,630 cells, are presented in Figure 3. Results indicated variation in ESR1-specific signal within and between cell compartments.

Representative, spectrally unmixed images depicting neonatal porcine endometrium immunostained for CK8 and ESR1, together with mean ESR1 expression and ESR1 LI data, are presented in Figure 4. Overall, ESR1 expression was greater ($P < 0.01$) in epithelium than stroma and, for the epithelial compartment, greater ($P < 0.01$) in GE than in LE (Figure 4c). An estimate of the percentage of cells in each compartment expressing ESR1 above a fixed threshold, ESR1 LI did not differ, on average, between epithelial and stromal compartments. However, for the epithelial compartment, ESR1 LI was greater ($P < 0.01$) in GE than in LE (Figure 4d).

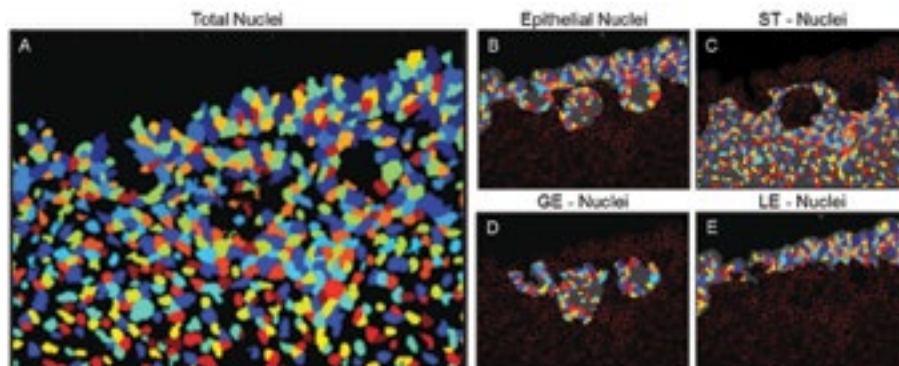


Figure 2. Identification of endometrial cell compartments using CellProfilerTM for DIP. Endometrial cell nuclei were identified based on DAPI signal (A). Colors denote individual objects identified as nuclei. Epithelial nuclei (B) were identified using a virtual mask based on CK8 signal. Stromal nuclei (C) were identified using the inverse mask for CK8 signal. Two epithelial categories were delineated. Glandular epithelium (GE) was masked based upon ESR1 signal alone (D). Luminal epithelium (LE) was identified by subtracting the GE mask from the CK8 total epithelial mask.

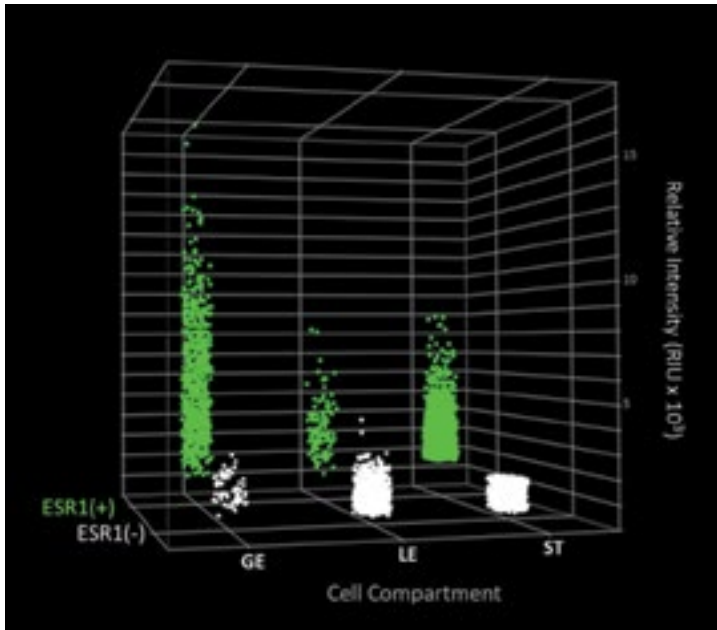


Figure 3. Raw data for ESR1+ (green) and ESR1- (white) cells in epithelial (GE and LE) and stromal (ST) compartments. Data are presented for 5,630 observations in relative intensity units (RIU $\times 10^3$).

DISCUSSION

Results reported here established that IF, MSI and DIP procedures could be applied to develop a protocol for accurate, efficient identification of cell compartments and sub-compartments in neonatal porcine endometrium. Specifically, procedures described here enabled clear delineation between stromal and epithelial compartments and, further, delineation between GE and LE as sub-compartments of the epithelium. This, in turn, enabled automated extraction of qualitative and quantitative data on a cell compartment-specific basis.

Automated image analysis provides several advantages over traditional protocols involving human observations (Ljosa and Carpenter, 2009). For example, DIP and downstream automated analyses provide objectivity, consistency and the precision that comes with the ability to interrogate effectively all objects (cells) within a field of view across multiple samples from many animals. Procedures of this kind, developed here, allow investigators to identify and distinguish subtle differences in cytological and molecular conditions between cells and/or cell compartments not detectable by the human eye. The combination of technologies employed here permitted collection of large, wavelength-specific, quantitative datasets for

cell compartment-specific characteristics necessary to provide precise assessment of developmentally important endometrial cell behaviors.

Results of automated image analyses designed to identify patterns of ESR1 expression in the neonatal porcine endometrium presented here agree with earlier reports (Tarleton et al., 1999; Tarleton et al., 1998). It was expected that ESR1 expression would be pronounced in GE as compared to LE and that, overall, epithelial ESR1 expression would be similar to that of stroma. The fact that results agree with published observations provides indirect validation of the image analysis protocol described here.

The image analysis protocol described here used DAPI staining to identify individual objects defined as cell nuclei. With the entire population of endometrial cells identified in this way, CK8- and ESR1-specific signals were used to delineate areas or 'masks' that could be employed to define endometrial cell compartments. Algorithmic inversion of the CK8 mask enabled definition of the stromal cell compartment. A mask was developed using a high intensity threshold applied to ESR1 expression to highlight GE. This ESR1 mask was then subtracted from the CK8 mask to reveal LE. With procedures for automated cell compartment identification established,

ESR1 expression data were extracted from all DAPI-positive objects in all images. Because cell compartments were identified by area based on masks and not on an individual cell basis, the protocol for extraction of ESR1 expression data allowed for cells in each compartment to register as ESR1+ or ESR1- depending upon signal intensity and threshold as defined by rules established using CPA (www.cellprofiler.com). When LE was distinguished from GE visually, by manually tracing LE, subtraction of the traced portion from the CK8 mask identified GE correctly (data not shown). Results from this manual trace method provide validation of the automated protocol described here.

The requirement for communication between stromal and epithelial compartments in development of female reproductive tract tissues is well established (Bartol et al., 2006; Kurita et al., 2001). Procedures described here permit automated assessment of specific cell behaviors *in situ*. This is important because cells removed from context in primary culture rarely behave as they would be expected to *in vivo* (Glasser and Mulholland, 1993). With a novel protocol for automated, DIP-based evaluation of cell compartment-specific events associated with endometrial development now in hand, the stage is set to pursue investigations of cell-cell interactions essential for support of uterine adenogenesis.

ABBREVIATIONS

Definitions for abbreviations not defined in the text are listed below.

DAPI: 4',6-diamidino-2-phenylindole

SAS: Statistical Analysis System

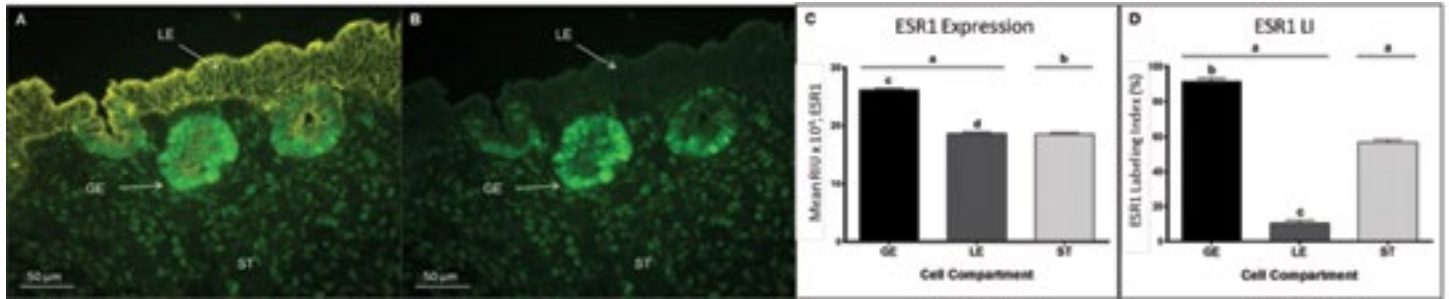


Figure 4. A spectrally unmixed composite image (A) depicting neonatal porcine endometrium immunostained for both CK8 (yellow) and ESR1 (green). Cell compartments (GE, LE and ST) are identified. Extraction of wavelength (A488)–specific data from image (A) produced image (B), illustrating ESR1 expression patterns *in situ*. Histograms illustrate data for mean ESR1 expression (C) and ESR1 LI (D) for GE, LE and ST. For quantitative data (C, D), comparisons included epithelium (GE + LE) vs. ST and GE vs LE. Different letters denote differences ($P < 0.001$).

REFERENCES

- Bartol, F. F., A. A. Wiley, D. J. Miller, A. J. Silva, K. E. Roberts, M. L. P. Davolt, J. C. Chen, A. L. Frankshun, M. E. Camp, K. M. Rahman, J. L. Vallet, and C. A. Bagnell. (2012). Lactocrine signaling and developmental programming. *Journal of Animal Science* (invited review) In Press.
- Bartol, F. F., A. A. Wiley, and C. A. Bagnell. (2006). Uterine development and endometrial programming. *in* C. J. Asworth and R. R. Kraeling (Eds.) *Control of Pig Reproduction VII*. 113-130. Nottingham University Press, UK.
- Bartol, F. F., A. A. Wiley, J. G. Floyd, T. L. Ott, F. W. Bazer, C. A. Gray, and T. E. Spencer. (1999). Uterine differentiation as a foundation for subsequent fertility. *Journal of Reproduction and Fertility*. Supplement 54: 287-302.
- Bartol, F. F., A. A. Wiley, T. E. Spencer, J. L. Vallet, and R. K. Christenson. (1993). Early Uterine Development in Pigs. *Journal of Reproduction and Fertility*. Supplement 48: 99-116.
- Bazer, F. W. (2012). Fertility: role of repressor of estrogen receptor activity. *Endocrinology* 153: 3555-3557.
- Cooke, P. S., G. C. Ekman, J. Kaur, J. Davila, I. C. Bagchi, S. G. Clark, P. J. Dziuk, K. Hayashi, and F. F. Bartol. (2012). Brief exposure to progesterone during a critical neonatal window prevents uterine gland formation in mice. *Biology of Reproduction* 86: 63, 61-10.
- Glasser, S. R. and J. Mulholland. (1993). Receptivity is a polarity dependent special function of hormonally regulated uterine epithelial cells. *Microscopy Research & Technique* 25: 106-120.
- Gray, C. A., F. F. Bartol, B. J. Tarleton, A. A. Wiley, G. A. Johnson, F. W. Bazer, and T. E. Spencer. (2001). Developmental biology of uterine glands. *Biology of Reproduction* 65: 1311-1323.
- Kurita, T., P. S. Cooke, and G. R. Cunha. (2001). Epithelial-stromal tissue interaction in paramesonephric (Müllerian) epithelial differentiation. *Developmental Biology* 240: 194-211.
- Ljosa, V. and A. E. Carpenter. (2009). Introduction to the quantitative analysis of two-dimensional fluorescence microscopy images for cell-based screening. *PLoS Computational Biology* 5: e1000603.
- Masters, R. A., B. D. Crean, W. Yan, A. G. Moss, P. L. Ryan, A. A. Wiley, C. A. Bagnell, and F. F. Bartol. (2007). Neonatal porcine endometrial development and epithelial proliferation affected by age and exposure to estrogen and relaxin. *Domestic Animal Endocrinology* 33: 335-346.
- Park, S., S. Yoon, Y. Zhao, S. E. Park, L. Liao, J. Xu, J. P. Lydon, F. J. DeMayo, B. W. O'Malley, M. K. Bagchi, and B. S. Katzenellenbogen. (2012). Uterine development and fertility are dependent on gene dosage of the nuclear receptor coregulator REA. *Endocrinology* 153: 3982-3994.
- Tarleton, B. J., A. A. Wiley, and F. F. Bartol. (1999). Endometrial development and adenogenesis in the neonatal pig: effects of estradiol valerate and the antiestrogen ICI 182,780. *Biology of Reproduction* 61: 253-263.
- Tarleton, B. J., A. A. Wiley, T. E. Spencer, A. G. Moss, and F. F. Bartol. (1998). Ovary-independent estrogen receptor expression in neonatal porcine endometrium. *Biology of Reproduction* 58: 1009-1019.

ACKNOWLEDGMENTS

Authors acknowledge the Auburn University Cellular and Molecular Biosciences (AU-CMB) program and the AU-CMB-supported Undergraduate Summer Research Scholars program for resources enabling this opportunity for KER. This work was supported by NSF-EPS-1158862. Work involving vertebrate animals was approved by the Auburn University Institutional Animal Care and Use Committee.

PARAMETER ESTIMATION AND SIMULATION USING VIRTUAL ELEVATION METHODS FOR RACE CYCLING

WILLIAM D. MCGINNIS

ABSTRACT

In professional cycling, the performance of athletes is largely determined by the effective drag force relative to power input over the course of a race. Testing athletes in a wind tunnel is effective but time consuming and expensive. By outfitting a bicycle with a Global Positioning System (GPS) and a power meter, a work-energy model can be derived and used to generate an apparent elevation profile. Using a Monte Carlo optimization, the unknown coefficients in the energy equation were found for a variety of riders by comparing the virtual elevation profile to the true elevation profile measured by the GPS. This operation was performed over the course of regular training rides and races, with no deviation from the athletes' regular routines. With this information and historical training data, the athletes' best possible performances over certain terrains were found, and ideal power profiles could be generated for those terrains. Their actual performances were compared to the simulated results to demonstrate the validity of the model. These processes have been used to analyze performance after races, to predict performance before races, and to select equipment or pacing strategies more judiciously.

INTRODUCTION

In professional cycling, winners of races that span multiple weeks are often decided by a handful of seconds. The 1989 Tour de France was famously won by a mere eight seconds after nearly 90 hours of total racing. Armed with the prevalence of reliable and plentiful data from racing and training, this paper presents a methodology to accurately estimate the effective drag coefficient (C_d) and coefficient of rolling resistance (C_{rr}) of a rider over any given terrain. The estimates are done using virtual elevation methods, which have been shown by Chung (2012) to be reliable for this application. Virtual elevation consists of using a known model with random parameter values to simulate a ride so that the model can be optimized to set the calculated and measured

elevation profiles equal to one another. By coupling the power data with GPS data, the method can be applied to arbitrary routes rather than simply to short loops, as Chung (2012) recommended.

BACKGROUND

By developing a robust model of a bicycle's expenditure and storage of a known energy input and assuming energy is conserved, one can infer the path the bicycle has taken in space. A bicycle's energy equation (Chung, 2012) is composed of four components that store or expend energy added to the system by the rider: rolling resistance, aerodynamic drag, kinetic energy, and potential energy,

$$J_{plant} = J_{rr} + J_{aero} + J_{ke} + J_{pe}. \quad (1)$$

To derive a more practical and useful formula, each term may be differentiated with respect to time in order to generate a power equation.

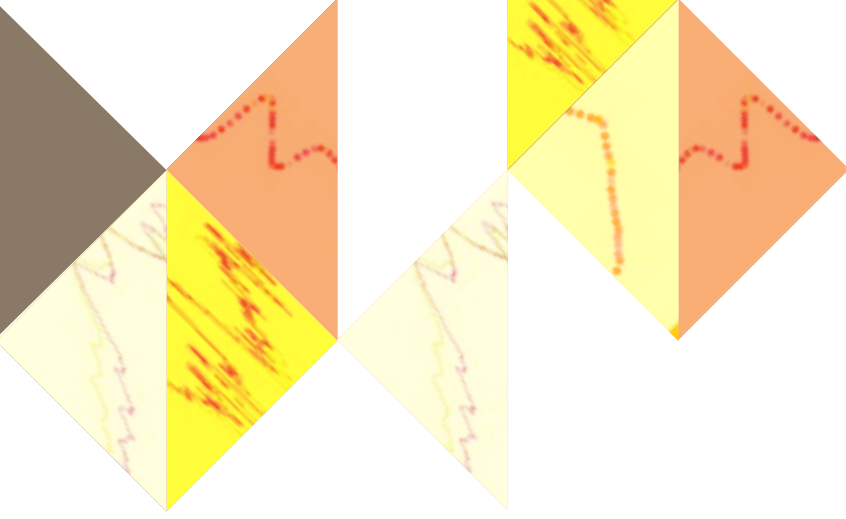
$$P_{plant} = P_{rr} + P_{aero} + P_{ke} + P_{pe}. \quad (2)$$

The accepted model (Martin and Martin, 2006) for energy lost by a tire is

$$P_{rr} = F_{rr} v \quad (3)$$

where the time rate of energy lost is given by the force of rolling resistance, F_{rr} , multiplied by velocity, v . In most cases, however, it has been shown that the force of rolling resistance increases linearly with the load on the wheel, due to increased deformation and shear of the tire. Because of this increased in force of rolling resistance, we can define a constant, C_{rr} , as

$$C_{rr} = F_{rr}/F_n \quad (4)$$



where F_n is the vertical load on the tire. In order to simplify the equation, it is assumed that both tires behave similarly and can be combined into one effective term (Gent and Walter, 2006), giving the total energy loss for the system due to rolling resistance, P_{rr} , as

$$P_{rr} = C_{rr} m g v_{gnd} \quad (5)$$

where m is mass, g is gravitational force, and v_{gnd} is the velocity of the bicycle. Because C_{rr} is an inferred value, it can easily account for not only the friction at the contact patch of the tire but also for bearing friction in the wheels, which is often “downstream” of the power measurement. In reality, C_{rr} varies with the road surface. On a rougher road, C_{rr} is higher than on a smoother road (Gent and Walter, 2006). For the scope of this model, it is assumed that the road surface remains constant throughout the data collection. Further instrumentation could allow for the estimation of road surface roughness and improve the model in future work.

The power dissipated by the aerodynamic drag, P_{aero} , of a cyclist is given by Batchelor (2002), where ρ is the current air density, C_d is the drag coefficient, A is frontal area, and v_{air} is the air speed.

$$P_{aero} = \frac{1}{2} C_d A_f \rho v_{air}^2 v_{gnd} \quad (6)$$

Again, $C_d A$ is not in reality a constant and varies with both the Reynolds number of the air and, more importantly, the geometry of the rider and bicycle.

While a rider is not completely static on a bicycle, a mean effective value of $C_d A$ is still not only very useful but even more representative of race conditions than a more exact measure of a very constrained case, as can be found from wind tunnel testing.

The power, P_{ke} , dissipated due to a change in kinetic energy of a mass is given by Jain (2009), where acceleration of the center of mass of the rider, ma_{cg} , is assumed to be equal to the time rate of change of GPS velocity, v_{gps} ,

$$P_{ke} = ma_{cg} v_{gps} \quad (7)$$

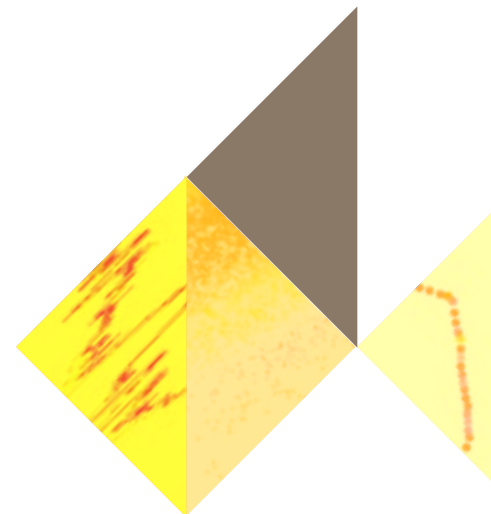
The power, P_{pe} , stored as potential energy in a mass is given by Jain (2009), where θ_{rg} is the angle of the road gradient.

$$P_{pe} = m g v_{gnd} \sin(\theta_{rg}) \quad (8)$$

Making a small angle approximation due to the relatively small angles present in road gradient, Equation 8 becomes

$$P_{pe} = m g v_{gnd} s \quad (9)$$

where s is the road slope, meters of elevation change divided by meters of horizontal distance traveled.



The power equation can be expanded using each of the now defined power component equations. This expanded power equation creates a first order non-linear differential equation that relates input power to velocity over time, with two unknowns for any instrumented bicycle system, C_{rr} and C_dA ,

$$P = C_{rr}mgv_{gnd} + smgv_{gnd} + ma_{car}v_{gnd} + \frac{1}{2}C_dA_f\rho v_{air}^2v_{gnd}. \quad (10)$$

Solving for slope, this becomes

$$s = \frac{P}{mgv_{gnd}} - C_{rr} - \frac{a_{car}}{g} - \frac{\frac{1}{2}C_dA_f\rho v_{air}^2}{mg}. \quad (11)$$

The air velocity is calculated using the rider's GPS heading and velocity combined with a vector of ambient wind speed and direction as measured on the testing day. The assumption made is that the ambient wind is at the same speed and in the same direction for the entire test. Equation 11 is used to iteratively solve for the elevation change of the system, given its mass, air density, velocity, acceleration and initial guesses for C_dA and C_{rr} . Then a subset of data is analyzed in order to solve for C_dA and C_{rr} by comparing the resultant virtual elevation profiles with the measured true elevation profile.

INSTRUMENTATION

In order to implement the virtual elevation method on-line, a number of parameters (power, elevation, velocity) must be monitored through the bicycle's instrumentation system. The most important metric to measure on the system is the power applied by the rider (the plant). Strain gages can be placed in various places in the drive train and used to solve for torsion in the shaft. Then power is given by the equation

$$P_{plant} = \tau\dot{\theta} \quad (12)$$

where τ is torque at the rear wheel hub. This process has been very well developed by the cycling companies, Saris™ and SRM™. Elevation is also crucial to the validity of the estimates, as a true elevation profile is the standard by which the model is trained. Although a variety of sensors can sufficiently measure altitude, GPS devices provide an accessible choice for determining elevation. Similarly, velocity can be measured with other devices such as a wheel encoder and known roll out of a non-drive wheel, but with the need for a GPS for other sensors, it makes sense to use the GPS for velocity measurement as well. Another advantage is the built-in function-

ality of Garmin™ GPS units to interface with Saris PowerTap™ and SRM™ power-meters, yielding a file (.TCX format) with all of the required data included in one place.

MODEL OPTIMIZATION

In order to solve for the parameters, the slope equation is seeded with 10,000 pairs of pseudo-random C_dA and C_{rr} values, and integrated in a forward calculation to generate a virtual elevation profile. For each pair of guesses, a characteristic error value, the mean-squared error between virtual and true elevation, is stored. When the errors of the 10,000 pairs have been evaluated, a fourth order, two-dimensional polynomial is fit to give error as a function of C_dA and C_{rr} . This polynomial forms what is referred to as the cost function. From here, the cost function can simply be minimized to find the final estimate for C_dA and C_{rr} .

In this study, this computational process was integrated into a Python-based desktop application, called BikeVE. With this tool, users upload a Garmin™ GPS file, input the known parameters, select any two parameters to estimate (not just C_dA and C_{rr}), and can perform the model optimization to solve the problem. An interesting note is that users most commonly choose to solve for wind speed and C_dA , not C_{rr} and C_dA . Below, two examples are presented to illustrate the computational process.

EXAMPLE 1: DAVID MILLAR

Using David Millar's ride at the 2010 Tour de France stage 19 time trial in Bordeaux, France (Millar, 2012), the computational method derived above can be used. The virtual elevation and true elevations that result from the optimization can be seen in Figure 2. The output from the optimization was a C_{rr} value

of .0075 and a C_dA value of .2100. These resultant values are, for the most part, in line with expected values (Coggan, unpublished data). The C_{rr} value was slightly higher than expected, which was likely a result of including all friction losses in the term C_{rr} . Also, lack of velocity variation in the collected GPS file, implies that C_{rr} is not significantly affected by the C_dA term. This relationship is reflected by the slope of the darker band in Figure 1. With a drive train efficiency term included, the C_dA would be expected to drop. This estimation of C_dA and the average power from the performance in the time trial, which was slightly longer than an hour, yields an estimated ratio of Functional Threshold Power (a physiological metric used to quantify fitness) to C_dA of 1859.7. Considering the timing of the race, 19 days into a grand tour, the ratio falls in the expected range of 1750 to 2000 as Coggan (unpublished data) determined can be expected of a tired professional.

Because the data were not derived from a controlled test but rather an actual race file, braking is prevalent but is seen by the model to be a sudden large hill. Such misinterpretations account for the errors in more technical parts of the course. By noting the locations where the derivative of the error between the virtual and true elevations is highest in relation to the GPS coordinates, a map of error prone spots can be generated in order to shed more light on the sources of error in the model. As one would expect, the deriv-

ative of error is highest going into corners, where the rider was using the brakes (Figure 3). Furthermore, if the sum of the error is considered to be lost potential energy in the system, there is an energy loss of 88 KJ in just 1:06 of riding or just over 6% of the total energy expended in the race. It is worth noting that in this case of a time trial bike, the action of braking is not only the use of rim brakes but also most likely moving the hands to the outer bars to form an air brake with the upper body.

EXAMPLE 2: ANDREW TALANSKY

A second case is Andrew Talansky's 10th stage time trial at the 2011 Vuelta a Espana (Talansky). In his case, the resultant elevation plots (Figure 4) match one another much more closely than those of Millar, a difference that can be attributed to the larger variation in velocity over the course of the ride. Because C_{rr} does not vary with velocity while C_dA does, the two parameters cannot be properly decoupled without variant velocity. Error can again be attributed to heavy breaking on the way in and out of Salamanca, where there were a number of roundabouts and sharp city street turns. Estimating 72 kg for his total weight (person, bike and clothing) and 1.037 for ρ , his C_{rr} and C_dA are estimated to be .0025 and .02303, respectively.

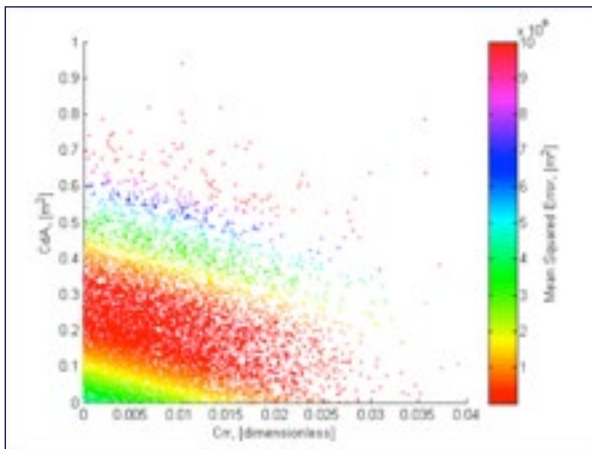


Figure 1. David Millar case study. Results of randomly generated pairs of drag coefficient (C_dA) and coefficient of rolling resistance (C_{rr}), colored for mean squared error. The distinct red band of lowest error guesses can be seen in the middle of the scatter.

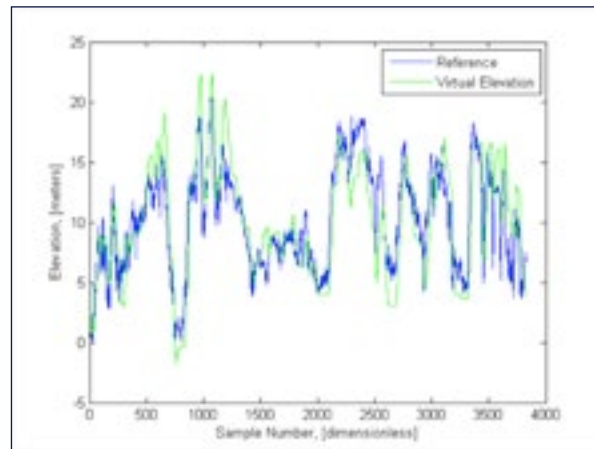


Figure 2. David Millar case study. Best virtual elevation profile as estimated by Monte Carlo optimization vs. real elevation as measured by GPS. Small errors can be seen throughout the profile due to variations in wind, braking, and other unaccounted for disturbances.

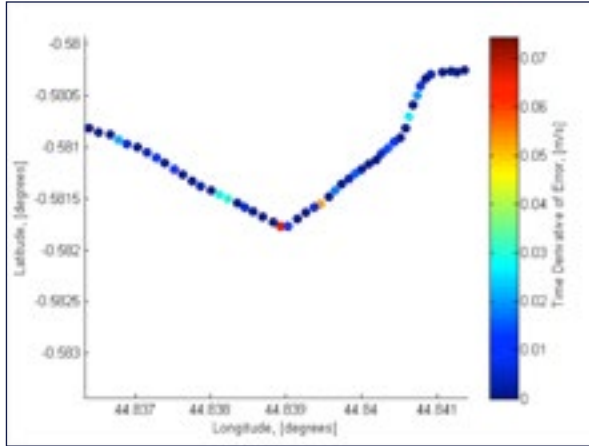


Figure 3. David Millar case study. Geographic positioning of cyclist at sharp corner, showing spikes in time derivative of error (denoted by color dots).

The band of fittest guesses in Figure 5 can be seen to slope steeply downward as C_{rr} rises. This slope is more in line with the expected result than was the case in Millar's data, in which the slope was more gradual. This result can again be attributed to the greater variation in velocity over the course of the ride. The derivative of error is highest at points leading into and coming out of turns, where it can be assumed that the rider was both braking heavily and using the outer handlebar, which greatly increases his frontal area. In Figure 6 where one of the sharper turns is detailed, the clear spike in error as the rider applied the brakes and sat up is shown.

MODELING THE RIDER

The dynamic model developed in this study is only capable of simulating performance over a terrain with known power input. While using steady power inputs to estimate a particular rider's performance may be suitable, it does not capture how races transpire in reality, nor is it the fastest way to ride most courses. A more ideal power output for the rider must be found in order to fully assess an athlete's potential on a given course. Given a large library of historical training and racing power data from a rider, it is possible to generate a curve of maximal power output for a given time duration. Luckily, with the prevalence of power meters in the elite cycling community, most high-level cyclists have years of data from every day of training and racing, often in excess of 3,000 hours. In order to find the optimal power input for the rider over a course, it is necessary to determine whether or not an arbitrary wattage file was possible from the rider. By recursively bisecting the power file, and

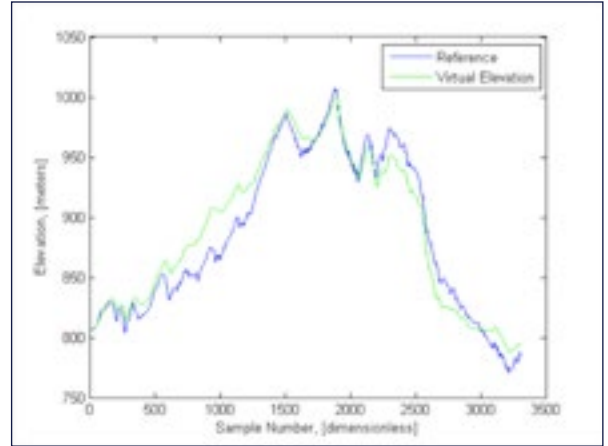


Figure 4. Andrew Talansky case study. Best virtual elevation profile as estimated by Monte Carlo optimization vs. real elevation as measured by GPS. Small errors can be seen throughout the profile due to variations in wind, braking, and other unaccounted for disturbances. This race occurs over greater topographic relief. Thus, errors are likely primarily due to braking on descents.

checking whether each incrementally smaller piece is sub-maximal on the rider's maximal power curve, it can be inferred whether or not the ride was possible by a certain rider.

OPTIMIZATION FOR TERRAIN

One major function of the model of the rider and of the system is to simulate an athlete's performance over a certain terrain. Given an elevation profile and a power file, it is possible to estimate the time required to complete a course. In order to simulate the ride, the forces on the rider can be summed:

$$ma_{cg} = \frac{P}{v_{gnd}} - C_{rr}mg - mgs - \frac{1}{2}C_dA_f\rho v_{gnd}^2 \quad (13)$$

$$a_{cg} = \frac{P}{v_{gnd}m} - C_{rr}g - gs - \frac{1}{2m}C_dA_f\rho v_{gnd}^2 \quad (14)$$

From these calculations, acceleration can be integrated to find velocity and position after some given time step. Because of the power term being divided by velocity, an initial velocity of zero using this model is impossible. To account for this impossibility, we assume an initial velocity of five m/s and an initial time of five seconds. Such an assumption results in an initial acceleration off the line which is well within the ability of any trained cyclist. In order to find the appropriate local slope for the next iteration, the position must be compared to the distance and elevation data-points from a GPS file of the desired course. The local slope is found by assuming a linear

gradient between the most recent and upcoming data points in the reference file.

Starting with a known sub-maximal baseline power file, a random search algorithm can converge on the fastest possible power profile for a course and its corresponding time. This algorithm involves changing the current best known power file randomly, checking it to ensure it was possible, simulating it, and then comparing the resultant time to the previous benchmark's time. If the new time is faster, then the

perturbed power file becomes the new benchmark, and the process is repeated. If the new time is slower, or if the perturbed power file was found to be impossible for the rider, the previous benchmark file is perturbed randomly again. As the power file approaches the boundary of the athlete's ability to perform, the number of points, which are randomly changed, is decreased to allow for finer tuning. This process will eventually converge on the best possible performance for the athlete over the terrain.

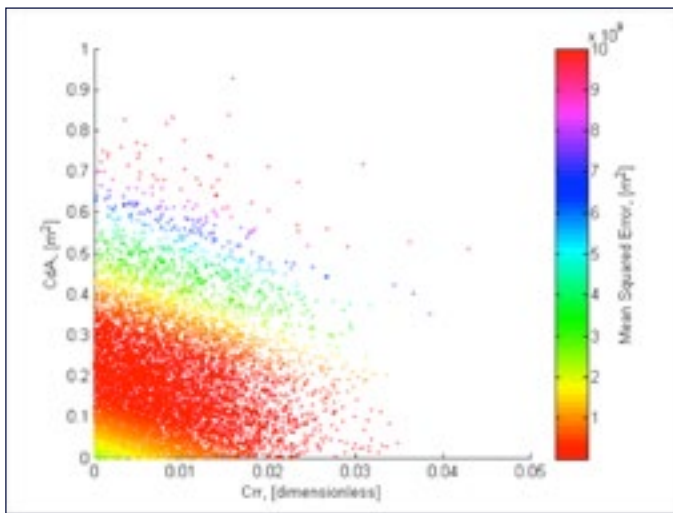


Figure 5. Andrew Talansky at the Vuelta a Espana. Results of randomly generated pairs of drag coefficient (C_{dA}) and coefficient of rolling resistance (C_r), colored for mean squared error. The distinct red band of lowest error guesses can be seen in the middle of the scatter. The band slopes at a notably steeper angle than that in Figure 1 due to greater velocity variation in the test run.

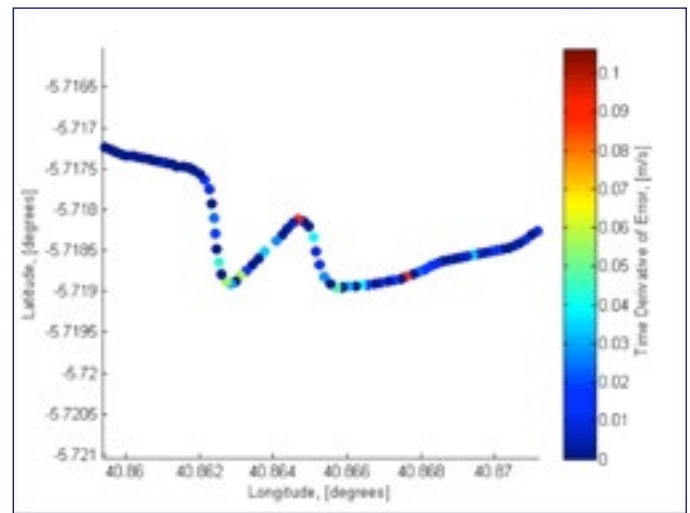
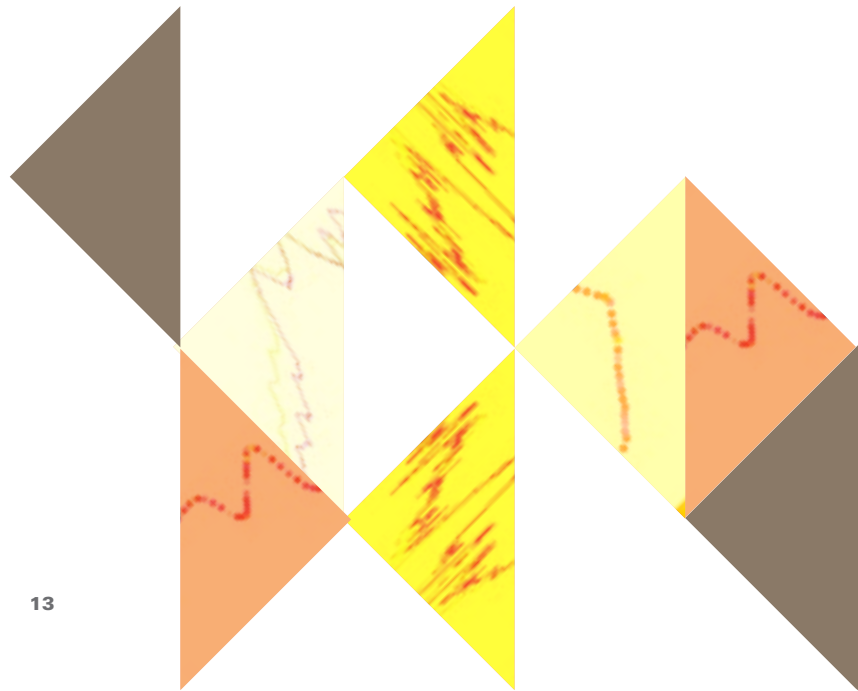


Figure 6. Andrew Talansky at the Vuelta a Espana. Geographic position of rider in sharp corner, showing spikes in derivative of error during presumed braking.



JOE MARTIN TIME TRIAL

The first stage time trial at the Joe Martin Stage Race in Fayetteville, AR, is notoriously difficult to pace. Starting out slightly downhill and climbing steadily, the short time trial is very fast despite its gradient. It remains ambiguous whether it is faster to ride a time trial or road bike, and whether to go easy on the flat to save for the climb or go hard on the flat and fade on the climb is yet to be seen. Further, the winner of the time trial is often the winner of the entire four-stage race, which on the national racing circuit holds prestige and prize money. Using virtual elevation methods to model a bicycle/rider system, and a maximal power curve to model the rider, it is possible to find the exact power profile which will result in the fastest time for a rider.

In this case the power curve is coupled with the dynamic model derived from the same rider's data prior to the event, to produce an estimate of his fastest possible ride. Using 0.29 as the C_dA for the rider on his road bike and upright, the suggested power profile is found to yield a time of 9:34. This time varies greatly from the actual one on race day of 10:14. When some context of the race schedule is given, it is clear that the Joe Martin Stage Race comes just days after the very taxing Tour of the Gila, which climbs the massive mountains of Southern New Mexico. It seems that the athlete may have been overly tired from this race, or botched pacing. Looking at results from races before and after Joe Martin, and at the results from the remainder of the race, it is apparent that this particular race was an anomaly. Regardless of the reason, it is indicated that the athlete did not ride to his best ability on race day. As a team director, this information may be used to inform roster selection for upcoming races, a coach may alter

training or rest schedules, and the racer may compare the idealized power files to his own to see whether it was a pacing error or one in preparation.

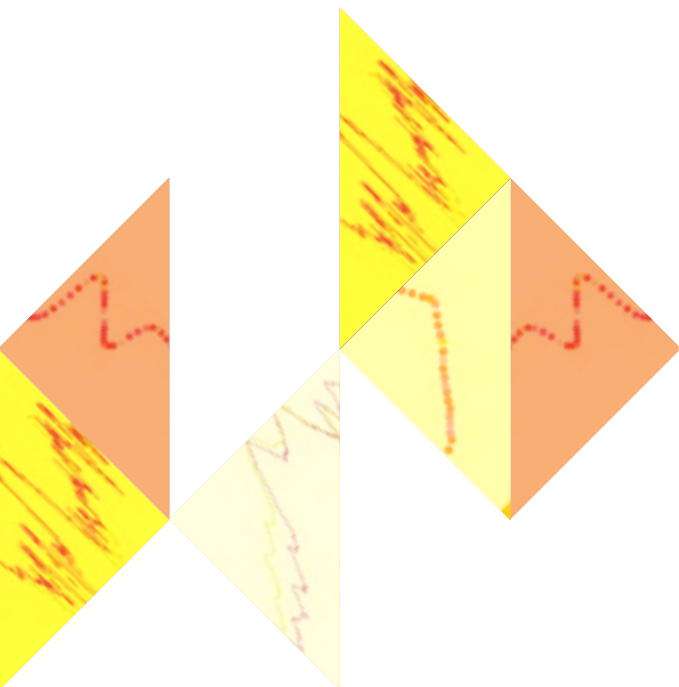
Upon further analysis, it can be seen that by dropping the C_dA to 0.24, the rate common for choked-up time trial bike position where the aerobars are held closer to the rider allowing for a more upright position that is more comfortable when climbing, and raising the mass one kg to account for the added weight of a time trial bike, the time would drop to just 9:29. This small margin creates uncertainty for the riders about bike selection since a mere five seconds separates two completely different bike options.

SOURCES OF ERROR

Using virtual elevation methods, there are two primary sources of error. Braking is not accounted for in the model at this point, so any braking over the course of a test will contribute greatly to error, manifesting itself as a sudden steep hill on the elevation profile. A means to correct this may be to reset the elevation to the true value after the derivative of error exceeds some quantity. Other sources of error include sensor errors, missing data points, imperfect true elevation profiles, local gradient estimation error in simulation, numerical integration error, and finding local maxima with the random search algorithm.

CONCLUSION

Using standard GPS files coupled with a power meter, it is possible to solve the slope equation for a cyclist's C_{rr} and C_dA with Monte Carlo methods. The rider itself can be modeled simply with a maximal power curve, which, when combined with the dynamic model, can be used to estimate the rider's best possible performance over an arbitrary terrain. This capability is used to detect the changes in C_dA due to various equipment changes and their impact on the performance of the rider over some benchmark course. The model can be used to estimate the athlete's performance at a particular event, to assess the worth of attending that event, and to tailor training to success in that event. Ideal pacing strategies with minimal braking can also be developed for any individual event. Finally, these methods can be used after an event to assess the energy lost due to braking and to compare that performance to the energy lost by other riders, which may shed light on deficiencies in handling skill or tire choice.



REFERENCES

- Batchelor, G. K. (2000). *An Introduction to Fluid Dynamics*. Cambridge, U. K.: Cambridge University Press.
- Coggan, A. *FTP Power to Drag Ratio Table*. http://4.bp.blogspot.com/-N54r1RmZ9ag/Th-51XzRmKI/AAAAAAAAA8M/_ht1jUHFx6A/s1600/FTP%2BPower%2Bto%2Bdrag%2Bratio%2Btable.jpg. (website accessed 26 Jan. 2013).
- Chung, R. *Estimating CdA With a Power Meter*. <http://anonymous.coward.free.fr/wattage/cda/indirect-cda.pdf>. (website accessed 23 Apr. 2012).
- Gent, A. N. and J. D. Walter. (Eds.) (2006). *The Pneumatic Tire*. Washington, D. C.: U. S. Department of Transportation.
- Jain, M. C. (2009). *Textbook of Engineering Physics, Part 1*. New Delhi, India: PHI Learning Private Limited.
- Martin, B., J. C. Martin, A. S. Gardner, and D. T. Martin. (2006). Modeling sprint cycling using field-derived parameters and forward integration, *Medicine & Science in Sports & Exercise*: 38, 592-597.
- Millar, D. *David Millar-Tour de France St 19*. <http://connect.garmin.com/activity/42191551>. (website accessed 18 Jan. 2012).
- National Research Council. (2006) *Tires and Passenger Vehicle Fuel Economy: Informing Consumers, Improving Performance*. Washington, D. C.: National Research Council of the National Academies.
- Talansky, A. *Ander Talansky-Vuelta a Espana, Stage 10*. <http://connect.garmin.com/activity/115668380>. (website accessed 18 Jan. 2012).

ACKNOWLEDGMENTS

The author would like to thank Dr. Roy J. Hartfield for acting as a faculty sponsor of this research.

THE TRIAL OF EUPHAME MACCALZEAN: FEMALE INHERITANCE AND THE PATRIARCHAL SOCIETY IN THE SCOTTISH WITCH-CRAZE OF 1590-1591

Yvette M. Jones, Adam J. Jortner

Abstract

Through a detailed examination of sixteenth century trial records, confessions, and execution accounts, this article focuses on the question: Could anxieties over female inheritance and female social dominance lead to witchcraft accusations? It examines specifically the trial of a wealthy woman named Euphame MacCalzean, who in 1591, amidst what is known today as the North Berwick panics, was accused, tried, and executed as a witch. After a thorough inspection of her case, this article argues that MacCalzean's story is a key example of the tensions between independent, powerful women and a traditional, early modern patriarchal society. I argue, in her instance, such tensions and resentments resulted in accusations of witchcraft, and subsequently, her death. In the hands of Euphame MacCalzean's male dominated community, witchcraft became an efficient means of controlling and limiting female power.

Euphame MacCalzean, as culpable and guilty thereof, to be taken to the castle hill of Edinburgh and there bound to the stake and burned in ashes, quick to the death and all and sundry her lands, heritages, tacks, steadings, rooms, possessions, corns, cattle, goods and gear to be forfeited and escheat to our sovereign lord's use (Normand and Roberts, 2000, 274).

The witch panics that began in the small town of North Berwick and spread throughout Scotland in the 1590s have been, for the most part, well researched and thoroughly documented (Adam, 1978; Seth, 1969). Witchcraft historians typically point to the heavy involvement of King James VI and his administration to justify their attention to

this period; however, many of the individual stories get lost amid the more popular accounts of James' association with these panics. Though Euphame MacCalzean was initially implicated in the royal scandal, only three of the 28 charges leveled against her relate to the monarchy. The remaining 25 charges of witchcraft reveal an issue infinitely more fascinating.

The accusations of witchcraft brought against MacCalzean ignited a storm of controversy in eastern Scotland in the late sixteenth century. Though at first it may seem that MacCalzean was just one of many women accused and executed in the Scottish witch craze of 1590-1591, a deeper look reveals that the accusations brought against her had intriguing economic undertones and possible hidden motives. First-hand accounts of the trial point more to an intense dispute over property and fear of MacCalzean's social and political power than to an actual belief that she participated in witchcraft. Her case can be taken as an example of the tensions that could occur between independent, authoritative women and the conventional patriarchal society. In her instance, and possibly in others, accusations of witchcraft could be used as a way to effectively dispose of a strong female threat.

MacCalzean's name, in connection with the witchcraft panic, was first brought to the public light by a servant named Geillis Duncan. Suspected of witchcraft herself, Duncan was tortured by her employer, David Seton, a municipal officer in the local town of Tranent, and forced to name her accomplices. One of the alleged

collaborators she named was Euphame MacCalzean. According to the popular pamphlet, *Newes from Scotland*, which kept the public up to date on Scottish witchcraft trials and executions, Geillis Duncan “caused one Euphame MacCalzean to be apprehended for conspiring and performing the death of her godfather, and for using her art upon a gentleman being one of the lords and justices of the session to bear good will to her daughter” (Normand and Roberts, 2000, 313). What was not noted in the pamphlet was the fact that David Seton was MacCalzean’s brother-in-law, married to Katherine Moscrop, sister of Euphame’s husband Patrick (Yeoman, 2002). Disagreements between the two sides over who received more money after the death of Patrick and Katherine’s mother led to animosity between the Setons and the MacCalzeans (Normand and Roberts, 2000). Did David Seton use his servant and the community’s fear of witchcraft as an opportunity to dispose of MacCalzean? Much of the evidence suggests that he did, and it is true that after the first accusation against her was made, the rest of her extended family did not hesitate to add to the charges.

MacCalzean’s case, of course, needs to be understood within the context of the culture of the time period, including the context of gender roles and relationships. Scholars agree that the early modern European world was composed of a strict social hierarchy and a love of order that dominated the lives of individuals in the sixteenth and seventeenth centuries (Amussen, 1988; Roper, 1989; Wiesner, 2000). Everyday life was structured around a male-dominated household where each member had his or her own individual roles to perform. If those said roles were not executed, -- for instance if a woman went against the authority of her husband, father or brother -- then disorder ensued. From the patriarchal perspective, disorder was to be avoided at all costs (Amussen, 1988).

The subordination of women to men was seen as the most natural of social hierarchies, and the performance of specific gender roles was what held early modern Scottish and English society together and allowed it to function as it should in accordance with the dominate patriarchy (Lake and Questier, 2002). Upon the death of her father in 1558 and her subsequent marriage, Euphame MacCalzean was under the authority of her husband, Patrick Moscrop. Frequently during her trial her marital behavior was brought into question, and as the charges against her suggest, MacCalzean’s

relationship with her husband was not typical. In fact, her husband was so frightened of her, he left Scotland for France. Constantly sick in her presence (supposedly from poison), he was incapable of exerting his authority over his own wife and so fled (Normand and Roberts, 2000). Their dysfunctional marriage was certainly not a representation of the expected early modern relationship between husband and wife, and for this reason, Euphame MacCalzean incurred a large amount of resentment from her male contemporaries.

As the only child of Thomas MacCalzean, Euphame stood to inherit, and did inherit, all of his lands and income after his death. It can be argued that the MacCalzean pattern of inheritance had significant economic implications that deviated from traditional gender arrangements. According to witchcraft historian Carol Karlsen, women with no brothers or sons were even more likely to be arrested, tried, and executed for witchcraft than women whose property was passed down to an acceptable male authority (Karlsen, 1987). Not only was MacCalzean the only inheritor of her father’s estate, but after her death, the MacCalzean wealth would go to her three daughters: Martha, Elizabeth, and Euphame MacCalzean (“Act”, 1592). Euphame and her daughters stood in the way of the conventional ordered succession of wealth and property from one generation of men to another. According to property law in the early modern period, women were allowed to inherit property, but ultimately that property would be under the control of their husbands when they wed (Braddick and Walter, 2001). With women having no independent legal rights, it was the right of the husband to control the property as he saw fit (Erickson, 1993; Sanderson, 2002). However, Patrick Moscrop’s flight to France left Euphame alone and virtually in control of the MacCalzean estate, until her arrest for witchcraft. Only after her conviction did Patrick return to Scotland to claim the property that should have, in ordinary circumstances, been rightfully his upon marriage (Normand and Roberts, 2000).

Interestingly, along with marital strife, conflicts concerning her daughters’ marriage arrangements surfaced in MacCalzean’s trial. Evidence of her influence in the community is more apparent when examining several accusations relating to the bewitchment of certain young men, young men she desired her daughters to marry. She was accused of “devilish witchcraft, enchantment, and incantation;”

forcing “Joseph Douglas of Pumpherston to love [her] under color and cloak of marriage with [her] daughter” (Normand and Roberts, 2000). Such a charge could stem from MacCalzean’s attempt to exercise her social power. By making advantageous marriages with certain Edinburgh families, she could further her own family’s influence both socially and politically since several men linked to MacCalzean were high officials and court advocates. Indeed, as laird of Pumpherston, Joseph Douglas was a prominent member of Scottish society, and MacCalzean’s intent to marry him to one of her daughters and solidify the continuation of her family’s power angered many people in her community, especially certain relatives that wanted to be rid of her persistent influence.

A close examination of MacCalzean’s trial records shows that 23 out of the 28 charges brought against her came from her own relatives and neighbors, both immediate and distant. In fact, the majority of the accusations came from two major sources: the Moscrop family (her in-laws, including David Seton) and her uncle, Henry MacCalzean. Almost all of allegations leveled against Euphame accused her of violence of some sort against her husband, brother-in-law, father-in-law, uncle, etc. (Normand and Roberts, 2000). Though each of the charges mentions some form of witchcraft or another, the underlying domestic conflicts are apparent. Indeed, 33 years before she was accused of witchcraft, MacCalzean had been taken to court to defend her lands and inheritance against claims by her uncle, who felt his brother’s property was rightfully his (Normand and Roberts, 2000). MacCalzean won the case and retained her father’s land, but certainly resentments would have lingered among those members of her family who felt they had been “cheated” out of an incredibly large inheritance. This previous property dispute and the persistent accusatory involvement of her family suggests that those bitter anxieties over Euphame MacCalzean’s wealth and inheritance were at the root of the witchcraft accusations brought against her three decades later.

Euphame MacCalzean’s trial began on June 9, 1591, and lasted until the fifteenth. In comparison to other witchcraft trials during that period, MacCalzean’s was unusually prolonged, but in regards to the execution of her sentence, her death was decidedly quick. She was brought to court, tried, and executed in the span of two weeks. Geillis Duncan, who was accused several months before MacCalzean, was not executed until December 1591, six months after MacCalzean was burned alive (Normand and Roberts, 2000). Though her lawyers argued with the court for three days she was found guilty on the twelfth of June. She was not convicted on the alleged attempted murder of her husband, but was found guilty of crimes including witchcraft, consultation with witches, the murder of her husband’s nephew, and the bewitchment of her father-in-law, John Moscrop (Normand and Roberts, 2000). The judge ordered her to be burned alive and all of her estates forfeited to the crown.

After her execution, several of her advocates attempted vehemently to have her name expunged. David Ogilvy, in particular, who had been one of the spokesmen for Euphame at her trial, took it upon himself to clear her name. Before the execution of the servant woman, Geillis Duncan, Ogilvy was granted an interview. Duncan confessed that she had never known MacCalzean and had no knowledge of her ever engaging in witchcraft. Ogilvy’s story was corroborated when, at Duncan’s execution on December 5, 1591, she announced to the public:

As she should answer on her soul and conscience before God, that she never knew the said Euphame MacCalzean to be any witch or to use any point of sorcery or witchcraft in any of the places foresaid... that she knew not of any vice or crime done by her at any time bygone... She was caused and persuaded to do so by David Seton in Tranent and others, and that it was all but lies, of the which she craved God’s forgiveness (Normand and Roberts, 2000, 198).



If Duncan's confession can be taken as the truth, then it was David Seton who forced her to name MacCalzean as a witch. No evidence suggests that Euphame MacCalzean had participated in witchcraft or sorcery of any kind. From all accounts, she was innocent of the charges brought against her, a point made evident when her estate was returned to her daughters and her name expunged less than a year after her execution.

The legal reversal of MacCalzean's conviction was issued by King James I of England in 1592. James authorized a parliamentary act entitled "Act in Favour of the Heirs of Euphame MacCalzean" on April 3rd of that year, approximately ten months after MacCalzean had been brutally executed on Castle Hill. The act not only fully reinstated MacCalzean's original estate to her daughters, but also cleared her name from any and all accusations of witchcraft. However, the act also re-established the dominant male hierarchy by shifting the authority over the estate to the men responsible for these women (*Act*, 1592).

According to the Act, Patrick Moscrop, the husband of Euphame MacCalzean, was the lawful administrator of the portions of her estate that belonged to his two youngest daughters, Elizabeth and Euphame. As for Martha MacCalzean, or Martha Ogilvy as she is referred to, her segment of the estate falls under the administration of her husband. Martha's new husband, David Ogilvy, was the very same David Ogilvy that served as an advocate for Euphame MacCalzean during her trial, the same man that worked so diligently to have his client's name expunged after her execution. As a result of the act, the Moscrop family, through the influence of Patrick Moscrop was in control of two-thirds of the MacCalzean estate, the other third going to David Ogilvy.

The fact that the MacCalzean estate was now under the appropriate control of male members of society could explain why Euphame's conviction was quickly overturned without any opposition. More importantly, the Moscrop family, the notorious in-laws who attacked

Euphame during her trial, were finally successful in their quest to control the MacCalzean estate. Certainly, there is a strong amount of evidence to suggest that Euphame MacCalzean's extended family used the accusation of witchcraft and the surrounding North Berwick panics to remove her influence and set the gender hierarchy to rights. An enormously prosperous estate was back under the influence of powerful men, men which included Patrick Moscrop, John Moscrop, and even David Seton.

Scholars have pointed to many various reasons for the emergence of witchcraft panics, including the most obvious explanation: the actual fear and belief in witchcraft. However the possibility of economic motivations, along with the persistent threat powerful women posed to a male-dominated society, and the fear of change in the gender hierarchy cannot be ignored. Euphame MacCalzean remains a prime example of those issues. While there are certainly other possible explanations for the emergence of the witch-craze in Scotland in the late-sixteenth century, evidence taken from the case of Euphame MacCalzean suggests that fear of female power and economic dominance could have played a crucial role in tensions that led to witchcraft accusations. As historians have argued, deviations in the social order would have alarmed those that clung to the traditional patriarchal system. The late sixteenth century was seeing the first signs of changes in that social structure and MacCalzean's case is an example of the conflict between the old and new orders. Certainly, feelings of dissatisfaction, anger, spite, and jealousy were understandable responses to the stresses of social and economic change, and, unfortunately, Euphame MacCalzean was a casualty of those emerging transformations.

References

Primary Sources:

“Act in favour of the heirs of Euphame MacCalzean, containing an exception for the lands of Cliftonhall and another exception to Master John Nicolson, advocate.” *The Records of the Parliaments of Scotland to 1707*. Edinburgh: April 1592. <http://www.rps.ac.uk/>. (Accessed 15 September 2012.)

Normand, L. and G. Roberts, (Eds.). (2000). Selected documents in *Witchcraft in Early Modern Scotland: James VI's Demonology and the North Berwick Witches*. Exeter, U. K.: University of Exeter Press.

Secondary Sources:

Adam, I. (1978). *Witch Hunt: The Great Scottish Witchcraft Trials of 1697*. London: Macmillan.

Amussen, S. D. (1988). *An Ordered Society: Gender and Class in Early Modern England*. Oxford: Basil Blackwell.

Braddick, M. J. and J. Walter, (Eds.). (2001). *Negotiating Power in Early Modern Society: Order, Hierarchy, and Subordination in Britain and Ireland*. New York: Cambridge University Press.

Erickson, A. L. (1993). *Women and Property in Early Modern England*. London: Routledge Publishing.

Karlsen, C. F. (1987). *The Devil in the Shape of a Woman: Witchcraft in Colonial New England*. New York: W. W. Norton & Company.

Lake, P. and M. Questier. (2002). *The Antichrist's Lewd Hat: Protestants, Papists and Players in Post-Reformation England*. New Haven, C. T.: Yale University Press.

Roper, L. (1989). *The Holy Household: Religion, Morals and Order in Reformation Augsburg*. Oxford: Clarendon Press.

Sanderson, M. H. B. (2002). *A Kindly Place? Living in Sixteenth Century Scotland*. East Linton, U. K.: Tuckwell Press.

Seth, R. (1969). *In the Name of the Devil: Great Scottish Witchcraft Cases*. London: Jarrolds.

Yeoman, L. (2002). “Hunting the rich witch in Scotland: High-status witchcraft suspects and their persecutors, 1590-1650,” in J. Goodare (Ed.), *The Scottish Witch-hunt in Context*. Manchester, U. K.: Manchester University Press, 106-121.

Wiesner, M. E. (2000). *Women and Gender in Early Modern Europe*. New York: Cambridge University Press.

Precision of the Neubauer Hemocytometer in Quantifying Concentration of Canine Spermatozoa Within and Between Operators of Differing Experience Levels

Kaitlyn Caraway, Robyn Wilborn, Aime Johnson, Jay Barrett, Todd Steury

Abstract

The importance of measuring accurately and precisely the concentration of spermatozoa in semen is increasing as artificial insemination becomes widely practiced in veterinary medicine. This study tested the precision of the Neubauer hemocytometer with canine spermatozoa of varying concentrations within and between operators of different experience levels (Figure 1). We calculated the standard deviation in estimates of spermatozoa concentration between two chambers of each hemocytometer and between replicate samples from the same ejaculate for both an experienced operator and an inexperienced one. The Neubauer

hemocytometer precision was also evaluated across varying concentrations of spermatozoa. We determined that the operator's experience level did not have a significant effect on precision when using the Neubauer hemocytometer. For both the experienced and inexperienced operator, the standard deviations between the two chambers of the hemocytometer and between replicate samples were 10.22 (± 1.22) million spermatozoa and 10.33 (± 2.16) million spermatozoa, respectively. Both these deviations exceeded 10 million spermatozoa, which many veterinarians consider to be significant when calculating a semen dosage for artificial insemina-

tion. However, this degree of deviation was present within the estimates of both operators, implying that it was not an effect of operator experience or expertise, but rather an inherent risk in using the hemocytometer.

Introduction

The analysis of concentration of spermatozoa in canine semen samples is becoming popular with the increased use of artificial insemination (AI) in veterinary medicine (Hansen et al., 2006). Accurately measuring the concentration of spermatozoa of a semen sample is important because it allows veterinarians to determine how many breeding dosages can be obtained from a single ejaculate. Common dogma is that at least 150 to 200 million progressively motile spermatozoa are recommended per insemination dose, but this number can vary greatly depending on the type of semen used (fresh, chilled or frozen) (Linde-Forsberg, 1991) and even the size of the dog breed. For example, an adequate breeding dose for a toy breed (e.g. Chihuahua, expected litter size of 2 to 4 puppies) requires much fewer progressively



Figure 1. Microscopic (400x) image of a canine spermatozoa on a hemocytometer grid.

motile spermatozoa than a breeding dose for a giant breed (e.g. Great Dane, expected litter size of 9 to 12 puppies), which correlates to size of the male testes of the corresponding breeds (Amann, 1986). This calculation of breeding doses is especially important with limited quantities of frozen semen from a valuable animal.

For this study, we chose to evaluate the Neubauer hemocytometer because it is the oldest, most common, and simplest method of measuring the concentration of spermatozoa cells in a sample (Kuster, 2005). For quantifying the spermatozoa concentration in semen samples, the Neubauer hemocytometer has long been considered the standard by the World Health Organization (WHO) (Cooper, 2010). It is the standard method for quantifying boar semen (Hansen et al., 2006), bull semen (Atiq et al., 2011), stallion semen (Samper, 2000), goat semen (Leboeuf et al., 2000), and human semen (Cooper, 2010). The hemocytometer has two chambers with a total area of 1.0 mm² on each end where the spermatozoa cells are counted. A coverslip sits 0.1 mm off the grid, allowing a diluted semen sample (1:100 dilution) volume of 0.1µl (Cooper, 2010). All spermatozoa cells within this area are counted manually under a microscope to quantify the concentration as millions of spermatozoa cells per milliliter, and the two chambers are averaged to obtain a spermatozoa concentration reading for that hemocytometer. The hemocytometer is cost-effective and relatively simple to use. However, it is much more time-consuming compared to other methods of quantification.

While computer-automated semen analysis (CASA) methods have become very popular in recent years

to increase efficiency, these methods are influenced by the Segre-Silberberg (SS) effect. The SS effect causes the spermatozoa to be pulled through the chamber faster and drives them toward the walls of the chamber, causing an underestimation of the concentration of spermatozoa, particularly in thin, capillary-loaded slides. This phenomenon was seen when analyzing human and boar semen samples on the CASA machine, but was not seen with the hemocytometer. It is believed that the SS effect does not have time to develop in the hemocytometer due to the increased chamber depth, as compared to the CASA slides (Cooper, 2010).

One large source of error with using the Neubauer hemocytometer is that the operator must manually count cells. Consequently, an operator that is experienced with the hemocytometer, microscopes, and the identification and counting of spermatozoa cells should be able to obtain accurate and precise results. However, pipetting errors, clumping of spermatozoa cells, and variations in the size of the drop dispensed into each chamber could all create variations in spermatozoa count estimates between chambers in the hemocytometer and between replicate samples from the same ejaculate. For example, if the operator dispenses a small drop into one chamber of the hemocytometer and a large drop into the other, a large standard deviation will result in the estimated concentration of spermatozoa averaged across chambers of the hemocytometer. Such errors could be exacerbated by untrained operators and lead to clinical mistakes. The main goal of this study

was to determine whether these errors coincide with the operator's level of experience.

Accuracy and precision are two terms used to describe a group of estimates. Accuracy is a measure of an estimate's closeness to the true value, and precision is a measure of how close a estimates in a group are to each other, regardless of how close they are to the true value. While it would be valuable to quantify the accuracy of the hemocytometer, doing so requires knowing the true values. For the purposes of this study, accuracy was not questioned. However, precision of the hemocytometer can readily be estimated by comparing multiple values from the same sample (ejaculate), including replicates by the same operator as well as another operator. For this study, we determine the standard deviation (i.e., precision) of estimates of spermatozoa concentration between chambers of the hemocytometer and between replicate samples from a given ejaculate, as influenced by the degree of operator experience.

Experimental Design

One hundred different samples (ejaculates) were obtained from a total of eighteen different dogs. The dog breeds used were Labrador Retrievers (8), Beagle (1), English Pointers (2), and Beagle-Corgi crosses (7). Dogs ranged from one to seven years of age with a mean of 4 years of age. All procedures were approved by the Auburn University Institutional Animal Care and Use Committee (IACUC #2009-1580).

“...the Neubauer hemocytometer has long been considered the standard by the World Health Organization.”

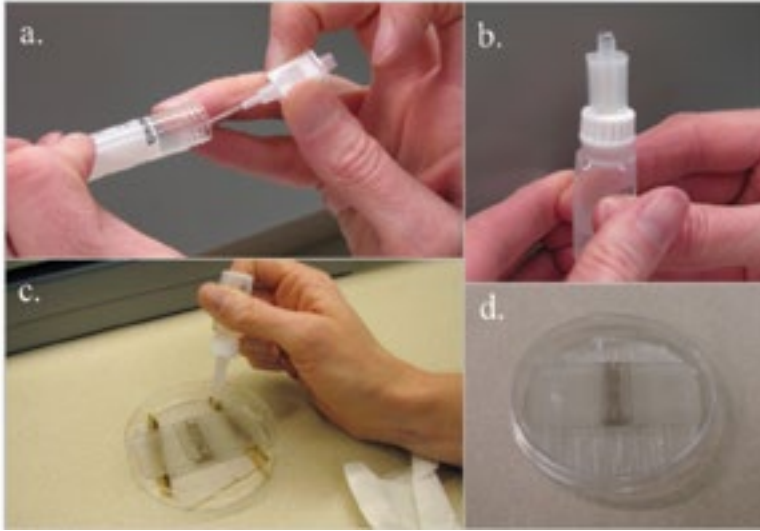


Figure 2. Method for preparing the Neubauer hemocytometer for this study: (a.) pipette is filled with 20 µl raw semen sample; (b.) sample is diluted 1:100 with reservoir mixture; (c.) each chamber of the hemocytometer is filled with 20 µl of raw sample (d.) loaded hemocytometer is incubated for four minutes in humidity chamber.

The inexperienced operator was trained in the proper use of the hemocytometer for a total of two hours. During this time, hands-on instruction was provided, and two practice samples, not included in the data collection, were counted. Proper procedure was posted

in the laboratory so that the inexperienced operator could quickly refer to protocol at any time, but no further hands-on instruction was provided.

Each ejaculate was quantified on a total of four hemocytometers, two by an experienced operator and two by an inexperienced one to obtain an inter-chamber and inter-replicate standard deviation for each operator. Both chambers of the hemocytometer were counted separately by each operator and averaged to provide an inter-chamber mean. This mean represents the concentration of spermatozoa for that hemocytometer. An estimate of the inter-chamber standard deviation was calculated from the individual counts of the two chambers. Each operator repeated this process a second time using the same raw ejaculate. The spermatozoa

counts representing each hemocytometer of the same ejaculate were then statistically averaged to obtain an inter-replicate mean. An estimate of the inter-replicate standard deviation was calculated from the averaged counts generated from the two replicates.

The mean concentration of each individual ejaculate as measured by each operator was grouped into three concentration categories that represent realistic spermatozoa concentrations in canines: <100 million cells/ml, 100 – 200 million cells/ml, and >200 million cells/ml. The standard deviation within each concentration category was analyzed to determine at which concentration the hemocytometer was the most precise.

Materials and Methods

Neubauer Hemocytometer

Each operator followed a standard procedure for preparing each Neubauer hemocytometer (Figure 2). A 1.98 ml unopette reservoir and 20 µl capillary pipette were obtained. The spear end of the capillary pipette

was used to create a hole in the top of the reservoir and then discarded. The raw semen sample was inverted three times to ensure homogenization, and the pipette was filled with 20 µl of the semen sample via capillary action. The pipette was then placed pipette end down into the reservoir, and a meniscus was made three times to ensure even mixing between the semen sample and reservoir mixture, resulting in a 1:100 dilution ratio. After allowing the reservoir and semen mixture to equilibrate undisturbed for ten minutes, it was then used to fill the chambers of the hemocytometer. This was accomplished by inverting the pipette and turning the reservoir upside down to dispense one full drop of the mixture (20 µl) into each chamber of the hemocytometer. Once both chambers were filled, the hemocytometer incubated for four minutes in a humidity chamber. This incubation period allows the sample to settle, while also preventing evaporation of the fluid. The hemocytometers were then counted using the method stated in the previous section.

Table 1. Standard deviation between experienced and inexperienced operators and among varying concentrations.

	Inter-chamber		Inter-replicates
Average Standard Deviation	10.22 (±1.22)		10.33 (±2.16)
Operator Difference	Inexperienced 1.97 (±2.03) higher		Inexperienced 2.80 (±1.96) higher
	<100 million cells/ml	100-200 million cells/ml	>200 million cells/ml
Average Standard Deviation	3.96 (± 0.58)	13.68 (±2.95)	29.16 (±11.52)

Statistical Analysis

A linear mixed-effects model was used to statistically compare the standard deviation in inter-chamber spermatozoa counts, as well as inter-replicate spermatozoa counts, between the experienced and inexperienced operators. Thus, in these models, the response variables were either the estimated standard deviation in inter-chamber spermatozoa or the estimated standard deviation in inter-replicate spermatozoa counts; the dependent variable was the operator experience level, and a random effect of ejaculate was included in these models as a blocking factor. A separate, similar mixed-effects model was used to compare the standard deviation between sperm count categories for the inter-replicate counts.

Results

The results of the precision tests are summarized in Table 1. The standard deviation in estimated spermatozoa concentration between chambers of the hemocytometer run by both the experienced and inexperienced operator averaged 10.22 (± 1.22) million spermatozoa with a 95%

confidence interval (C.I.). Standard deviation in estimated spermatozoa concentration between the two chambers of the hemocytometer averaged 1.97 (± 2.03; 95% C.I.) million spermatozoa higher for the inexperienced operator relative to the experienced operator; however, differences were not statistically significant at the $\alpha = 0.05$ level ($t_{281} = 1.90, p = 0.058$).

Standard deviation in estimated concentration of spermatozoa between replicate samples for all ejaculates run by both the experienced and inexperienced operator averaged 10.33 (± 2.16; 95% C.I.) million spermatozoa. Standard deviation in estimated spermatozoa concentration between replicate samples of the hemocytometer was estimated to be 2.80 (± 1.96; 95% C.I.) million spermatozoa higher for the inexperienced operator relative to the experienced operator; however, differences were not significant ($t_{99} = 1.43, p = 0.1562$).

When the sample concentration averaged less than 100 million cells/ml, the standard deviation was 3.96 (± 0.58; 95% C.I.) million spermatozoa cells. The standard deviation for a sample concentration between 100

and 200 million cells/ml was 13.68 (± 2.95; 95% C.I.) million spermatozoa cells, and the standard deviation for a concentration over 200 million cells/ml was 29.16 (± 11.52; 95% C.I.) million spermatozoa cells. The categorical grouping of spermatozoa concentration was a significant predictor of standard deviation in spermatozoa counts ($F_{2, 98} = 43.29, p < 0.0001$), with all three categories significantly different from each other (all $t_{98} > 4.67, p < 0.0001$).

Discussion

Results indicate that even between the two chambers of a hemocytometer slide, estimated concentration of spermatozoa can easily vary by as much as 20 million spermatozoa from the mean. Similarly, even after minimizing such variation by using averages of both chambers, estimated spermatozoa concentration can vary between replicate samples by as much as 20 million spermatozoa from the mean. Although there is not a well-documented benchmark for a measure of clinical significance, an error of ≥ 15 million cells/ml is considered by some veterinarians to be a costly clinical mistake in canine reproduction (Wilborn,

personal communication). If sample concentration is overestimated, too few spermatozoa may be used for an insemination dose, resulting in lower pregnancy rates and reduced litter sizes. On the other hand, when sample concentration is underestimated, too many spermatozoa may be used for an insemination dose, and valuable semen that could have otherwise been used on an additional female may be wasted.

There was no significant difference between the precision of either inter-chamber counts or

inter-replicate counts when run by an experienced operator versus an inexperienced operator. From a clinical standpoint, this is very important. Veterinarians are more efficient when time-consuming tests such as this one can be reliably performed by support staff such as veterinary assistants or technicians. Many veterinary practices have significant turnover in support staff and experience level varies greatly among these individuals. Therefore, it is critical to have a method of quantification that is highly repeatable with little training required.

In summary, the Neubauer hemocytometer is a simple method for determining the concentration of canine spermatozoa. Although this method is considered the standard for accuracy, precision did vary and could contribute to clinical errors when calculating breeding doses for canine artificial insemination. The level of operator experience did not have a significant effect on results, indicating that this method would lend itself to use by properly trained veterinary support staff with results comparable to those achieved by the veterinarian.

References

- Amann, R. P. (1986). Reproductive physiology and endocrinology of the dog. *in* D.A. Morrow (Ed.). *In Current Therapy in Theriogenology 2: Diagnosis, Treatment and Prevention of Reproductive Diseases in Small and Large Animals*. Philadelphia, PA.: W.B. Saunders, 532-538.
- Atiq, N., N. Ullah, S. M. H. Andrabi, and S. Akhter (2011). Comparison of photometer with improved Neubauer hemocytometer and Makler counting chamber for sperm concentration measurement in cattle. *Pakistan Veterinary Journal*: 31 (1), 83-84.
- Cooper, T. G. (2010). *WHO Laboratory Manual for the Examination and Processing of Human Semen*, Fifth Edition. WHO Press: Geneva, Switzerland.
- Hansen, C., T. Vermeiden, J. P. W. Vermeiden, C. Simmet, B. C. Day, and H. Feitsma (2006). Comparison of FACSCount AF system, improved Neubauer hemocytometer, Corning 254 photometer, SpermVision, UltiMate and NucleoCounter SP-100 for determination of sperm concentration of boar semen. *Theriogenology*: 66 (1), 2188-2194.
- Kuster, C. (2005). Sperm concentration determination between hemocytometric and CASA systems: why they can be different. *Theriogenology*: 64 (3), 614-7.
- Leboeuf, B., B. Restall, and S. Salamon (2000). Production and storage of goat semen for artificial insemination. *Animal Reproduction Science*: 62 (1-3), 113-141.
- Linde-Forsberg, C. (1991). Achieving canine pregnancy by using frozen or chilled extended semen. *Veterinary Clinics of North America: Small Animal Practice*: 21 (1), 467-485.
- Samper, E. (2000). *Equine Breeding Management and Artificial Insemination*, Second Edition. Philadelphia, PA.: W.B. Saunders.
- Wilborn, R. Personal interview. 11 November 2012.

Acknowledgments

The authors would like to thank Drs. Bruce Smith and Rob Gillette for the use of the dogs, as well as Sara Beth Griffin and Steve Waters for their assistance with the animals.

Frictional Properties of Ground Loblolly Pine Chips

Jacob Wadkins, Anshu Shrestha, Oladiran Fasina, Sushil Adhikari, Steven Taylor

Abstract

Biomass, such as ground wood chips, is a bulk material and therefore has the typical flow problems associated with bulk materials. The frictional properties (cohesion, flow index, and angle of internal friction) of ground loblolly pine chips obtained from different harvesting operations (clean chips, dirty chips, and residues) and ground through 1.588 mm and 3.175 mm screens were measured. Grinding screen size did not significantly affect ($P < 0.05$) the frictional properties of the samples. Cohesive strength and flow index of ground clean chips and dirty chips were significantly higher than those of ground residues. Based on flowability classification, the flow index value of 3.53 obtained for ground residues indicates that it has a cohesive flow behavior. Ground clean and dirty chips have easy flow behavior (flow index is 4.36). The angles of internal friction for ground clean chips, dirty chips, and residues were 45.2°, 44.9° and 46.2° respectively. The higher values of ash, cohesive strength, angle of internal friction, and flow index for the residues indicate that special handling and processing operations have to be carried out on the residues before they can be utilized in bioenergy applications.

Introduction

The South is the primary wood-producing region of the United States. Forestland covers 156 million acres or 60 percent of the land area in the southeastern part of the country (<http://fia.fs.fed.us/>). Over 60 percent of U.S. timber production comes from southern forests with loblolly pine being the most predominant wood species grown. With a decline in the pulp and paper manufacturing industry and in the solid wood products sectors due to reductions in housing construction, a significant amount of wood is available as biomass feedstocks for production of bioenergy, biofuels, and bioproducts (Frederick et al., 2008). Loblolly pine is the biomass feedstock that is predominantly available in the forestland of the southern part of the U.S. The three different products that are typically obtained from forest logging and chipping operations are: 'clean' chips, 'dirty' chips, and residues. Clean chips are produced from the stems of debarked wood. Dirty chips are chips produced from entire trees and typically include the stem, bark, branch wood, and leaves/needles. Residues are the unused parts above the stumps of harvested trees including live standing or downed trees that are left on site after logging. To facilitate heat and mass transfer during bioenergy conversion processes,

harvested trees need to be ground before they are fed into conversion equipment at the biorefinery plants. When trees are harvested, they are typically chipped into 25 to 50 mm sizes. Wood grinds are produced at the bioenergy conversion facility by grinding the chips into sizes of 1.0 to 6.0 mm with a hammer mill. The final grind size depends on the bioenergy conversion process and the technology used. Direct grinding of trees is currently not a common practice because of the logistics of grinding on the forest land.

Since wood grinds are bulky in nature, they have flow problems that are typically exhibited by bulk materials. Core flow (as shown in Figure 1) is the default flow pattern out of storage containers, holding containers, and drying vessels for powder-like materials such as wood grinds. This flow pattern is characterized by powder discharge through a preferential flow channel that starts from the top of the stored material and results in a first-in/last-out discharge. The result is unreliable and inconsistent flow, and/or no flow caused by cohesive arching or the formation of a stable rathole (Iqbal and Fitzpatrick, 2006). Another problem with core flow is that powder around the walls and in the lower sections of the container remains there until the container is emptied. During 'mass'

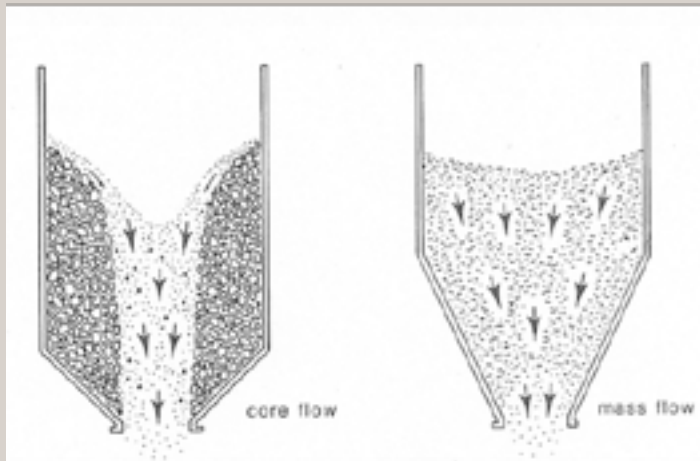


Figure 1. Patterns of discharge from hoppers (Woodcock and Mason, 1988).

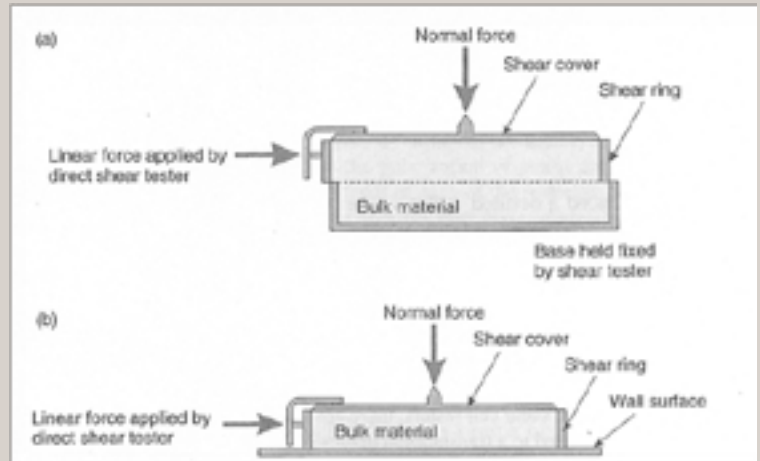


Figure 2. Jenike shear tester modes of operation for measuring (a) flow function, (b) wall friction characteristics (Fitzpatrick, 2005).

flow, all of the material in the bin is in motion (i.e., there is 'mass' movement – Figure 1) whenever the discharge outlet is opened resulting in first-in/first-out flow sequence. This flow pattern is especially desirable for cohesive solids and fine powders that are typically poor-flowing because all of the material in the bin is in motion. The result is consistent and there is reliable flow from these containers (Iqbal and Fitzpatrick, 2006). Other advantages of mass flow include an absence of surging and flooding and minimum segregation of stored products (Roberts, 2005). Process optimization in biorefineries, such as gasification plants, requires a reliable flow from these containers. Unlike the core flow pattern that naturally occurs, special design considerations must be made for the mass flow pattern to occur. Flow properties (such as the angle of internal friction, flow index, and cohesive strength) are used to design hopper angles and outlet diameters necessary for mass flow of powder-like materials such as wood grinds.

Frictional (or flow) properties of powder-like materials are usually determined with a translational or rotational

shear tester that generally involves applying shear force to a material until the material fails (McGlinchey, 2005). In a translational shear tester (often referred to as the Jenike shear tester), the bulk solid specimen is subjected to a normal stress. The material is then sheared by applying a gradually increasing horizontal force on the upper side of the shear cell. This causes the upper side of the shear cell to move relative to its lower side (i.e., shearing of the sample placed in the shear cell – Figure 2). A shear tester in which the relative displacement is achieved by rotation of the top of the bulk solid specimen relative to the bottom is called a rotational shear tester (Schulze, 2008). The rotational shear cell tester was initially developed to overcome the limited shear displacement that can be achieved with the Jenike shear tester. A more detailed description of the two shear tester types can be found in Jenike (1964) and in Barbosa-Cánova et al. (2005). A yield locus curve is obtained from the shear stress test. The curve is a plot of the shear stress required to cause sample failure versus the normal stress applied. The angle of internal friction and

cohesive strength of the materials are obtained from the slope and intercept of the yield locus curve respectively. Wall friction properties are measured by replacing the base of a shear cell with a plate of the material that will be used to manufacture the hopper or storage container.

The angle of internal friction measures the friction between solid particles flowing against each other. Cohesive strength is a measure of the force of attraction or bonding tendency between particles of a bulk material (Bernhart and Fasina, 2009). Flow index is used to characterize the flowability of bulk materials (Table 1). The flow index is the inverse of the flow function obtained during flow behavior tests. The flow function is the slope of the plot of unconfined yield stress versus the major consolidating stress (Fitzpatrick et al., 2004). The plot is obtained by developing Mohr stress circles on the yield locus curves obtained for a sample at various consolidating stresses. In general, materials with a cohesion of less than 2 kPa and an angle of internal friction of less than 30° are amenable to handling using gravity alone (Puri, 2002).

Factors that have been documented to affect these flow properties include particle size, moisture content, and material composition (Fasina, 2006; Zulfiqar et al., 2006). The objective of this study was to measure the physical and frictional properties of wood grinds from loblolly pine clean chips, dirty chips, and residues.

Materials and Methods

Wood chips from different harvesting operations (clean chips, dirty chips, and residues left on field after harvesting) were ground through two screen sizes (1/8" and 1/16") using a hammer mill (Glenn Mills Inc., Clifton, NJ). Ash, moisture, and volatile contents of the samples were analyzed according to ASTM Standard E1755 (ASTM, 2007), ASTM Standard E1756 (ASTM, 2008) and ISO Standard 562 (ISO, 2010) respectively. An IKA C200 bomb calorimeter (IKA Works Inc., Wilmington, NC) was used to measure the heating value of the samples. Physical properties of the ground samples that were quantified were particle density (Model 1340, Micromeritics Instrument Corp, Norcross, GA) and bulk density (Fasina, 2006). Average particle size was based on the equivalent sphere approach (i.e., diameter of the sphere that has a volume equivalent to the average volume of the particles) and was measured by a digital image particle analyzer (Camsizer, Retsch Technology, Haan, Germany).

A rotational type powder flow tester (Brookfield Engineering Laboratories, Middleboro, CA) was used to measure the friction properties (flow index, cohesion, and angle of internal friction). The tester was operated by loading a sample into the space between the inner ring and the outer ring of a sample trough. After determining the mass of the loaded sample, the trough and its contents were placed on a flow tester already fitted with a vane lid. The software supplied by the equipment manufacturer was then used to run the flow function test. The software returned the values for the friction properties of the tested sample.

All of the above analyses were carried out in duplicate. Data analysis and plotting were carried out using Microsoft Excel software. Statistical analysis was performed on all data sets using SigmaPlot (version 12.3, Systat Software Inc., San Jose, CA) and SAS statistical software package (version 9.2, SAS Institute Inc., Cary, NC, 2011). Statistical testing was carried out at the 95% confidence interval.

Results and Discussion

Values of the physical and chemical characteristics of the ground loblolly pine wood chips are shown in Table 2. Statistical analysis using ANOVA and Duncan’s multiple range test showed that the physical properties (particle density, bulk density, and particle size) are significantly affected ($P < 0.05$) by material type and grinding screen size. As expected, the sample type significantly affected ($P < 0.05$) the chemical properties (ash, energy, and volatile contents) of the samples but screen size did not ($P > 0.15$). Energy and volatile contents of the ground residues samples were about 40% lower while the ash contents of the residues were several orders of magnitude higher than the corresponding values for ground samples from clean chips or from dirty chips. In addition, the ash contents of ground dirty chips samples were significantly higher than those of clean chips. Dirty chips contain leaves, bark, and branches that may have ash contents of up to 10% (based on other analysis).

Residues are being investigated for bioenergy utilization because residues left in the forest after biomass harvest impede forest regeneration, increase the risk of forest fire, and hinder recreational use. Current technology to gather and collect residues after logging operations often results in contamination of the residues with soil, hence the significantly higher ash contents and lower volatile contents of the residues as shown in Table 2. These results show that the potential use of residues in bioenergy is questionable unless processes to gather and collect them are improved such that soil contamination is minimized.

Table 1. Classification of powder flowability by flow index (Jenike, 1964).

	Very Cohesive	Cohesive	Easy Flowing	Free Flowing
Flow Index (FI)	FI < 2	2 < FI < 4	4 < FI < 10	FI > 10

RESULTS

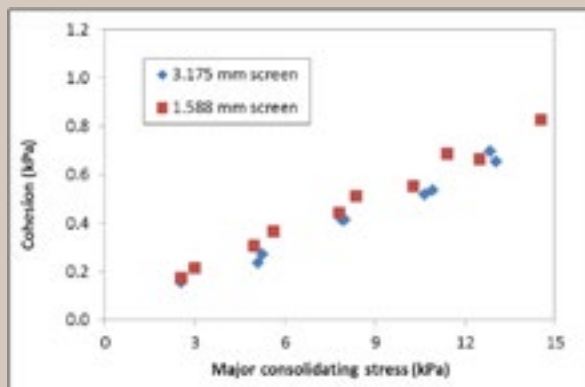


Figure 3. Effect of screen size on cohesion of clean wood chips ground through 1.588 mm and 3.175 mm screens.

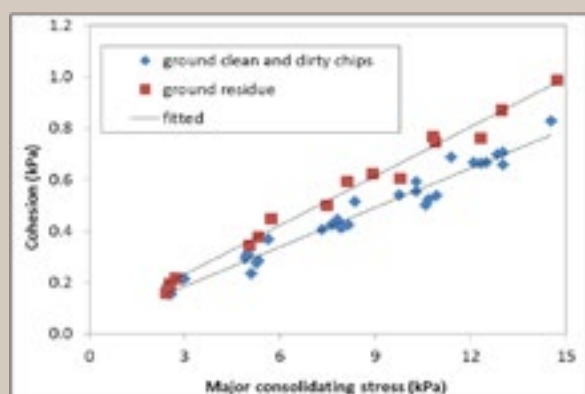


Figure 4. Fitted and experimental data of cohesion of ground clean and dirty wood chips, and residues.

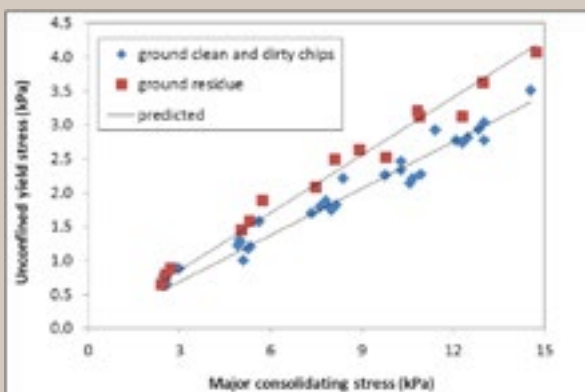


Figure 5. Unconfined yield stress versus major consolidating stress for ground clean and dirty chips, and residues.

Cohesive strength increased linearly with an increase in consolidating pressure as shown in Figure 3 for ground clean chips samples. A similar linear relationship was obtained for ground dirty chips and residues samples. Parallel line analysis in SigmaPlot showed that the linear relationships for all the samples were not significantly affected by size and that the ground clean chips and dirty chips were not significantly different from each other. Consequently, the cohesion data for ground samples from clean chips and dirty chips were pooled and a linear equation (Equation 1) was developed to relate their cohesive strength to major consolidating stress, σ_c (Figure 4). The corresponding equation for residues can be found in Equation 2.

Ground clean and dirty chips (through 1.588 mm and 3.175 mm screens)

$$C = 0.0509 \sigma_c + 0.0334 \quad R^2 = 0.9711 \quad (1)$$

Ground residues (through 1.588 mm and 3.175 mm screens)

$$C = 0.0637 \sigma_c + 0.0412 \quad R^2 = 0.9864 \quad (2)$$

For each feedstock type, the angle of internal friction of the ground sample was not significantly affected by size. However, the angle of internal friction for residues were significantly ($P < 0.05$) higher than those of clean chips or dirty chips. The average angles of internal friction were 44.9° , 45.2° , and 46.2° for the dirty, clean, and residues respectively. The implication is that this study and other related studies (Fasina, 2006; Chevanan et al., 2009; Bhadra et al., 2009) indicate that ground biomass materials do not meet one of the two criteria listed by Puri (2002) for gravity flow; i.e., the angle of internal friction is not less than 30° . Our laboratory is currently working on systems to reduce the angle of internal friction of biomass materials.

Statistical testing showed that screen size did not significantly affect the unconfined yield strength values at the different consolidating stresses for each of the three sample types.

This is similar to the results obtained by Fasina (2006) on the effect of screen size on strength behavior of peanut hull, switchgrass, and poultry litter. Similar to the cohesive strength results, the flow function of clean chips was not significantly different from that of dirty chips; however, the flow function of the residues were significantly different from those of clean chips and dirty chips. Consequently, the flow function data of clean chips and dirty chips were lumped together and a linear fit was used to relate the unconfined yield stress to the major consolidating stress (Figure 5). A separate linear fit was developed for the flow function data of the ground residues as given below.

Ground clean and dirty chips (ground through 1.588 mm and 3.175 mm screens)

$$UYS = 0.2296\sigma_c \quad R^2 = 0.9664 \quad (3)$$

Ground residues (ground through 1.588 mm and 3.175 mm screens)

$$UYS = 0.2836\sigma_c \quad R^2 = 0.9767 \quad (4)$$

The flow indices (obtained from the inverse of the slopes of Equations 3 and 4) for ground clean/dirty chips and for ground residues are 4.36 and 3.53 respectively. The flow indices indicate that the ground clean/dirty chips are easy flowing while the ground

residues are cohesive (see classification in Table 1). This result is not surprising because the residues have a higher angle of internal friction and a higher cohesive strength. The use of residues in bioenergy applications will therefore require special handling and discharge methods from silos and storage vessels before the material can be fed into biorefinery unit operation equipment.

Conclusion

It can be concluded from this study that the quality (based on ash, volatile, and energy content) of residues from forest harvest operations is significantly lower than those of clean chips or dirty chips. The presence of ground residues in forest-based feedstock destined for bioenergy applications may present flow problems in discharge hoppers and feeders. The flow index value of 3.53 for the ground residues indicates that it is cohesive in nature. The frictional properties of forest biomass feedstock were not significantly affected by grinding screen size (1.588 mm and 3.175 mm).

Table 2. Properties of ground wood chips affected by grinding screen size and sample type.

Property/screen size (mm)	Sample Source					
	Clean chips		Dirty chips		Residues	
	3.175	1.588	3.175	1.588	3.175	1.588
Energy content (J/g)	19705 ^{a*}	19549 ^a	20068 ^a	19546 ^a	12552 ^b	10378 ^b
Volatile content (%)	83.1 ^a	85.4 ^a	81.9 ^a	83.5 ^a	48.4 ^b	43.1 ^b
Ash content (%)	0.41 ^a	0.26 ^b	0.61 ^c	0.65 ^c	26.67 ^d	34.62 ^e
Particle density (kg/m ³)	1423 ^a	1438 ^b	1392 ^c	1410 ^d	1621 ^e	1727 ^f
Bulk density (kg/m ³)	217.1 ^a	225.9 ^b	260.0 ^c	236.0 ^d	275.4 ^e	353.6 ^f
Avg. particle size (mm)	1.335 ^a	1.179 ^b	1.230 ^c	0.928 ^d	0.699 ^e	0.557 ^f

*different letters in a row are significantly different at P < 0.05.

References

- ASTM. (2008). *ASTM Standard E1756. Standard test method for determination of total solids in biomass*. West Conshohocken, PA.: ASTM.
- ASTM. (2007). *ASTM Standard E1755: Standard test method for ash in biomass*. West Conshohocken, PA.: ASTM.
- Barbosa-Cánova, G. V., E. Ortega-Rivas, P. Juliano and H. Yan. (2005). *Food Powders: Physical Properties, Processing and Functionality*. New York, NY: Kluwer Academic Publishers.
- Bernhart, M. and O. O. Fasina. (2009). Moisture effect on the storage, handling and flow properties of poultry litter. *Waste Management: 29*, 1392-1398.
- Bhadra, R., K. Muthukumarappan, and K. A. Rosen-trater. (2009). Flowability properties of commercial distiller dried grains with solubles (DDGS). *Cereal Chemistry: 86*, 170-180.
- Chevanan, N., A. R. Womac, V. S. P. Bitra, D. C. Yoder, and S. Sokhansanj. (2009). Flowability parameters for chopped switchgrass, wheat straw and corn stover. *Powder Technology: 193*: 79-86.
- Fasina, O. O. (2006). Flow and physical properties of switchgrass, peanut hull and poultry litter. *Transactions of the ASABE: 49*, 721-728.
- Fitzpatrick, J. J. (2005). Food Powder Flowability, in C. Onwulata (Ed.), *Encapsulated and Powdered Foods*. Boca Raton, FL: CRC Press, 247-260.
- Fitzpatrick, J.J., S. A. Barringer and T. Iqbal. (2004). Flow property measurement of food powders and sensitivity of Jenike's hopper design methodology to the measured values. *Journal of Food Engineering: 61*, 399-405.
- Frederick, W. J. Jr., S. J. Lien, C. E. Courchene, N. A. DeMartini, A. J. Ragauskas, and K. Lisa. (2008). Co-production of ethanol and cellulose fiber from southern pine: a technical and economic assessment. *Bioresource Technology: 99*, 5051-5057.
- Iqbal, T. and J. J. Fitzpatrick. (2006). Effect of storage conditions on the wall friction characteristics of three food powders. *Journal of Food Engineering: 72*, 273-280.
- ISO. (2010). *ISO 562: Hard coal and coke – determination of volatile matter*. Geneva, Switzerland: ISO.
- Jenike, A. W. (1964). *Storage and Flow of Solids*. Bulletin No. 123. Salt Lake City, Utah: University of Utah Engineering Experiment Station.
- McGlinchey, D. (2005). Bulk Property Characterization, in D. McGlinchey (Ed.), *Characterization of Bulk Solids*. Boca Raton, FL: CRC Press, 48-84.
- Puri, V. M. (2002). Characterizing powder flowability. *Chemical Process: 65*, 39-42.
- Roberts, A. W. (2005). Characterization for Hopper and Stockpile Design. in D. McGlinchey (Ed.), *Characterization of Bulk Solids*. Boca Raton, FL: CRC Press, 85-131.
- Schulze, D. (2008). *Powders and Bulk Solids: Behavior, Characterization, Storage and Flow*. New York, NY: Springer.
- Woodcock, C. R. and J. S. Mason. (1988). *Bulk Solids Handling: An Introduction to the Practice and Technology*. New York, NY: Chapman and Hall.
- Zulfiqar, M., B. Moghtaderi, and T. Wall. (2006). Flow properties of biomass and coal blends. *Fuel Process Technology: 87*, 281-288.

Acknowledgments

We acknowledge support from the USDA funded Southern Partnership for Integrated Biomass Supply System (IBSS) that provided SEED fellowship for the first author.

Pathoadaptive Variants of *Pseudomonas aeruginosa*

Heather C. Eggleston, Sarah B. Chaney, Daniel J. Wozniak

Abstract

Pseudomonas aeruginosa is an opportunistic pathogen present in several chronic infections that exhibits resistance to antimicrobial therapy. *P. aeruginosa* exhibits increased resistance due to its ability to genetically adapt when confronted with the selective pressures of a chronic inflammatory environment. Though many studies have been performed that characterize these genetic adaptations, an *in vivo* model has not been developed to study the correlation between the levels of chronic inflammation and resulting genetic variants. Therefore, we developed a dermal wound porcine model to simulate chronic inflammation. The samples collected from this model were screened for phenotypic and genotypic diversification. The characteristics of the isolates identified from the model mirror the results of several *in vitro* studies and also present opportunities for characterization of new phenotypes. In particular, the successful isolation of mucoid variants is a standard indication of the progression to chronic infection. Through this model, we have developed an approach to understand the variants of *P. aeruginosa* induced by chronic inflammation to direct new antimicrobial therapies.

Introduction

The opportunistic pathogen, *P. aeruginosa* is present in several infections including those associated with urinary tracts, catheter and indwelling biodevices, chronic wounds, and respiratory tracts of cystic fibrosis (CF) patients. In fact, *P. aeruginosa* is the major pathogen involved in the respiratory infections of CF patients, and respiratory failure is the major cause of death in 95% of patients with CF (Baynham et al., 1999; Ramsey and Wozniak, 2005). Pathoadaptation is the mechanism by which opportunistic pathogens such as *P. aeruginosa* are able to persist in the inflammatory environment of a chronic infection. Pathoadaptation occurs when *P. aeruginosa* is exposed to components of the host immune system and antimicrobial therapies, resulting in an adaptation to this environment by diversifying into genetic and phenotypic variants with enhanced biofilm formation and antimicrobial resistance. Thus, *P. aeruginosa* has evolved into a paradigm of the study of bacterial evolution in the presence of antibiotic and innate host immunity pressures. By replicating the chronic inflammatory environment in a dermal wound model, we hoped to observe the genetic and phenotypic diversification of *P. aeruginosa* due to chronic inflammation. By controlling the length and treatment of infection, we hoped to create different levels of inflammation in order to discern the specific factors that produce particular variants. *P. aeruginosa* possesses several characteristics that allow it to persist in these chronic inflammatory environments (Mann and Wozniak, 2012). Common and important variants of *P. aeruginosa* include mucoid and rugose small colony variants. Mucoid variants of *P. aeruginosa* are characterized by an overproduction of the exopolysaccharide alginate, a non-repetitive partially O-acetylated polymer of D-β-1,4-mannuronic acid and α-L-guluronic acid, with a shiny, mucus like appearance *in vitro* (Ramsey and Wozniak, 2005). Two characteristics of alginate enhance the persistence of *P. aeruginosa*: intricate biofilm architecture and protection from



Figure 1. Illustration of porcine burn wound model. Boxes represent wounds; red and green triangles represent co-inoculation with PAO1 (*P. aeruginosa*) and 19606 (*A. baumannii*). Control wounds were inoculated with mock saline. Collection by punch biopsy occurred every 7, 9, 14, 28, or 35 days. Yellow boxes represent treatment by surgical debridement.

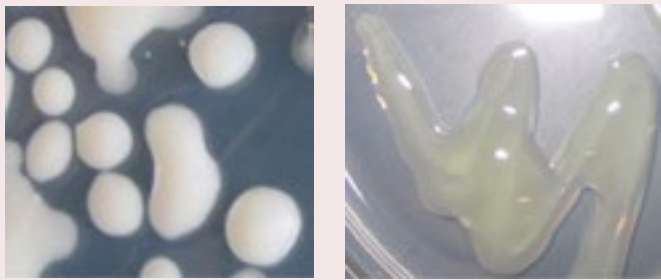


Figure 2. Mucoid colony morphology as determined by the appearance of opaque or green translucent colonies with thick, shiny secretions.

Figure 3. Mucoid clinical isolate FRD1 (left) streaked on 1/2X PIA. RSCV isolate MJK8 (right) streaked on VBMM agar.



the innate and adaptive immune systems. Biofilms containing the O-acetylated polymer of alginate exhibit a complex architecture, consisting of large microcolonies separated by water channels. In addition to this specialized biofilm structure, alginate scavenges free radicals released by activated macrophages *in vitro* and prevents neutrophil chemotaxis and complement activation (Ramsey and Wozniak, 2005). These characteristics explain why isolation of mucoid *P. aeruginosa* from the sputum samples of CF patients is associated with a worsening prognosis (Baynham et al., 1999). Rugose small colony variants (RSCV) have also been isolated from the chronic lung infections of CF patients. These variants possess an enhanced ability to form biofilms and therefore exhibit a greater resistance to antimicrobial treatment (Starkey et al., 2009). In this paper, we investigate the pathoadaptation of *P. aeruginosa* by screening for these phenotypic and genotypic variants in a chronic wound model.

Materials and Methods

Ex vivo samples from a chronic porcine burn wound model were screened for *P. aeruginosa* genetic and phenotypic variants (Figure 1). In this model, wounds are co-inoculated with wild type *P. aeruginosa*, PAO1, and *Acinetobacter baumannii*, strain 19606. Three randomly distributed punch biopsies from a wound were collected at time points of 7, 9, 14, 28, or 35 days. The collected tissue was homogenized and banked frozen at -80°C with 10% skim milk. Both control-mock saline inoculated and experimental bacterial inoculated samples were screened (n = 175). Each homogenate was thawed and then diluted using 1X PBS buffer. Dilutions ranged

from 10^1 to 10^{-6} depending upon the previously determined colony forming units (CFU) of the sample. All samples were grown at 37°C. Each sample was initially plated onto 1/2X *Pseudomonas* Isolation Agar (PIA). Colonies with the morphological characteristics of mucoid or rugose small colony variants (RSCV) were plated onto Vogel-Bonner Minimal Medium agar (VBMM) (Moody and Hassan, 1982). Colonies that absorbed Congo red dye from the VBMM agar were streaked for isolation. Colonies that demonstrated a distinct phenotype on VBMM were grown overnight in 5 mL of Lysogeny broth (LB) or LB with no NaCl. DNA was isolated from the resulting culture by following the Wizard Genomic DNA Purification Kit protocol (Promega). Polymerase chain reaction (PCR) was performed with universal 16S ribosomal primers because the 16S rRNA region does not exhibit a significant mutation rate (Janda and Abbott, 2007). Samples determined to have analogous 16S rRNA bands with PAO1 by gel electrophoresis were purified following the PCR purification kit protocol (Qiaquick) and sequenced. The sequences were then compared to the PAO1 16S rRNA sequence provided by the *Pseudomonas* Genome Database (Winsor et al., 2011). A culture of mucoid isolate M1 was grown in LB broth to an optical density of 0.5 to observe and quantify biofilm formation. One (1) mL of this sample was grown in capillary flow cell (Ibidi), fixed with paraformaldehyde, stained with LIVE/DEAD stain (Invitrogen), and imaged with confocal microscopy. For positive comparison, a mucoid strain of *P. aeruginosa* (PDO300) was grown under the same conditions. A *psl* dot blot, an alginate dot blot, and carbazole alginate assay were performed according to the methods outlined in Kintner and Van Buren (1982).

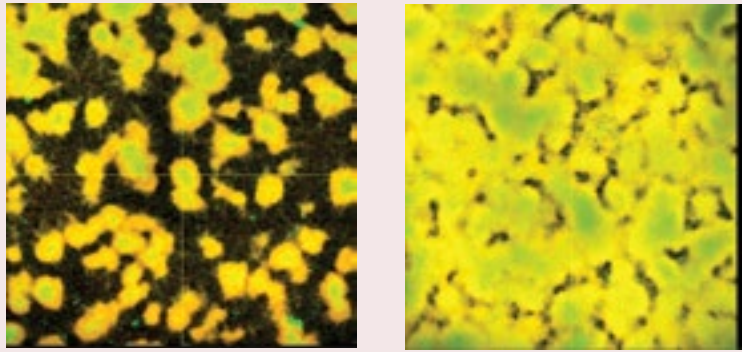


Figure 4. Biofilm growth of M1 (left) compared to growth of mucooid PDO300 (right). 20X magnification.

Results

Phenotypic Identification and Sequencing of Variants

Thirteen variants were selected from the 175 total samples and screened for more detailed analysis if they exhibited either a mucooid or rugose small colony variant phenotype. Phenotypic identification was determined by visual comparison to the mucooid morphology exhibited in Figure 2, as well as the mucooid clinical sputum isolate FRD1 (Figure 3) and RSCV isolate MJK8 (Figure 3). Sequencing results are only available for ten variants due to the inability to purify sufficient DNA. Isolates identified to be of a genus other than *Pseudomonas* are considered contaminants (Table 1). Though each wound was co-inoculated with *Pseudomonas aeruginosa* (PAO1) and *Acinetobacter baumannii* (strain 19606) with the goal of studying the mechanism of each pathogen, this paper focuses solely on *Pseudomonas* isolates. The presence of two strains is not expected to have affected the results of either isolate due to the lack of a sterilized environment during the course of infection and the variation in the nature of treatment of each wound. These conditions introduced contamination, a source of natural competition, and therefore eliminated potential competition between the two strains. The term “chronic” was assigned to the infection described above due to the following factors: an unsterilized environment, treatment of the wound site which ranged from no treatment to surgical debridement, and the length of time of infection, the longest being 35 days.

Biofilm Growth and Quantification

Once isolate M1 was determined to be PAO1-derived by 16S rRNA sequencing, several assays were performed to observe and quantify biofilm growth and composition. Figure 4 shows confocal imaging of biofilm growth in a flow reactor cell. The imaging demonstrates the ability of M1 to form tall, tightly packed microcolonies, while PDO300 demonstrates thicker, shorter microcolonies. In attempt to identify the composition of M1’s biofilm, both an alginate and a psl dot blot were performed (Figure 5). Both dot blots reveal that M1’s biofilm contains neither alginate nor psl, the common exopolysaccharides of *P. aeruginosa*. This lack of alginate was confirmed by an alginate assay (Graph 1).

Discussion

Previous studies have thoroughly investigated the *in vitro* differentiation of *P. aeruginosa* and characterized the potential molecular adaptations that promote this differentiation and subsequent survival in a host environment. Several sputum isolates from chronic respiratory infections of CF patients have also been studied in great detail. However, to our knowledge, no previous studies have developed a chronic infection model designed to represent the chronic inflammation that is believed to induce the molecular adaptation of wild-type *P. aeruginosa* (PAO1). This model allows the investigation of the progression

Table 1. Results of 16S rRNA sequencing indicate the presence of a PAO1 derived mucooid isolate and contaminant bacteria.

Isolate	Phenotype	Sequence Identification (genus)	Figure Identification
BF45-D35-T3A2	Mucooid	<i>Pseudomonas</i>	M1
BF45-D14-T2A1	Mucooid	<i>Enterococcus</i>	M2
BF20-D7-T1B3	RSCV	<i>Bacillus</i>	R1
BF44-D35-T3B1	RSCV	Insufficient	R2
BF45-D35-T3A2	RSCV	<i>Enterococcus</i>	R3
BF28-D7-C1A3	RSCV	<i>Bacillus</i>	R4
BF20-D7-T1A3	RSCV	Insufficient	R5
BF37-D56-T3B3	RSCV	<i>Micrococcus</i>	R6
BF14-D14-T2B	RSCV	Insufficient	R7
BF37-D56-T3B2	RSCV	<i>Kocuria</i>	R8

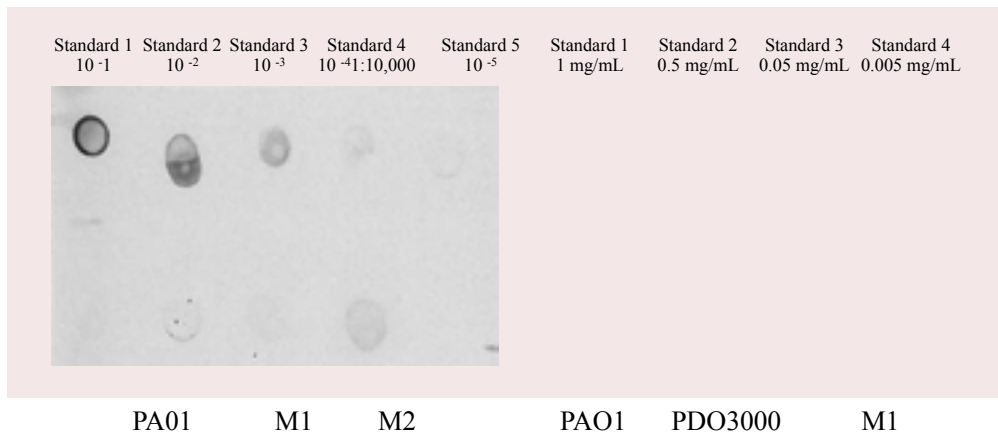
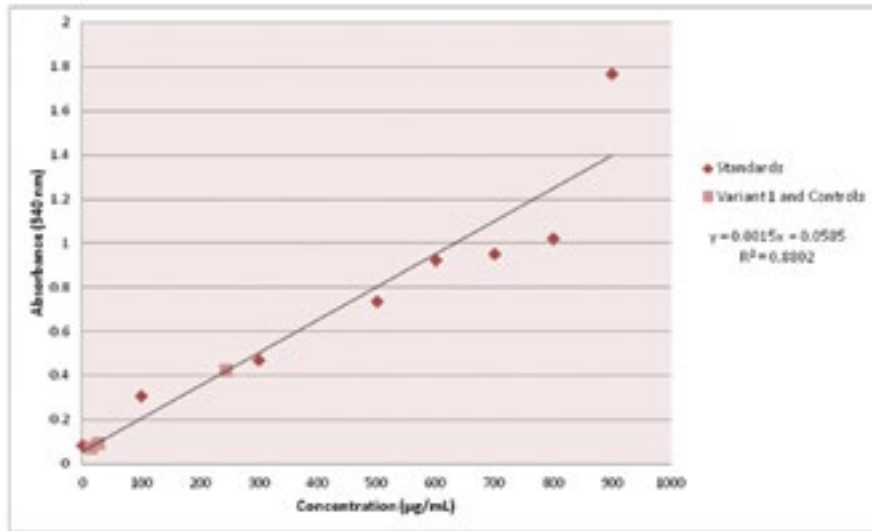


Figure 5. Alginate dot blot (left) and psl dot blot (right) indicate that the biofilm of M1 contains neither alginate, nor psl. Each label corresponds to the dot directly above or below it. Some dots may not be readily evident due to low concentrations.

of molecular adaption and formation of biofilms in response to chronic inflammation. In the screening of 175 samples, we discovered a wide variation in colony morphology that can be partially attributed to the presence of contaminant bacteria. More significantly, the amount of samples screened as well as the identification of characteristic *P. aeruginosa* isolates suggest that the morphology differences can also be attributed to the selection of *P. aeruginosa* variants that possess the ability to endure chronic *in vivo* infection. In particular, the identification of the mucoid isolate from experimental sample BF45-D35-T3B1 (earlier referred to as M1) as PAO1-derived confirms the results of previous studies that *P. aeruginosa* converts from non-mucoid PAO1 to a mucoid phenotype when subjected to chronic inflammation from the host's immune system (Mathee et al., 1999; Song et al., 2003). Interestingly, the sample M1 was isolated from an untreated wound with the longest time of infection used in this study (35 days), eliminating antibiotic or other routine wound care treatments as a means of inducing the change. We propose this bacterial response is due to a response to the immune factors of the host, not antimicrobial or surgical debridement therapy. The isolation of a mucoid morphology also parallels the isolation of the mucoid clinical CF sputum isolate FRD1, suggesting our model may be representative of the chronic infectious environment of a CF patient. Elucidation of the mechanisms underlying each of these morphological changes and comparison to previously determined adaptive mechanisms is an interesting aspect for future study, requiring whole genome sequencing for mutations in the alginate synthesis pathway and other important biosynthetic loci. When comparing the biofilm of the mucoid isolate M1 with a biofilm of the known mucoid strain PDO3000 a noticeable difference in the mode of growth was observed. The mucoid isolate demonstrated aggregation into distinct clusters of biofilm matrix, commonly referred to as "towers" or "mushrooms," while

the PDO3000 biofilm exhibited a thicker, more even growth. The formation of these densely packed microcolonies is attributed to the production of the polysaccharide psl, which has been deemed necessary for both mucoid and non-mucoid biofilm growth. Also, strains that produce a large amount of psl exhibit a densely packed biofilm (Mann and Wozniak, 2012; Ma et al., 2012). Based upon these previous conclusions, we expected that the biofilm of isolate M1 would be primarily composed of psl polysaccharide. However, the results of the psl dot blot disproved this assumption by indicating that no psl polysaccharide was present in the biofilm of M1. For this reason, an alginate dot blot and assay were performed to ascertain whether the biofilm was composed of alginate, the primary polysaccharide present in mucoid *P. aeruginosa* biofilms. Both of these methods yielded the result that alginate was not present in the biofilm of M1. The absence of psl and alginate polysaccharides may indicate a uniquely composed biofilm created by a chronic inflammatory environment. However, these preliminary results must be validated by replication or by increasing the selection of variants sequenced. Particularly, a full characterization of the M1 isolate including whole genome sequencing and determination of biofilm composition should be conducted. The variants identified through this project present several interesting avenues for future research, including complete characterization of an apparent mucoid PAO1-derived variant that was isolated from a chronic wound. This isolate could be used to identify new or confirm previously seen genotypic variations. Another future direction is to measure the response of the isolates to the inflammatory species present during *in vivo* chronic infection in order to observe the resulting changes in bacterial function. From these observations, the changes that occur preceding to phenotypic differentiation could be assessed and targeted in the development of therapeutics for treatment of chronic *P. aeruginosa* infections.



Graph 1. Quantification of alginate. Alginate assay confirms initial dot blot result that alginate is not present in the biofilm of M1.

References

- Baynham, P. J., A. L. Brown, L. L. Hall, and D. J. Wozniak. (1999). *Pseudomonas aeruginosa* AlgZ, a ribbon-helix-helix DNA-binding protein, is essential for alginate synthesis and algKD transcriptional activation. *Molecular Microbiology*: 33 (5), 1069-1080.
- Janda, M. J. and S. L. Abbott. (2007). 16S rRNA gene sequencing for bacterial identification in the diagnostic laboratory: pluses, perils, and pitfalls. *Journal of Clinical Microbiology*: 45 (9), 2761-2764.
- Kintner, P. K. and J. P. Van Buren, III. (1982). Carbohydrate interference and its correction in pectin analysis using the m-hydroxydiphenyl method. *Journal of Food Science*: 47 (3), 756-759.
- Ma, L., S. Wang, D. Wang, M. R. Parsek, and D. J. Wozniak. (2012). The roles of biofilm matrix polysaccharide psl in mucoid *Pseudomonas aeruginosa* biofilms. *Federation of European Microbiological Societies*: 65 (2), 377-380.
- Mann, E. E. and D. J. Wozniak. (2012). *Pseudomonas* biofilm matrix composition and niche biology. *Federation of European Microbiological Societies*: 36 (4), 893-916.
- Mathee, K., O. Ciofu, C. Sternberg, P. W. Lindum, J. I. A. Campbell, P. Jensen, A. H. Johnsen, M. Givskov, D. E. Ohman, M. Søren, N. Høiby, and A. Kharazmi. (1999). Mucoid conversion of *Pseudomonas aeruginosa* by hydrogen peroxide: a mechanism for virulence activation in the cystic fibrosis lung. *Microbiology*: 145 (6), 1349-1357.
- Moody, C. S. and H. M. Hassan. (1982). Mutagenicity of oxygen free radicals. *Proceedings of the National Academy of Sciences*: 79 (9), 2855-2859.
- Ramsey, D. M. and D. J. Wozniak. (2005). Understanding the control of *Pseudomonas aeruginosa* alginate synthesis and the prospects for management of chronic infections in cystic fibrosis. *Molecular Microbiology*: 56 (2), 309-322.
- Song, Z., H. Wu, O. Ciofu, K.F. Kong, N. Høiby, J. Rygaard, A. Kharazmi, and K. Mathee. (2003). *Pseudomonas aeruginosa* alginate is refractory to Th1 immune response and impedes host immune clearance in a mouse model of acute lung infection. *Journal of Medical Microbiology*: 52 (9), 731-740.
- Starkey, M., J. H. Hickman, L. Ma, N. Zhang, S. De Long, A. Hinz, S. Palacio, C. Manoil, M. J. Kirisits, T. D. Starner, D. J. Wozniak, C. S. Harwood, and M. R. Parsek. (2009). *Pseudomonas aeruginosa* rugose small-colony variants have adaptations that likely promote persistence in the cystic fibrosis lung. *Journal of Bacteriology*: 191 (11), 3492-3503.
- Winsor, G. L., D. K. Lam, L. Fleming, R. Lo, M. D. Whiteside, N. Y. Yu, R. E. Hancock, and F. S. Brinkman. (2011). *Pseudomonas* Genome Database: improved comparative analysis and population genomics capability for *Pseudomonas* genomes. *Nucleic Acids Research*: 39: D596-600.

Acknowledgments

The authors would like to thank Dr. Peter Panizzi for acting as a faculty sponsor of this research.

Comparison of Articular Cartilage Thickness in Cadaveric Equine Limbs

W. Grant Kirkland, Ryan N. Whitmore, Hannah E. Young, Ashton J. Richardson, Robert L. Jackson, R. Reid Hanson

Abstract

Articular cartilage plays a pivotal role in the mechanical function of a joint. Understanding the unique abilities and mechanical properties of articular cartilage is important in preventing, diagnosing, and treating damage. It is believed that variation of cartilage thickness strongly influences the overall function of the joint. Therefore, this study explores how articular cartilage thickness correlates with types of equine joints and the articular surfaces within the joints. The average thickness of three different equine joints which undergo a variety of loads and ranges of motion was determined via a Bruker CETR machine. Seven articular surfaces were tested: (1) medial and (2) lateral condyles of the distal third metacarpus in the fetlock joint; (3) medial aspects of the distal radius and (4) proximal radial carpal bone of the radiocarpal joint; (5) distal radial carpal bone and (6) proximal third carpal bone of the midcarpal joint; and (7) medial femoral condyle of the stifle joint. Results indicate that the mean articular cartilage thickness of the stifle joint was significantly greater than both the carpus and fetlock joints in all six horses analyzed ($p < 0.05$). There was a difference ($p = 0.35$) in the cartilage thickness of the carpus compared to the fetlock joint. Within the carpus, the radiocarpal joint cartilage thickness was found to be significantly greater than that of the intercarpal joint ($p < 0.05$). However, in the fetlock joint there was no significant difference between the thickness of articular cartilage of the medial and lateral condyles of the distal cannon bone.

Introduction

Articular cartilage is the smooth, white fibrous load bearing connective tissue that covers the ends of bones, known as the articular surface.

Articular cartilage is classified as a porous, viscoelastic material composed of solid and liquid phases; the solid phase is elastic and acts as a porous membrane that allows the fluid to flow through the cartilage. This model of cartilage is known as the biphasic model (Lu and Mow, 2008). The articular surfaces come together to form a synovial joint, which is the most common and most movable joint in a mammal. Articular cartilage plays a pivotal role in the mechanical function of a joint. Healthy articular cartilage reduces the force required to create movement between articular surfaces, provides the articular surfaces with protection from damage, and reduces pressure on the articular surfaces by redistributing impulse due to weight-bearing activities such as running or jumping. How different mechanical properties of articular cartilage contribute to its unique abilities is extremely important in preventing, diagnosing, and treating damage to articular cartilage.

This study focuses on three equine joints: the stifle joint, the carpus joint, and the fetlock joint (Figure 1). The stifle joint is located in the hind legs of the equine, whereas the fetlock and carpus joints are located in the front legs. As a result, the carpus and fetlock joints support similar loads and impacts, as they are located axially in relation to one another. The static weight bearing loads of the fetlock, equivalent to that of a human wrist, and carpus joints are greater than that of the stifle joint due to the body weight distribution of an equine. The hind limbs, and therefore stifle joint, act as the primary means of propelling the horse forward.

Cartilage thickness is believed to be a major contributing factor to the longevity and mechanical performance of a joint, as the articular cartilage is the primary means for distributing contact stresses within the joint. Studies suggest that articular cartilage thickness in regions with cartilage-to-cartilage



Figure 1. Location of three equine joints tested in this study. Thickness of articular cartilage in these joints is believed to significantly influence functionality.



Figure 2. Tested equine joint surfaces. (A) Fetlock joint: (1) medial aspect, (2) lateral aspect of distal surface of the cannon bone; (B) Carpal joint: (3) distal radius and (4) proximal radial carpal bone of radiocarpal joint, (5) distal radial carpal bone of midcarpal joint and (6) proximal third carpal bone of midcarpal joint; (C) Stifle joint: (7) medial femoral condyle.

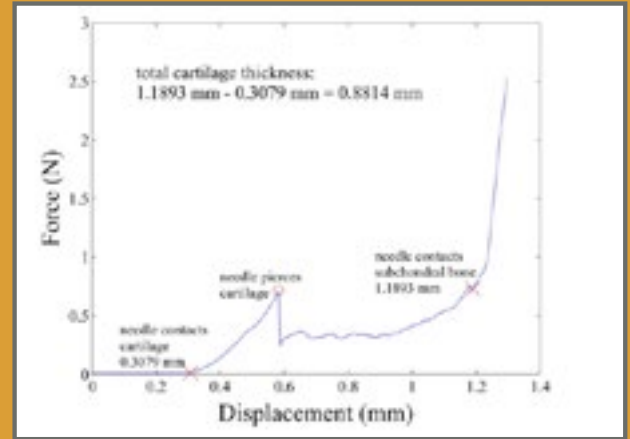


Figure 3. A sample plot used to determine cartilage thickness. The first X represents the initial needle contact with cartilage. The second X represents the initial needle contact with the cartilage-bone interface, and the O represents the point at which the needle pierces the cartilage.

Table 1. The average articular cartilage thickness, in millimeters, of each surface tested. Numbers correspond to surfaces tested (see Figure 2).

Joint	Fetlock		Carpus			Stifle	
Surface	Medial (1)	Lateral (2)	Distal Radius (3)	Proximal Radial Carpal Bone (4)	Distal Radial Carpal Bone (5)	Proximal 3rd Carpal Bone (6)	Medial Femoral Condyle (7)
Thickness	0.833	0.852	0.883	0.914	0.729	0.599	2.026

contact is greater than the thickness of cartilage in non-contact regions. It is believed that this increased cartilage thickness reduces contact stresses and friction within the area of contact (Li et al., 2005). Since different joints undergo different loads and motions, our hypothesis is that articular cartilage thickness varies for different equine limb joints.

Methodology

JOINT HARVESTING

A total of twelve sets of left equine limb joints were obtained from equine cadavers acquired by the Alabama State Diagnostic Lab. Following necropsy, gross dissection of the joints specific to our research and in healthy condition was performed. All fetlock joints were removed at mid-cannon bone

and mid-pastern bone; carpus joints were removed at mid-radius and mid-cannon bone; stifle joints were condensed to distal femur and proximal tibia. Fine dissection was then performed to disarticulate the articular cartilage surfaces of interest within the joint. Excess tissue was removed from each joint and surfaces were cut to an appropriate sample size using a band saw. Within the fetlock joint, the entire distal articular surface of the cannon bone was collected and divided into (1) medial and (2) lateral aspects. Only the medial aspects of the radiocarpal and midcarpal joints within the carpus were tested. The surfaces of interest were the (3) distal radius and (4) proximal radial carpal bone of the radiocarpal joint and the (5) distal radial carpal bone and (6) proximal third carpal bone of the midcarpal joint.

The articular surface of interest within the stifle joint was the (7) medial femoral condyle located in the femorotibial joint. These surfaces are shown in Figure 2.

NEEDLE PROBE TESTING

The needle probe tests were performed on a Bruker CETR UMT-3 tribometer via a high sensitivity load cell within a maximum of 46 hours postmortem with average tests performed within 13 hours postmortem. A 25-gauge hypodermic needle was mounted vertically below the load cell. A 25-gauge needle was chosen because it is stiff enough not to deflect during the test but thin enough to easily penetrate the cartilage surface. Saline was added to the dissected cartilage samples in a flat-bottomed acrylic container until the entire sample was submerged. The sample and container were then placed just beneath the hypodermic needle and load cell in the CETR machine.

A custom testing sequence was created and was performed five times on each sample. The sequence displaced the needle vertically downward at a rate of 0.02 mm per second until the load cell registered a force greater than or equal to 2.5 N. A force of 2.5 N was chosen based on repeated observations of the force output when the needle contacted the articular bone. A sampling rate of 1000 Hz was used, gathering 1000 data points per second. Each of the five tests was performed in a linear progression across the load bearing surface of each sample with 3 to 5 mm separating adjacent testing locations.

The force data and the vertical displacement data from each test was then output into a CSV file. A Savitzky-Golay smoothing filter was applied to the data in Matlab™. The Savitzky-Golay method was chosen instead of a moving weighted average filter because it tends to preserve features of the distribution, such as relative maxima and minima, an important aspect to this type of data analysis.

The data was normalized so that the initial needle force just before contact was zeroed. The vertical displacement position at which the load cell detected an increase in force was determined to be the surface of the articular cartilage. This point of surface contact was indicated by an increase in slope calculated over vertical displacements of 0.02 μm , 0.2 μm , 0.4 μm , 2.0 μm , and 5.0 μm . Using visual

inspection, a slope ranging from 0.4 N/ μm to 1.4 N/ μm was observed to coincide with the point of surface contact, with between 0.5 N/ μm or 0.7 N/ μm coinciding the majority of the time. Therefore, a slope value of 0.5 N/ μm was used in the program to automatically detect when the needle contacted the cartilage surface. The contact point corresponded to an average threshold force of 0.0321 N.

A sudden decrease in detected force was determined to be the vertical displacement position at which the needle pierced the surface of the cartilage. This data point was marked by determining the maximum value and corresponding index on a range from the first data point to the minimum value and index of the numerically differentiated data. A sudden increase in detected force was determined to be the vertical displacement position at which the needle contacted the subchondral bone.

Similar to the method of determining the point of surface contact, a slope value greater than 3.0 N/ μm calculated over vertical displacements of 0.02 μm , 0.2 μm , 0.4 μm , 2.0 μm , and 5.0 μm was used to numerically determine the point of subchondral bone contact.

A thorough visual inspection of each plot was performed to insure the numerically chosen data points were consistent. Threshold slope values were adjusted only when required. To determine the thickness of the cartilage, the displacement position of the subchondral bone contact was subtracted from the displacement position of the initial cartilage surface contact, as shown in Figure 3.

Results

The average thickness of each joint surface was calculated, as shown in Table 1. Results show the medial and lateral surfaces within the fetlock joint are very similar ($p = 0.71$), implying no statistical difference between articular cartilage thickness of the medial and lateral surfaces of the fetlock.

Data collected from the four surfaces within the carpus joint was statistically analyzed using a mixed model for analysis of variance and Scheffe's test for multiple comparisons, as shown in Table 2. Results indicate the articular cartilage thickness of the proximal third carpal bone surface was statistically different from

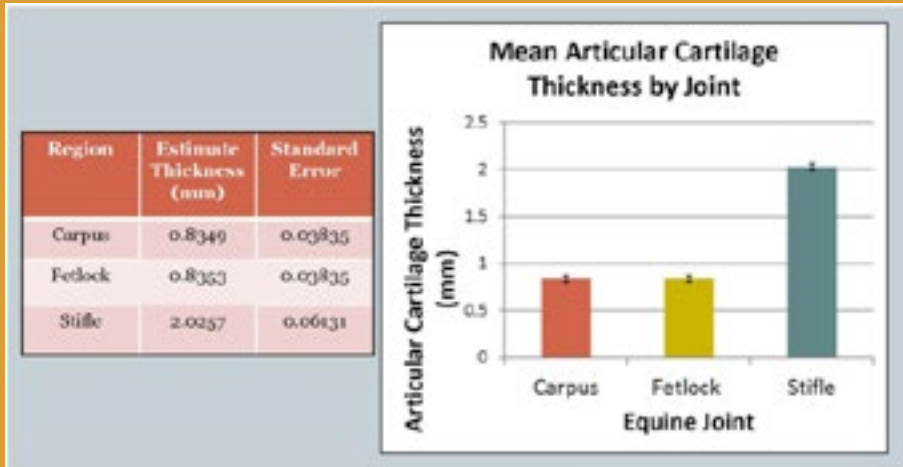


Figure 4. Mean articular cartilage thickness by joint. Although the carpus and fetlock joints had similar thickness, the thickness of the stifle joint was significantly greater.

Table 2. Statistical significance of cartilage thickness data.

Region	Compared to Region	P Value	Conclusion
Distal Radius (3)	Proximal Radial Carpal Bone (4)	0.9716	Not Statistically Different
Distal Radius (3)	Distal Radial Carpal Bone (5)	0.1280	Not Statistically Different
Distal Radius (3)	Proximal Third Carpal Bone (6)	0.0013	Statistically Different
Proximal Radial Carpal Bone (4)	Distal Radial Carpal Bone (5)	0.0452	Statistically Different
Proximal Radial Carpal Bone (4)	Proximal Third Carpal Bone (6)	0.0002	Statistically Different
Distal Radial Carpal Bone (5)	Proximal Third Carpal Bone (6)	0.3237	Not Statistically Different

the distal radius ($p = 0.0013$) and proximal radial carpal bone ($p = 0.0002$) surfaces. Also, the articular cartilage thickness of the proximal radial carpal bone surface was statistically different from the distal radial carpal bone surface ($p = 0.0452$). The articular cartilage thicknesses of all other carpal surfaces were statistically equivalent.

Figure 4 shows the overall average articular cartilage thickness calculated for each of the three joints using all of the data collected from each joint. Results indicate the stifle had significantly thicker articular cartilage than both the carpus and the fetlock.

The thickness of articular cartilage in the carpus and fetlock joints are statistically equivalent ($p < 0.001$), while the thickness of articular cartilage in the stifle compared to the carpus and fetlock is statistically different ($p = 1.00$).

Discussion

The results presented verify the hypothesis that articular cartilage thickness varies between different equine limb joints. Even though the overall average thicknesses of the carpus and fetlock joints did not prove to be significantly different from one another, they did prove to be significantly different from the thickness of the stifle joint. The correlation between cartilage thickness and loading capacity has been a topic of great discussion (Li et al., 2005). Ateshian et al. (1991) hypothesized that areas of thicker cartilage correspond to joint surfaces which support a greater load. In contrast, Eckstein et al. (2002) have suggested that an increase in cartilage thickness has an adverse effect on the ability to transmit loads due to the biphasic properties that characterizes cartilage. Although it was suggested that articular cartilage thickness is related to loading in a directly proportional manner, in that a joint

supporting a greater load requires thicker cartilage, our results do not support this hypothesis. In addition, because the surface area of the stifle is much larger than that of the fetlock and carpus, it should experience a significantly lower pressure.

Since the contact area of the individual joints is required in order to determine the precise pressures experienced in each joint, it is suggested that further studies focus on the relationship between contact area and pressure distribution changes during loading in the stifle joint. These results would allow a comparison of articular cartilage thickness related to contact area and pressure to be determined and enable loading and articular cartilage thickness to be compared (Li et al., 2005). Previous studies of this relationship exist for the third carpal bone. The results indicate an increase in contact area with an increase in load, as well as an increase in the mean pressure for certain area of the joint (Palmer et al., 1994). Likewise, these results demonstrate that the mechanics of the stifle joint in particular may be more complex than simple relationships based on joint size and amount of load supported by the joint.

Another possible explanation relating to articular cartilage thickness, contact area, and pressure distribution pertains to the type of joint. The radiocarpal joint is a hinge joint with ball and socket movement, whereas the midcarpal is a door hinge type joint. Also, proximity to the body may play a role in pressure distribution which may affect cartilage thickness, as the stifle is the most proximal joint and also maintains the highest mean cartilage thickness. Therefore, this study cannot come to a conclusion based on cartilage thickness and total load carried in the joint based on our results.

Conclusion

This study showed significant differences in the thickness of the articular cartilage between the carpus and the stifle joints, as well as between the fetlock and the stifle joints. The carpus and fetlock joints were not found to have statistically different articular cartilage thicknesses. Within the fetlock joint, the thicknesses of the articular cartilage of the medial and lateral aspects

were not found to be statistically different. Within the carpus joint, the thickness of the articular cartilage of the proximal third carpal bone was statistically different from the distal radius and proximal radial carpal bone. Also, the thickness of the articular cartilage of the proximal radial carpal bone surface was statistically different than that of the distal radial carpal bone surface. This study is inconclusive with regards to the relation between cartilage thickness and the load-bearing capacity of the joints. Further work is required to explore the complexities of this topic.

REFERENCES

- Ateshian, G. A., L. J. Soslowsky, and V. C. Mow. (1991). Quantitation of articular surface topography and cartilage thickness in knee joints using stereophotogrammetry. *Journal of Biomechanics*: 24 (8), 761-776.
- Eckstein, F., S. Faber, R. Muhlbauer, J. Hohe, K. H. Englmeier, M. Reiser, and R. Putz. (2002). Functional adaptation of human joints to mechanical stimuli. *Osteoarthritis Cartilage*: 10 (1), 44-50.
- Li, G., S. E. Park, L. E. DeFrate, M. E. Schutzer, L. Ji, T.J. Gill, and H. E. Rubash. (2005). The cartilage thickness distribution in the tibiofemoral joint and its correlation with cartilage-to- cartilage contact. *Clinical Biomechanics*: 20 (7), 736-744.
- Lu, X. L., and V. C. Mow. (2008). Structure biomechanics of articular cartilage and determination of material properties. *Medicine and Science in Sports and Exercise*: 40 (2), 193-199.
- Palmer, J. L., A. L. Bertone, and A. S. Litsky. (1994). Contact area and pressure distribution changes of the equine third carpal bone during loading. *Equine Veterinary Journal*: 26 (3), 197-202.

Acknowledgments

The authors acknowledge contributions from J. C. Wright, K. M. Theis, C. A. Malpass, H. Lee (Auburn University), and P. A. Smyth (Georgia Institute of Technology). We also thank the AU Intramural Grant Program and the Undergraduate Research Program for support of R. Whitmore.

Microwave Effects Relevant to Antimatter Traps

Kelsie A. Niffenegger, Patrick H. Donnan, Francis Robicheaux

Abstract

We investigate the effect of microwaves on hydrogenic Rydberg atoms in strong magnetic fields in order to determine if microwave ionization will be present in the current generation of antihydrogen traps. We examine what microwave electric field magnitudes and microwave frequencies are required to ionize the atoms in strong magnetic fields. We compare results for a ramping, non-oscillating electric field in the presence of microwaves to calculations that do not include microwaves from reference (Donnan et al., 2011). We present classical calculations for an initial quantum bound state of $n = 40$ and several magnetic field strengths for comparison. Lastly, we examine the effect of a weak microwave field on recombination in an ultracold neutral plasma, which mimics the three-body recombination (3BR) that occurs in antihydrogen traps. We show that weak microwave fields generated with sufficiently low power should have no effect on the ionization of Rydberg antiatoms or on recombination in an ultracold plasma.

Introduction

Microwave ionization of Rydberg atoms is a well-studied phenomenon in the field of atomic physics. Fu et al. (1990), Griffiths and Farrelly (1992) and Kappertz and Nauenberg (1993) provide a very small number of examples of this phenomenon in their research. In studying antimatter, physicists seek to minimize the amount of ionization; ionizing any potentially trapped antihydrogen atoms leads to fewer trapped antihydrogen atoms in each experimental shot. Microwaves are used as a tool to study antimatter because one of the easiest precision measurements to perform on trapped antihydrogen is hyperfine spectroscopy. Hyperfine spectroscopy, where the positron flips its spin, requires microwaves

to drive the transition between the two hyperfine states. Hyperfine spectroscopy is currently the only spectroscopic measurement that has been performed on antihydrogen (Amole et al., 2012). Strong magnetic fields are present in every apparatus of the current generation of antihydrogen trapping experiments, and strong electric fields are used to control antimatter plasmas in some traps. (Anderson et al., 2011; Enemoto et al., 2010 and Gabrielse, 2010). Thus, this investigation is aimed at understanding how these magnetic and electric fields influence the microwave ionization process. We aim to discover if microwave ionization will affect current antimatter experiments.

Numerical Methods

We present calculations for microwave electric fields large enough to ionize Rydberg hydrogen atoms in the presence of the strong magnetic fields present in the traps. Donnan et al. (2011) showed that strong magnetic fields can significantly influence the field strength required to ionize the atoms. We investigate the ionization dynamics with strong microwave fields to examine any possible resonance conditions. By introducing a ramping, non-oscillatory electric field, we simulate the effect of the electrodes that are being used to guide positron and antiproton plasmas in an antimatter trap (Anderson et al., 2011). We reduce the microwave electric field strength to an experimentally feasible value, i.e., 0.46 V cm^{-1} , and examine the effect of a weak microwave field on ionization. Lastly, we examine the effect of weak microwaves on recombination in an ultracold plasma. Ultracold plasmas have recently become a topic of great interest in atomic physics (Rolston, 2008). We believe the recombination in an ultracold plasma is analogous to

the three-body recombination (3BR) process by which it is believed antihydrogen is formed, where two positrons collide within the field of an antiproton leaving one bound to the antiproton and one with more energy (Butler, 2011). The atomic system used in this paper is an electron orbiting a proton. Assuming no charge-parity-time (CPT) violations, the calculations are accurate for antihydrogen as well. All calculations are for an initial quantum bound state of $n = 40$.

We use several approximations to model the case of microwave ionization. Firstly, we take the nucleus to be infinitely massive and fixed in space at the origin of our coordinate system. This is a good approximation because the antiatoms contained in the traps move fairly slowly (on the order of 100 m s^{-1}) which means that the time scale of the electron's motion is much shorter than that of the nucleus. We use the following form to model the electric field term from the microwave

$$E_{mw}(t) = E_0 \cos(-\omega t) \quad (1)$$

where $E_{mw}(t)$ is the time-dependent microwave strength, E_0 is the electric field maximum, ω is the angular frequency of the microwave and t is the time in the simulation. Here we have neglected the spatial term usually found in an equation describing an electromagnetic wave. We make this approximation because the spatial term is multiplied by a factor of the wavenumber which is $1/c$ smaller than the angular frequency for an electromagnetic wave. Using the same reasoning, we neglect the microwave magnetic field term, as it is $1/c$ smaller than the electric field term and will not contribute significantly to the motion.

We choose to introduce the microwaves along the z-axis, such that

$$\vec{E}_{mw} = E_{mw} \hat{z} \quad (2)$$

We choose a simple directionality for the application scheme in order to represent an experimentally feasible set-up in our calculations.

We use the same method as the electric fields modeled by Donnan et al. (2011). This method gives an electric field term of

$$E_{ramp}(t) = t_{wid} \left(\frac{E_{max}}{t_{final}} \right) \ln(1 + e^{t/t_{wid}}) \quad (3)$$

Here t_{wid} is taken to be 0.5% of the total run time, t_{final} is the value of the electric field at t_{final} . The reader should note that E_{max} and E_0 are not the same. We give the electric field this form in order to ensure a smooth turn-on around the point $t = 0$ and linear behavior when t is larger than . Calculations begin at negative time to ensure a smooth turn-on of the electric field, typically between -2 and -5 nanoseconds before $t = 0$. We again choose the directionality of the field to be parallel to the z-axis.

We choose a magnetic field of varying strength depending on the calculation being run. The magnetic field is also parallel to the z-axis, giving the following equations of motion

$$\frac{d\vec{r}}{dt} = \vec{v} \quad (4a)$$

$$\frac{d\vec{v}}{dt} = \frac{e(\vec{E}_{mw}(t) + \vec{E}_{ramp}(t) + \vec{v} \times B)}{m_e} \quad (4b)$$

where \vec{r} is the position of the electron, \vec{v} is the velocity of the electron, e is the charge of the electron, m_e is the mass of the electron, and \vec{B} is the magnetic field, $E_{ramp}(t)$ is not present in the calculations without the non-oscillating electric field.

We solve the equations of motion using a fourth-order, adaptive step-size Runge-Kutta algorithm (Press et al., 1992). This method is not symplectic so care must be taken to combat numerical drag. To minimize this effect, in each run we carefully observe conserved quantities for the systems being simulated. Unfortunately, when changing electric fields are present, typical momentum quantities are not conserved. For our configuration of electric and magnetic fields only the canonical angular momentum about the z-axis is conserved. If we observe a

significant change in the conserved quantity (on the order of a 1% change over the course of the simulation), we reject the data. Less than 0.5% of all runs were rejected.

To best simulate the starting state of the electron bound to a proton through 3BR, we use a microcanonical ensemble for the starting phase space coordinates of the electron in each trajectory. A microcanonical ensemble gives a spread of angular momentum for a fixed energy. This is a good approximation because it is nearly impossible to determine the exact starting conditions of the antihydrogen formed in the various traps due to n - l mixing by the electric fields present in the traps. This also allows us to pick a starting principal quantum bound state (which fixes the energy) for each set of trajectories, which makes the results easier to interpret. As previously mentioned, we use principal quantum number $n = 40$ in our simulations.

The ultracold plasma simulations are of a different nature than the previously discussed simulations. The previous simulations deal with only one moving body, but the ultracold plasma codes are many-body simulations. Other simulations with the same codes found convergence using 100 electrons and 100 ions (Niffenegger et al., 2011), so we adapt that same number of particles for this simulation.

Ion and electron motion in the plasma is simulated using the fourth-order, adaptive step-size Runge-Kutta algorithm and similar accuracy checks are performed. We ensure that the energy drift per particle is less than 0.01 K for every run. In no run is this condition met or exceeded. We use a soft-core model for the potential to decrease the computing time needed to run the simulation without changing the physical results (Niffenegger et al., 2011). Because the simulations are of a finite number of particles, we use a box with wrapping boundary conditions such that when a particle exits one side of the box, that particle reappears on the opposite side of the box. For the starting conditions of the ions and electrons, we randomly place ions in the box and start the electrons within roughly 20 Bohr radii of the ions with a radial velocity away from the near ion. The near ion is given the opposite momentum of the electron to conserve momentum. We use a velocity value of the electron that simulates that of a photoionized electron in a typical ultracold plasma experiment. This ensures that the energy of the atom equals that of the vacuum threshold of the ion-electron system of photoabsorption.

Results

Figures 1 through 3 present calculations of the ionization rates with only microwaves and the magnetic field. Though our simulations covered a range of microwave frequencies from 18 GHz to 60 GHz, we present only data for the microwave frequencies that gave the highest ionization rates. There is resonance-like behavior located at ~ 41 GHz (40 GHz and 42 GHz give the greatest ionization rates). This is a somewhat unanticipated value because the Larmor angular frequency for an electron in a 0.25 T magnetic field is ~ 44 GHz. It is unknown why the greatest ionization occurs at this frequency. Figure 1 presents decay curves for atoms in a 0.25 T magnetic field for a microwave field strength of 50 V cm^{-1} . Figures 2 and 3 present similar calculations for different magnetic field strengths. The scaling of the greatest ionization frequency does not follow that of the Larmor angular frequency of an electron in a magnetic field, as seen in Figures 2 and 3.

Figure 4 presents results with the ramping, non-oscillatory field added to the equations of motion. We chose to simulate 40 and 42 GHz for the microwave field due to results discussed in the previous section. We did not see any qualitative or quantitative difference between the 40 and 42 GHz cases. We reduced the microwave electric field strength to 10 V cm^{-1} . We chose 1000 V cm^{-1} for the ramping field strength (see Figure 6 of Donnan et al. (2011) for comparison). The 60 ns ramp does not quite have twice the length of the 30 ns ramp, indicative of microwaves contributing to the ionization for the given values. Figure 4 presents these decay curves.

For experimental reasons (ALPHA Collaboration, personal communication, 2012) having to do with the amount of power that can be effectively run through a microwave horn, we present simulations with and without microwave electric field strengths of 0.46 V cm^{-1} (Figure 5). We used a ramp time of 2400 ns. At these microwave electric field strengths, two orders of magnitude below previous simulations, we see the effect of the microwaves vanish.

Lastly, we performed simulations of an ultracold plasma with and without the microwave field strength of 0.46 V cm^{-1} that was given to us by the experimentalists (ALPHA Collaboration, personal communication, 2012). We found no difference with respect to the number of recombined atoms, meaning that microwaves should play no effect on the 3BR that forms the antihydrogen.

Conclusion

We have shown the effects that microwaves can have in the high magnetic fields present in current antimatter traps. We have shown that at experimentally feasible parameters, microwaves should not cause further ionization of Rydberg antihydrogen. By running at microwave powers low enough not to ionize the trapped antihydrogen as it decays to the ground state but still high enough to induce quantum transitions between ground hyperfine states, microwaves should continue to prove a useful tool for the analysis of the first element on the anti-periodic table.

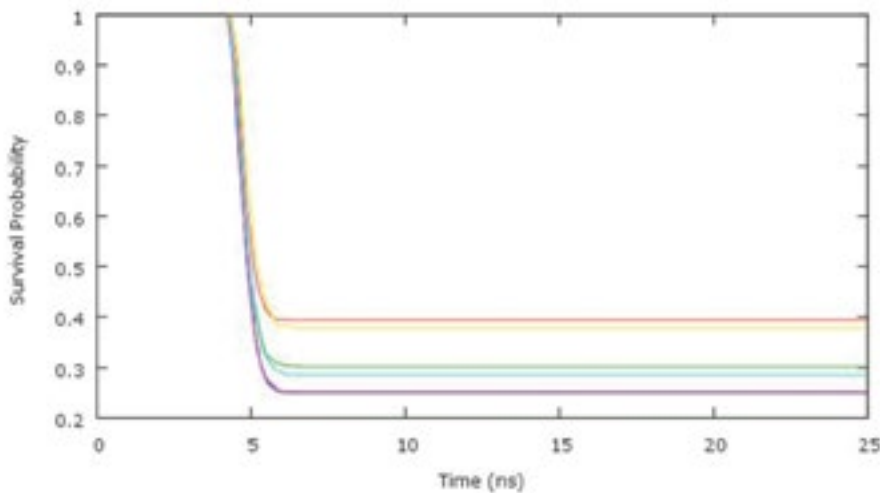


Figure 1. Decay curves for a 0.25 T magnetic field and a microwave electric field strength of 50 V cm^{-1} . The curves correspond to microwave frequencies as follows: red-36 GHz, green-38 GHz, blue-40 GHz, magenta-42 GHz, light blue-44 GHz and yellow-46 GHz. The maximum ionization occurs at ~ 41 GHz.

Figure 2. Decay curves for a 0.5 T magnetic field and a microwave electric field strength of 50 V cm^{-1} . The curves correspond to microwave frequencies as follows: red-36 GHz, green-38 GHz, blue-40 GHz, magenta-42 GHz, light blue-44 GHz and yellow-46 GHz. The maximum ionization occurs at ~ 42 GHz.

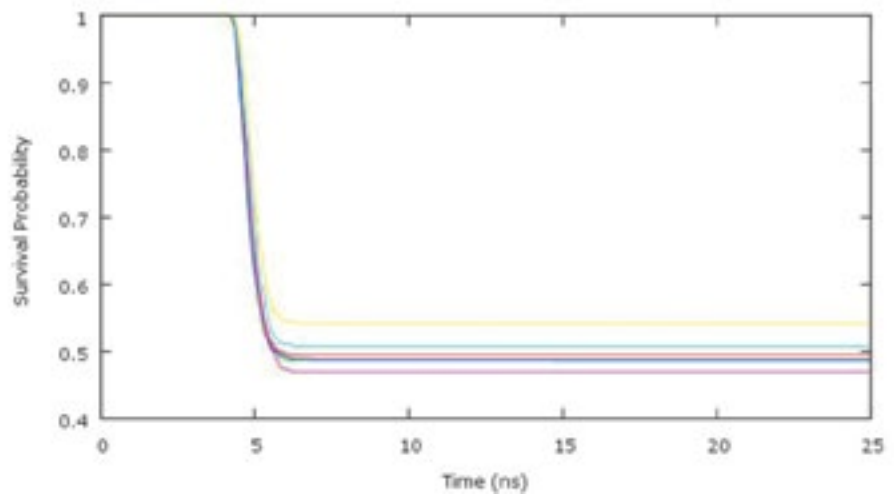


Figure 3. Decay curves for a 1 T magnetic field and a microwave electric field strength of 50 V cm^{-1} . The curves correspond to microwave frequencies as follows: red-36 GHz, green-38 GHz, blue-40 GHz, magenta-42 GHz, light blue-44 GHz and yellow-46 GHz. The maximum ionization occurs at $\sim 44 \text{ GHz}$.

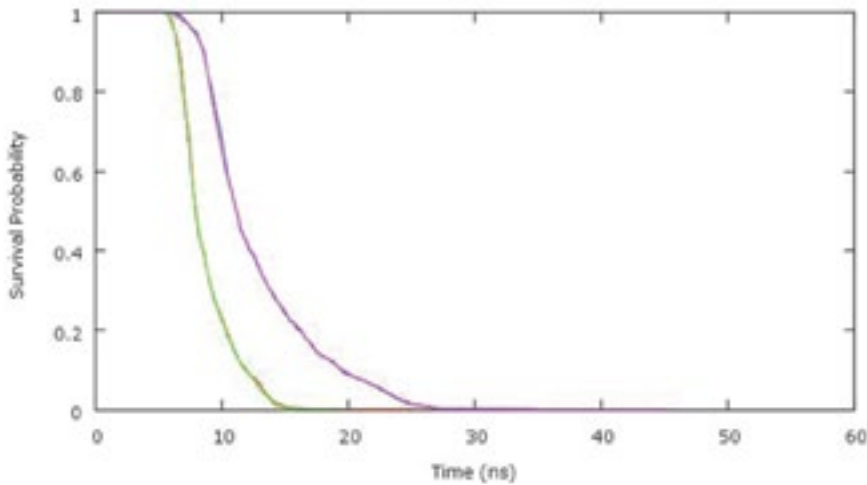
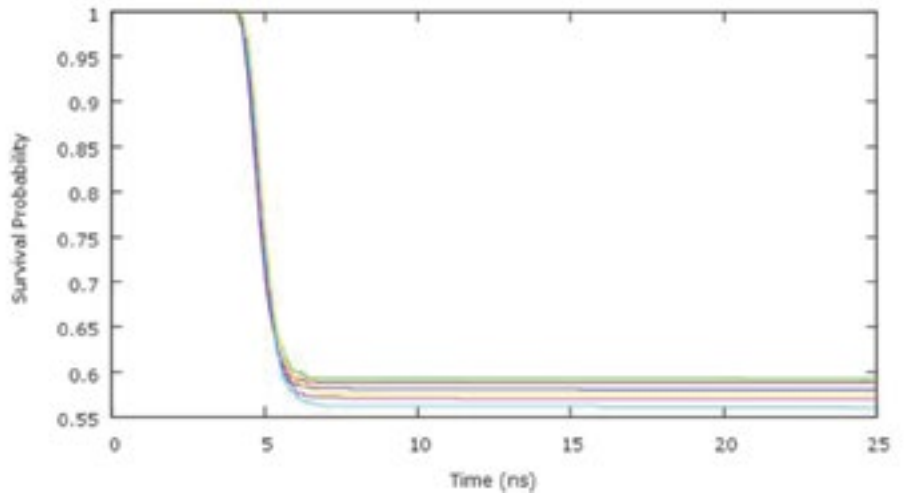
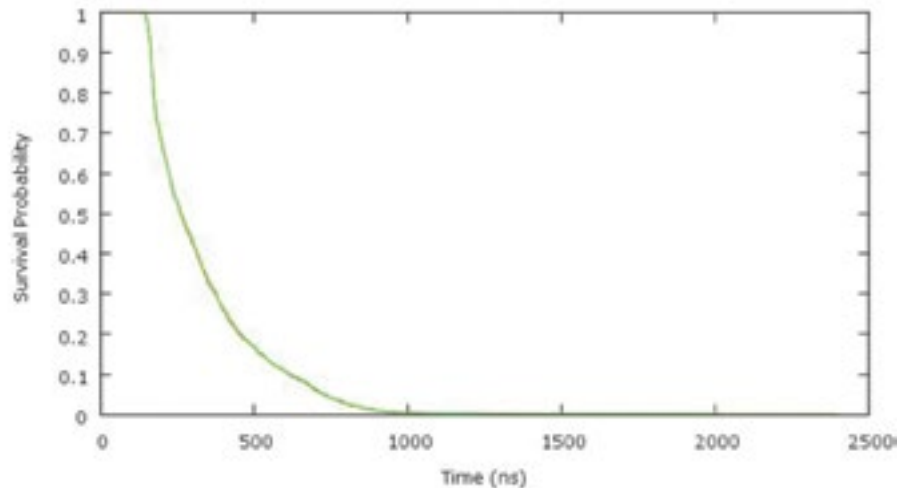


Figure 4. Decay curves with the addition of a non-oscillatory, ramping electric field in a microwave electric field of 10 V cm^{-1} . The ramping electric field ramped from near-zero (as discussed in the text) to 1000 V cm^{-1} over the prescribed time. The curves correspond as follows: red-40 GHz, 30 ns ramp time; green-42GHz, 30 ns ramp time; blue-40 GHz, 60 ns ramp time; and magenta-42 GHz 60 ns ramp time. Because there is no qualitative or quantitative difference between the two microwave frequencies, the green and red curves overlie one another, as do the blue and magenta curves.

Figure 5. Decay curves for a 2400 ns ramp time and microwave strength of 0.46 V cm^{-1} (red) and 0 V cm^{-1} (green). These parameters were chosen for experimental reasons. The effect of the microwaves is shown to be negligible in that the two curves overlie one another.



References

- Amole, C., and ALPHA Collaboration. (2012). Resonant quantum transitions in trapped antihydrogen atoms. *Nature*: 483 (7390), 439-444.
- Andresen, G. B., and ALPHA Collaboration. (2011). Confinement of antihydrogen for 1,000 seconds. *Nature Physics*: 7 (7), 558-564.
- Bulter, E. (2011). Antihydrogen Formation, Dynamics and Trapping. Ph.D. Thesis. Department of Physics, Swansea, Wales, United Kingdom: Swansea University.
- Donnan, P. H. and F. Robicheaux. (2012). Simulations of Hyperfine Antihydrogen Spectroscopy of Antihydrogen Contained by the ALPHA Collaboration Trap. *Auburn University Journal of Undergraduate Scholarship*: 1, 12-19.
- Donnan, P. H., K. Niffenegger, T. Topcu and F. Robicheaux. (2011). Calculation of state selective field ionization of hydrogen atoms in a strong magnetic field. *Journal of Physics B: Atomic, Molecular and Optical Physics*: 44 (18), 184003.
- Enemoto, Y., and ASACUSA Collaboration. (2010). Synthesis of Cold Antihydrogen in a Cusp Trap. *Physical Review Letters*: 105 (24), 243401.
- Fu, P., T. J. Scholz, J. M. Hetteema and T. F. Gallagher. (1990). Ionization of Rydberg atoms by a circularly polarized microwave field. *Physical Review Letters*: 64 (5), 511-514.
- Gabrielse, G. (2010). Slow Antihydrogen. *Physics Today*: 63 (3), 68-69.
- Griffiths, J. A. and D. Farrelly. (1992). Ionization of Rydberg atoms by circularly and elliptically polarized microwave fields. *Physical Review A*: 45 (5), R2678-R2681.
- Kappertz, P. and M. Nauenberg. (1993). Circularly polarized microwave ionization of hydrogen. *Physical Review A*: 47 (6), 4749-4755.
- Niffenegger, K., K. A. Gilmore and F. Robicheaux. (2011). Early time properties of ultracold neutral plasmas. *Journal of Physics B: Atomic, Molecular and Optical Physics*: 44 (14), 145701.
- Press, W. H., S. A. Teukolsky, W. T. Vetterling and B. P. Flannery. (1992). *Numerical Recipes*. (2). New York: Cambridge University Press.
- Rolston, S. L. (2008). Trend: Ultracold neutral plasmas. *Physics*: 1, 2.

Acknowledgments

This work was supported by a National Science Foundation grant to F. Robicheaux NSF-PHY-0903811. P. Donnan was supported by the Auburn University Undergraduate Research Fellowship Program.

Mapping Social Vulnerability for Earthquake Hazards in Salt Lake County, Utah

Ryan Hile, Philip L. Chaney

ABSTRACT

Salt Lake County, Utah, is the home of Salt Lake City and more than a million people. The Wasatch Fault, an active fault zone, runs north-south through the county and the city. Past research related to earthquake hazards in the county has utilized geological methods aimed at identifying fault geometry and recurrence. Modern hazards research, however, assesses not only natural earth processes but also the role of humans in enhancing or reducing risk to hazards. This project assesses the human component of earthquake hazards in Salt Lake County by establishing a social vulnerability index for the county. The index is composed of seven social factors: population under the age of 18, population over the age of 65, race, housing occupancy, total population, gender, and housing value. These factors represent the study population's access to resources and political power, disaster event response capability, physical/structural vulnerability, and population stress (e.g., population density or need for resources). The social factor data were combined and normalized (and given equal weight) to create an index of social vulnerability for the county. Social vulnerability within the county was generally low, with the exception of small, disconnected areas of high vulnerability within the Salt Lake City metropolitan area. The social vulnerability index created in this study identifies areas of concern as a means to improve future hazard awareness, preparedness, and mitigation practices in Salt Lake County.

INTRODUCTION

Research in natural hazards is growing in importance as people face significant change in our environment, change that often involves a major natural hazard intersecting with human life (Bogardi, 2006). A natural hazard is defined as a physical process that has the potential to affect human life and property. The impact in terms of loss of life and economic losses from natural hazards in cities around the world is growing (Tobin and Montz, 1997). As such, society needs to better understand the challenges posed by these hazards.

Hazards have been viewed historically as simple geophysical processes that occasionally burden human life and are merely a nuisance. This view, most strongly held following the industrial era of the late 1800s, has shaped hazard management policy for almost a century (Oliver-Smith, 2004). This attitude has persisted despite a major shift in how hazards were viewed by researchers in the last half century, a shift that led to acknowledgment and investigation of the connection between human systems and natural hazards (Burton et al., 1978). Subsequent decades brought new methods for assessing the human element of natural hazards, such as Blaikie's Pressure and Release model and Cutter's Hazards of Place model (Blaikie et al., 1994; Cutter, 1996). These models allowed researchers to investigate social factors that increased a region's susceptibility to harm from natural hazards. These studies ultimately seek to improve hazard management practices and protect lives and property.

EARTHQUAKE HAZARDS IN SALT LAKE COUNTY, UTAH

The study site for this research is Salt Lake County, home to Salt Lake City, the capital and most populated city in Utah. Over a million people reside in Salt Lake County, most of whom live within or in close proximity to Salt Lake City (USCB, 2012). This area faces a dire future as geophysicists have predicted that the local fault system, the Wasatch Fault, will produce a significant (magnitude 6.5 or greater), possibly surface-rupturing earthquake in the near future (UGS, 1996). Hazard studies have focused on earthquake occurrence probabilities and infrastructure loss estimates (Gori, 2000). Consequently, there remains a gap in hazard research with respect to the potential impact on society.

This project is part of a larger study to analyze the earthquake hazard in Salt Lake County based on contemporary hazards research methods. The project utilizes the social vulnerability index (SoVI) component of Cutter's (1996) Hazards of Place model. The project is an applied study of the social vulnerability of Salt Lake County, using the methods found in Cutter's (2000) work

in Georgetown County, South Carolina. In this project, a SoVI is developed for Salt Lake County to identify the most socially vulnerable locations and to determine the unique character of social vulnerability in the county. The SoVI will be utilized in future work as the social component of a place vulnerability assessment for the county.

NATURAL HAZARDS ASSESSMENT MODELS AND SOCIAL VULNERABILITY

Social vulnerability has become a significant area of study in recent years as a result of the models developed by Blaikie et al. (1994), Cutter (1996), and others. These models allow for a quantitative view of a suite of social factors that are understood to amplify hazard vulnerability, such as age, race, income, social infrastructure, and gender. These factors represent limited access to resources and political power, limited disaster response capabilities, physical vulnerability, and social infrastructure (e.g., community organization and municipal infrastructure), collectively (Blaikie et al., 1994; Tobin and Montz, 1997; Cutter et al., 2000). Across the globe, hazards researchers are seeing consistent affirmation that these factors play a major role in the impact of a natural disaster. The means by which these models address the relationship of social factors to natural hazards varies to some degree, but they all seek to determine how those factors can contribute to increased risk (described by vulnerability) or decreased risk (described by resilience) from hazards (Blaikie et al., 1994; Cutter, 1996).

Cutter's (1996) Hazards of Place model places importance on the integration of both the physical and human elements of natural hazards through the utilization of both physical vulnerability spatial models and social vulnerability spatial models. Statistical modeling is performed using a computer-based geographic information system (GIS) to identify areas of high vulnerability for

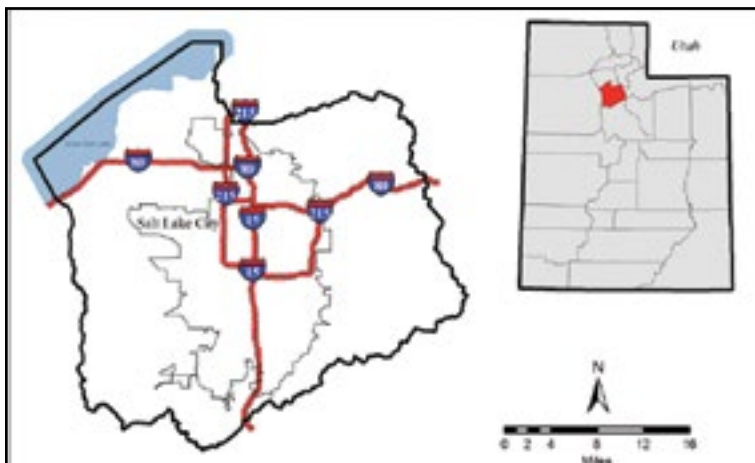


Figure 1. Salt Lake County study area (with highways, metropolitan area, and the Great Salt Lake shown). Inset shows the county's location within Utah.

both physical and social factors. These areas are combined in the GIS using spatial analysis tools to produce the Hazards of Place model, which illustrates the intersection of the human with the physical elements of vulnerability.

MAPPING SOCIAL VULNERABILITY IN SALT LAKE COUNTY, UTAH

This study utilized Cutter’s (1996) Hazards of Place model over the Blaikie et al., (1994) Pressure and Release model because the Cutter model provides a more in-depth focus on social characteristics; the Pressure and Release model emphasizes geophysical processes, while Cutter’s model gives equal consideration for geophysical processes and social factors. The specific indicators used for this study were demographic statistics from the U.S. Census Bureau for population under the age of 18, population over the age of 65, race, housing occupancy, total population, gender, and housing value (value was derived from Salt Lake County parcel data from the Salt Lake County Assessor’s office). These indices were selected on the basis of previous work (Cutter et al., 2000; Schmidlein et al., 2008).

Demographic data were collected from the Salt Lake County Assessor’s Office (parcel data for the wealth factor) and the U. S. Census Bureau. The census data consisted of TIGER shapefiles (a GIS format) of Salt Lake County’s census blocks from the main Census Bureau website and demographic tables (U.S. Census Bureau, <http://quickfacts.census.gov>). This collection of data allowed for the isolation of the seven social factors to be considered in this study’s SoVI.

The data were processed into a usable format for both GIS analysis and for the construction of the index. For all of the data from the Census Bureau, this simply involved removing extraneous data from the demographic data tables and isolating the statistics necessary for each of the specific social factors. Once the data were pared down in the tables, index scores were calculated with standardized values for each of the seven social

Table 1. Example calculation of vulnerability index score for population. Source: Adapted from Cutter et al., 2000.

Census Block	Number of People in Block	Number of People in County	Ratio of People in Block to County (a)	Population Vulnerability Score (a/max a)
1	0	1029655	0.0000	0.00
2	2503	1029655	0.0024	1.00
3	784	1029655	0.0008	0.31
4	2079	1029655	0.0020	0.83
5	1337	1029655	0.0013	0.53

factors. The index values using the census data were calculated as described below. The block value for a social factor was divided by the total county value for that factor to produce a ratio, *a*, from the block to the county, then the ratio divided by the maximum ratio value, *max a*, for all blocks to normalize the data:

$$(\text{block value}) \div (\text{county value}) = a; a \div \text{max } a = \text{index score (1)}$$

The end result of this procedure was the calculation of a standardized value for each social factor for each census block on a zero-to-one scale; zero indicates low vulnerability with increasing vulnerability to the highest value, one (Table 1).

Once the calculations were complete, the tables were attached to the census blocks. A table join was used in a GIS application to append the demographic tables to the attribute table of the census block data using the block identification number, a unique number assigned to each census block by the Census Bureau and found in both the census block data and the demographic tables.

Processing the parcel data required a different method, as the parcel data are housed in a different spatial division than the census blocks. The parcel data had to be translated to the census block which was accomplished using a spatial join function in a GIS application. This method is inherently statistically biased, however, as are all methods of

Table 2. Example calculation of vulnerability index score for wealth. Source: Adapted from Cutter et al., 2000.

Census Block	Mean Value (\$) of Housing in Block	Mean Value (\$) of Housing in County	Difference of Value (\$) of County and Block (a)	Absolute Value of a	Absolute Value of Maximum Added to a (b)	Mean Value of Housing Vulnerability Score (b/max b)
1	500	127594	127194	127194	1830085	1.00
2	19000	127594	108594	108594	1813585	0.99
3	530467	127594	-402772	402772	1900119	0.71
4	508440	127594	-380846	380846	1811445	0.47
5	1830585	127594	-1702991	1702991	0	0.00

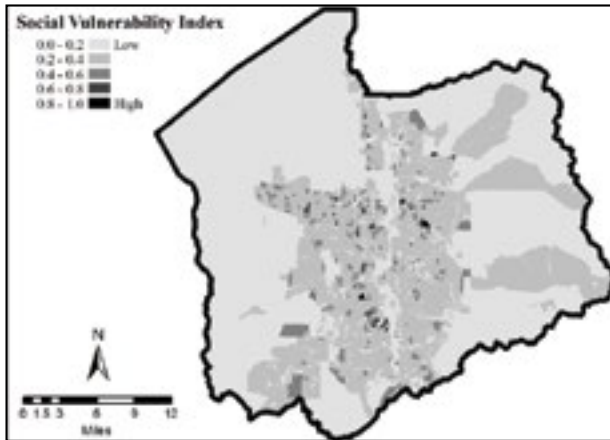


Figure 2. The social vulnerability index of Salt Lake County, Utah. Seven social factors were used to create the model: age (<18, >65), race, housing occupancy, total population, gender, and house value.

spatial areal comparisons (Openshaw, 1984). The bias comes as a result of the selection of enumeration boundaries when aggregating point data, and has been identified in the literature as the Modifiable Areal Unit Problem (MAUP) (Openshaw, 1984; Wong, 2004). The MAUP, however, has yet to have an established solution, leaving researchers in the position of having to acknowledge the issue when conducting studies with different areal divisions (Wong, 2004). The spatial join function in GIS software is a tool designed specifically to address the joining of data between different areal divisions in a bias-minimizing manner. During the join process, the software was directed to calculate the mean value of houses within each census block. The mean house value for each census block was used to calculate an index value for the wealth factor for each census block using the following calculation: the mean house value of the block was subtracted from the mean house value of the county, which

allowed for negative numbers that were removed by adding the absolute value of the maximum, $max a$, of that difference for each block. This value was divided by the maximum value of that calculation for all blocks to produce a standardized score like that for the other six factors:

$$\text{mean county value} - \text{mean block value} = a ; \frac{|max a| + a}{b} = \text{indexscore} \quad (2)$$

Once all the index values of the social factors had been calculated and attached to the census blocks, a final index-value was obtained by adding all of the index values for a census block and dividing the sum by the maximum value. This final value represents the total vulnerability, as described by the seven social factors used, for a given census block (Table 2 and Figure 2). To simplify the visualization of social vulnerability across the county, the ten classes (corresponding to the zero-to-one range of values) were compressed to five using an equal-interval method and to make the classes readily identifiable at the scale of the Figure 2.

SOCIAL VULNERABILITY CHARACTERISTICS OF SALT LAKE COUNTY, UTAH

The spatial pattern of higher vulnerability blocks (areas with an index score of ≥ 0.7) in Salt Lake County occurs within the metropolitan area of Salt Lake City in disconnected concentrations (Figure 3). These blocks are highlighted in red. The most vulnerable block, labeled 1 on Figure 3, possesses high index scores (> 0.7) in five of the seven vulnerability characteristics: a high population of

people younger than eighteen, a high proportion of females to males, a high housing occupancy, a high number of non-white individuals, and low house values. This particular block also has the highest vulnerability index value for the whole county. Another block of concern, labeled 2 on Figure 3, possesses high index scores in four of the seven vulnerability characteristics: a high population of people younger than eighteen, a high proportion of females to males, a high housing occupancy, a high number of non-white individuals. These are the only similarities between these two blocks. The other blocks in the area of interest share similar component index scores, connecting the census blocks statistically even though they do not appear to be spatially related.

Some concerns may be raised with the social factors selected, however. The major concern is the use of house value from the county parcel dataset as a metric of wealth. The value of a house can change through time, and does not necessarily reflect the owner's income. An array of situations may cause an individual to own a house that does not relate to their income level. Thus, using house value as a measure of wealth may not be an appropriate metric. That being said, it is the only publicly available data that contains spatial data possibly related to wealth and is necessary for indices, such as this vulnerability index, to aid in understanding the relative wealth of an area, as long as outlier data is considered.

CONCLUSIONS

Social vulnerability in Salt Lake County exhibits disconnected areas of high vulnerability concentration. The areas appear to be disconnected in a spatial sense, being several miles apart, though there may be other factors that link these areas. Further study is needed to enhance the SoVI to determine if there is any connection between these areas. The characteristics of vulnerability in Salt Lake County are that of a high population of

individuals under the age of eighteen, a low measure of wealth, a high number of non-white individuals, and a large number of individuals occupying a single living space. In summary, the successful creation of the SoVI gives a description to the unique nature social vulnerability in the county, which can be used to add a new dimension to the assessment of earthquake hazards in Salt Lake County.

The creation of a social vulnerability index is a necessary step for conducting contemporary hazards research. It allows social factors to be quantitatively joined to physical hazard analyses in order to describe the nature of potential disasters in a given area. On its own, the SoVI can inform about disparate social conditions in the region analyzed. Combined with physical analyses, the SoVI illustrates where human harm may occur in a natural disaster situation, which is valuable information for disaster response coordinators, planners, policy makers, and others who are involved with hazards and disasters. The SoVI described in this paper will be joined with various earthquake data to identify key areas of concern for Salt Lake County in the event of a major earthquake event.

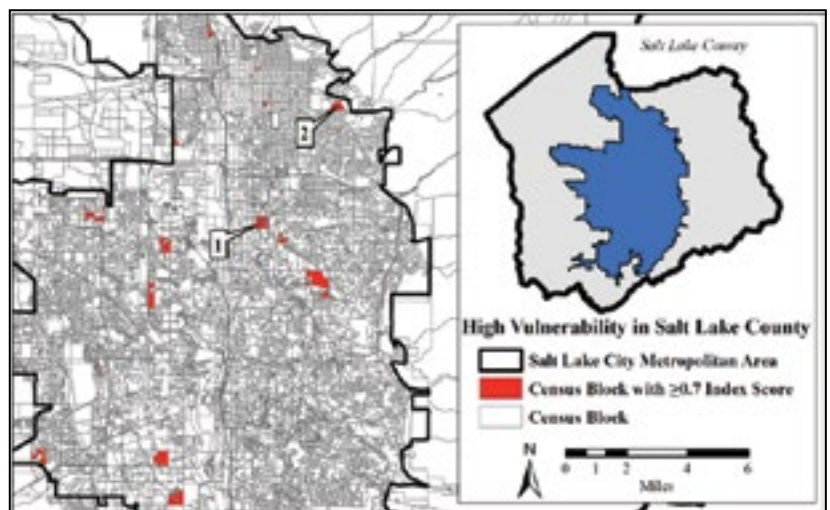


Figure 3. Census blocks with index scores ≥ 0.7 . The figure is scaled to show that all of the blocks with high vulnerability are located within the Salt Lake City metropolitan area. Numbers indicate the two census blocks with the highest vulnerability scores as discussed.

ACKNOWLEDGMENTS

Special thanks goes to Mr. Jarom Zenger with the Salt Lake County Assessor's Office for providing access to the county's parcel data for use in this project. This work was supported by the AU Undergraduate Research Fellowship Program and the Department of Geology and Geography.

REFERENCES

- Blaikie, P., T. Cannon, I. Davis, and B. Wisner. (1994). *At Risk: Natural Hazards, People's Vulnerability, and Disasters*. London: Routledge.
- Bogardi, J. J. (2006). Introduction, in J. Birkmann (Ed.), *Measuring Vulnerability to Natural Hazards*. Tokyo: United Nations University Press, 1-6.
- Buckle, P. (2006). Assessing Social Resilience, in D. Paton and D. Johnston (Eds.), *Disaster Resilience*. Springfield, IL: Charles C Thomas Publisher, LTD, 88-103.
- Burton, I., R. W. Kates, and G. F. White. (1978). *The Environment as Hazard*. New York: Oxford University Press.
- Cutter, S. L. (1996). Vulnerability to Environmental Hazards, *Progress in Human Geography*: 20(4), 529-539.
- Cutter, S. L., J. T. Mitchell, and M. S. Scott. (2000). Revealing the Vulnerability of People and Places: A Case Study of Georgetown County, South Carolina. *Annals of the Association of American Geographers*: 90 (4), 713-737.
- Gori, P. L. and W. W. Hays. (Eds.) (2000). *Assessment of Regional Earthquake Hazards and Risk Along the Wasatch Front, Utah*, Reston, VA: U.S. Geological Survey.
- Oliver-Smith, A. (2004). Theorizing Vulnerability in a Globalized World: A Political Ecological Perspective, in G. Bankoff, G. Frerks, and D. Hilhorst (Eds.), *Mapping Vulnerability: Disasters, Development, and People*. London: Earthscan, 10-24.
- Openshaw, S. (1984). *Concepts and Techniques in Modern Geography No. 38: The Modifiable Areal Unit Problem*. Norwich: Geo Books.
- Pooley, J. A., L. Cohen, and M. O'Connor. (2006). Links Between Community and Individual Resilience: Evidence from Cyclone Affected Communities in North West Australia, in D. Paton and D. Johnston (Eds.), *Disaster Resilience*. Springfield, IL: Charles C Thomas Publisher, LTD, 161-170.
- Schmidtlein, M. C., R. C. Deutsch, W. W. Piegorsch, and S. L. Cutter. (2008). A Sensitivity Analysis of the Social Vulnerability Index. *Risk Analysis*: 28 (4), 1099-1114.
- Tobin, G. A. and B. E. Montz. (1997). *Natural Hazards: Explanation and Integration*. New York: Guilford Press.
- Utah Geological Survey. (1996). *The Wasatch Fault. Public Information Series 40*. Salt Lake City, UT: Utah Geological Survey.
- U.S. Census Bureau. (2012). *Salt Lake County QuickFacts*. <http://quickfacts.census.gov>. (website accessed 6 Sept. 2012).
- Wong, D. W. S. (2004). The Modifiable Areal Unit Problem (MAUP), in D. G. Janelle, B. Warf, and K. Hansen (Eds.), *WorldMinds: Geographical Perspectives on 100 Problems*. Dordrecht, The Netherlands: Kluwer Academic Publishers, 571-575.

Effectiveness of Continuous-catch Doors for Removing Wild Pigs

Trenton N. Smith, Mark D. Smith

Abstract

Wild pigs (*Sus scrofa*) are invasive, non-native animals and their populations have increased dramatically in the United States over the past 20 years. Now found in more than 45 states, wild pigs cause over \$1.5 billion/year in crop damage nationally and over \$30 million/year of agriculture and forestry damage in Alabama. As such, private landowners, agricultural producers, and state and federal agencies have allocated significantly greater resources toward managing wild pig damage. Lethal removal, through the use of cage, corral, or box traps, remains the most cost-effective, efficient, and practical means for managing local wild pig populations. Whereas the specific dimensions of these traps may vary, trap doors typically fall into two designs: continuous-catch and single-catch. Continuous-catch doors are one-directional doors that allow additional animals to enter the trap after the door is initially triggered closed. This is achieved by door panels that swing open in one direction only, allowing animals to enter the trap but not exit. Continuous-catch doors have been advocated as the preferred door design based solely on intuitive reasoning that these doors will allow additional pigs to enter the trap after the door closes and result in a greater number of individuals being captured. However, anecdotal evidence from several professional wild pig trappers suggests continuous-catch doors rarely result in additional captures once the trap door closes. In this project, we examined the relative effectiveness of three continuous-catch door designs (root, saloon, trainer) to allow additional wild pigs to enter closed traps. This study was conducted on four sites in central and southwest Alabama during the summer of 2011. Results from data collected over only one season of one year indicate the overall entrance through closed continuous-catch doors was minimal (4.9%), refuting commonly held beliefs that these doors substantially increase capture rates of wild pigs.

Introduction

Wild pigs (*Sus scrofa*) are invasive, non-native animals and their populations have increased dramatically in the United States over the past 20 years with free-ranging populations now found in more than 45 states. Wild pig management presents a unique challenge in that pigs pose a threat not only to agricultural crop producers, but also to forest landowners, livestock producers, sportspersons through contact with diseased animals, and those tasked with managing the environmental and ecological services of natural landscapes. For example, wild pigs cause over \$1.5 billion/year in crop damage nationally (Pimental, 2007), more than \$30 million/year in Alabama (Shui et al., Auburn University, unpublished data), and over \$81 million in 2011 in southwest Georgia (Mengak, 2012). Wild pig impacts to agricultural crops include consumption, rooting, and trampling of crops such as corn, wheat, beans, peanuts, cotton, fruit trees, and small grains and rooting in pastures resulting in loss of forage and or damage to machinery (Engeman et al., 2007).

Whereas agricultural damage by wild pigs has been well documented, there exists a paucity of information regarding their impact on native flora, fauna, and ecosystems. It is presumed this damage may equal or exceed estimates of crop damage. Engeman et al. (2003a, 2003b) estimated wild pig rooting caused \$1.2 to 4.0 million in damage to unique basin wetland systems and adjacent uplands in Savannas Preserve State Park in Florida. Moreover, wild pigs have been consistently cited as one of the greatest modifiers of natural habitats (Cushman et al., 2004) negatively impacting microbial composition in streams (Kaller and Kelso, 2006), local reptile and amphibian populations (Jolley, 2007), and nest success of many ground-nesting birds (Rollins and Carroll, 2001). Wild pigs are also competitors with native wildlife for food resources such as acorns (Henry and Conley, 1972) and

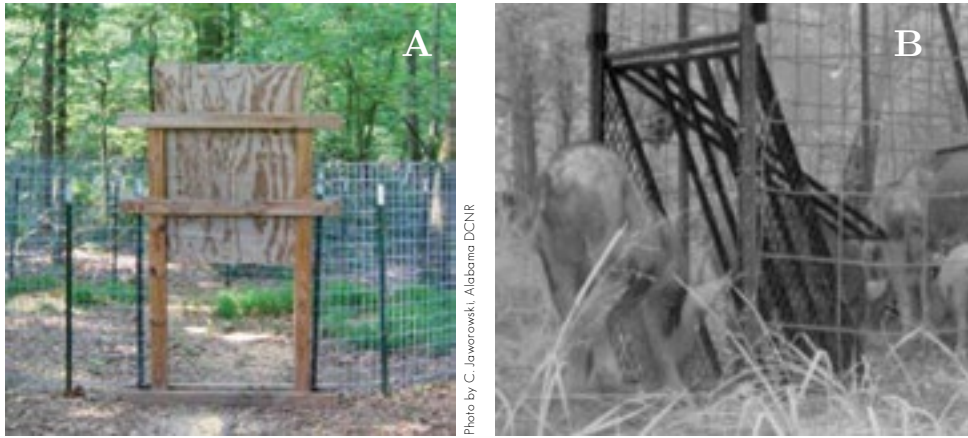


Figure 1. Examples of trap door designs: single-catch door (A) and continuous-catch door (B). When baited and set correctly, simple, wooden, single-catch doors will capture multiple pigs before the door is triggered. However, when the door is triggered and closes no more pigs may enter through single-catch doors. Continuous-catch doors (metal, hinged doors) may also catch multiple pigs before the door is triggered, but do have the potential to allow additional pigs to enter the trap after the door closes.

may displace desired wildlife species such as white-tailed deer and turkeys (Holtfreter, Auburn University, unpublished data). In forested landscapes, wild pigs may depredate hardwood seedlings (Mayer et al., 2000), suppress regeneration and sprouting of saplings (Ickes et al., 2003), and uproot seedlings (Lipscomb, 1989), in addition to rooting and trampling of recreational food plots.

Wild pigs are capable of carrying numerous diseases and parasites that may affect livestock (Corn et al., 2004, Hartin et al., 2007, Wyckoff et al., 2009), humans (Davidson, 2006), and may also serve as agents for bioterrorism (Ditchkoff and West, 2007). Swine brucellosis, pseudorabies, trichinosis, tuberculosis, vesicular stomatitis, and classical swine fever are of significant concern to livestock producers. Corn et al. (2004) reported prevalence of pseudorabies virus antibodies in 38% of wild pigs ($n = 100$) collected from 10 sites in the southeastern United States. Wyckoff et al. (2009) reported prevalence of pseudorabies and swine brucellosis antibodies in 30% and 11% of wild pigs tested in southern Texas, respectively. Although confinement operations may reduce exposure risk of domestic swine to brucellosis and pseudorabies, fenced or corralled swine may experience greater risk of exposure. Wyckoff et al. (2009) reported that 19% (7 of 37) of radio-marked wild pigs had contact with domestic pigs in Texas and found greater visitation of wild pigs to pens containing domestic swine than empty pens.

Given the magnitude and diversity of damage caused by wild pigs, many landowners and natural resource managers implement removal programs to reduce damage. Of several abatement techniques available (e.g., recreational hunting, electric fencing, opportunistic shooting, hunting with dogs), lethal removal using corral style traps is the most

cost-effective and practical means for managing local wild pig populations. As such, many aspects of wild pig trapping have been studied. For example, Williams et al. (2011a) reported corral traps having four times greater capture rates than box traps in Georgia, whereas Choquenot et al. (1993) reported that an estrous sow was ineffective at enticing trap-shy adult boars to traps. Likewise, Williams et al. (2011b) reported greater duration of feeding bouts of wild pigs at sites baited with dry whole kernel corn than soured corn or a mix of soured and dry corn. Considering the many aspects of trapping that have been evaluated, it is surprising that no studies have examined the effectiveness of frequently recommended continuous-catch doors for trapping wild pigs.

Continuous-catch doors, such as saloon and root style doors, use hinged door panels that permit one-way entry of pigs into a trap after the door initially closes, whereas single-catch doors (e.g., falling or guillotine doors), by nature of their design, do not permit entry of additional pigs into the trap after initial door closure (Figure 1). Continuous-catch doors have been advocated as the preferred door design based solely on intuitive reasoning that the ability of these doors to allow additional pigs to enter the trap once the door closes will result in greater capture rates. However, anecdotal evidence from several professional wild pig removal specialists suggests continuous-catch doors rarely result in additional captures once the trap door closes. Given the widespread use of trapping as a primary wild pig removal technique throughout the United States, coupled with the greater cost of continuous-catch doors, it is imperative that natural resource professionals tasked with wild pig removal understand the relative costs and benefits of these door types when allocating resources within removal programs.

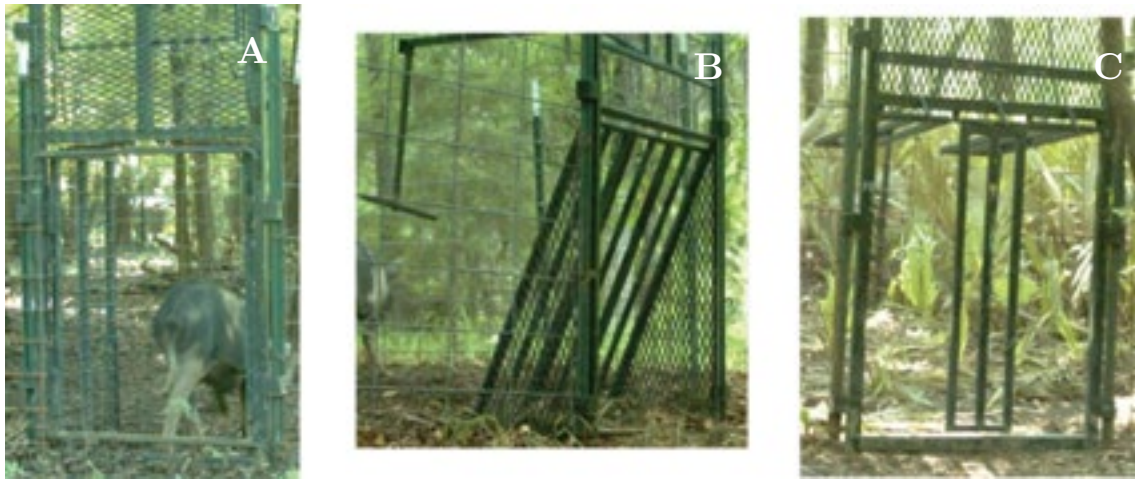


Figure 2. Saloon (A), root (B), and trainer (C) continuous-catch trap door designs evaluated in this study. All three doors function by hinged panels that allow pigs to enter after the door has shut, but not to exit. Saloon doors are the simplest design with two horizontally hinged panels (open in) with springs to close the door behind the pig after it enters. Root doors have three vertically hinged panels (open up) that when closed are slightly inset to potentially guide the pigs to the opening. Trainer doors are also made up of three vertically hinged panels. They are unique in that you may remove the stop at the bottom and allow pigs to enter and exit through the door (freely) so that they might become accustomed or "trained" to push open the closed door before setting the trap.

Although both trap door designs (continuous- and single-catch) will effectively capture wild pigs when used properly, the cost of steel or aluminum continuous-catch doors (approximately \$300) is significantly greater than that of simple wooden single-catch doors (approximately \$40). This cost differential equates to approximately the price for one complete three-panel corral trap with a wooden single-catch door. Because total trap cost is frequently the primary factor driving the number of traps a landowner may construct and use (the financial investment), and the type of trap door used will significantly influence this cost, it is important to determine whether or not the added expense of continuous-catch doors will result in greater capture rates. If capture efficiency is similar between door types (i.e., no additional pigs enter through continuous-catch doors once the door closes) it would be beneficial to reallocate financial resources to the construction of additional traps with single-catch doors rather than a single trap with a continuous-catch door. Therefore, the objective of this study was to evaluate the capture efficiency of three commonly recommended continuous-catch doors designs.

Study Area and Methods

We evaluated the capture efficiency of saloon, root, and trainer door designs (Figure 2) on four study sites in central and southwest Alabama during summer of 2011. We used standard three-panel (16'x 5' livestock panel) corral traps throughout the study (Figure 3). We pre-baited trap sites with whole kernel corn for approximately one week during which we used one motion-sensitive trail camera to determine

the number of pigs and to identify individuals in the sounder (a family unit of pigs). Once the sounder size was determined and all individuals within the sounder were conditioned to entering a trap, we began our capture trial. In the late afternoon, we set the trap to capture only a portion of a sounder by placing most of the bait near the triggering mechanism positioned a short distance inside the trap (Figure 3). We used this approach to ensure that several pigs of the sounder were not captured and thus left outside the trap after the door closed. Lastly, we placed two motion-sensitive trail cameras, one at the front and one at the side of each trap, to record the activity of the pigs remaining outside of the trap.

We checked the traps approximately 16 hours after setting. We photographed and identified all captured pigs by sex, age class (adult or juvenile), and markings to allow for cross-verification of individuals within a sounder. Then we released the pigs from the trap and removed the memory cards from the game cameras to upload the images to a computer. After the capture trial, we reviewed images to determine the number of pigs initially captured, number of pigs outside the trap when the door closed (number of pig opportunities), number of entry attempts (a pig making physical contact with the door), number of pigs entering through closed doors, amount of time spent around the trap by non-captured individuals, and the number of visits to the trap by non-captured pigs during the capture trial. We then tallied the data by door type to determine the relative capture efficiency of saloon, root, and trainer doors.

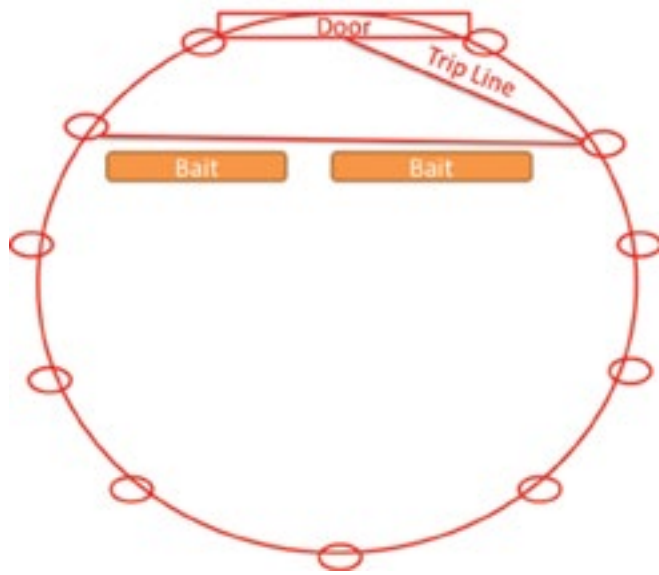


Figure 3. Three-panel corral-style trap design used in the experiment. Traps were set to intentionally capture only part of the sounder by placing the bait and trigger (trip line) near the entrance of the trap to ensure that the first few individuals to enter would trigger the trap and the rest of the sounder would remain outside. Two motion-sensitive cameras were placed near the trap entrance and side to observe whether the individuals left outside of the trap entered the closed door during the capture trial.

Results

Overall, we observed a total of 239 unique individuals from 24 sounders with a mean sounder size of nine individuals from more than 40,000 game camera images. On average, we captured about 50% of each sounder during a capture trial. We obtained data from 37 capture trials where pigs were captured and other pigs remained outside of the trap after the door closed. Of these capture trials, we observed 222 pig opportunities (individual pigs outside the trap after the door closed; saloon: $n=115$, root: $n=55$, trainer: $n=52$). Pigs outside the trap on average made two visits per capture trial to traps with a mean time per visit of approximately one hour. We also observed an event where a pig opened a root door from inside the trap allowing it and three others to escape. Overall, we observed entry rates (entries through closed doors/pig opportunities) of 16.4% ($n=9$), 0.9% ($n=1$), and 1.9% ($n=1$) through closed root, saloon, and trainer doors, respectively.

“...wild pigs cause over \$1.5 billion/year in crop damage nationally and over \$30 million/year of forestry and agriculture damage in Alabama.”

Discussion

Our purpose was to evaluate the ability of continuous-catch doors to capture additional wild pigs after the door closes. Considering the number of opportunities that pigs had to enter closed doors ($n=222$) and the exceptionally low number of individuals that successfully entered ($n=11$), we conclude that continuous-catch doors were not effective at capturing substantial numbers of additional pigs after the trap door initially closed (less than 5% of pig-opportunities overall). This is further supported by the extensive amount of time spent outside the trap and number of visits made by pigs after the door closed. Pigs averaged approximately one hour per visit and made two or more visits per trap night. Some individuals even bedded around the trap, staying there for most of the night. It was apparent that the pigs were motivated to enter the trap, but did not. Root doors did have a much greater capture rate (16%) than both saloon and trainer doors (less than 2%). However, capturing approximately 16% of the pigs remaining outside of the trap is marginal considering that when baited correctly, the majority of the individuals will already be inside the trap with only a few remaining outside.

This information is critical to wildlife managers, agricultural producers, and landowners, considering the difference in cost and construction of continuous-catch doors and single-catch doors as described above. Because the benefit of continuous-catch doors (capturing additional pigs) over single-catch doors was minimal in comparison to the difference in cost (more than \$200), we recommend that landowners allocate resources instead to additional traps and place greater emphasis on other technical aspects of trapping (e.g., proper bait placement, patience, minimizing negative stimuli, etc.) to maximize capture rates rather than a reliance upon continuous-catch doors.

References

- Choquenot, D., R. J. Kilgour, and B. S. Lukins. (1993). An evaluation of wild pig trapping. *Wildlife Research* 20:15-22.
- Corn, J. L., D. E. Stallknecht, N. M. Mechlin, M. P. Luttrell, and J. R. Fischer. (2004). Persistence of pseudorabies virus in feral swine populations. *Journal of Wildlife Diseases* 40:307-310.
- Cushman, J. H., T. A. Tierney, and J. M. Hinds. (2004). Variable effects of feral hog disturbances on native and exotic plants in a California grassland. *Ecological Applications* 14:1746-1756.
- Davidson, W. R., (Ed). (2006). Wild swine. *Field Manual of Wildlife Diseases in the Southeastern United States*. Third edition. Southeastern Cooperative Wildlife Disease Study, Athens, GA.: 105-134.
- Ditchkoff, S. S., and B. C. West. (2007). Ecology and management of feral hogs. *Human-Wildlife Conflicts* 1:149-151.
- Engeman, R. M., H.T. Smith, R. G. Severson, M.A.M. Severson, S. A. Swift, B. Constantin, and D. Griffin. (2003a). Amount and economic valuation of feral hog damage to a unique basin marsh wetland in Florida. USDA National Wildlife Research Center - Staff Publications. Paper 217. http://digitalcommons.unl.edu/icwdm_usdanwrc/217.
- Engeman, R. M., H. T. Smith, S.A. Shwiff, B. Constantin, J. Woolward, M. Nelson, and D. Griffin. (2003b). Prevalence and economic value of feral swine damage to native habitat in three Florida state parks. *Environmental Conservation* 30:319-324.
- Engeman, R. M., J. Wollard, H. T. Smith, J. Bourassa, B.U. Constantin, and D. Griffin. (2007). An extraordinary patch of feral hog damage in Florida before and after initiating hog removal. *Human-Wildlife Conflicts* 1:271-275.
- Hartin, R. E., M. R. Ryan, and T. A. Campbell. (2007). Distribution and disease prevalence of feral hogs in Missouri. *Human-Wildlife Conflicts* 1:186-191.
- Henry, V. G., and R. H. Conley. (1972). Fall foods of European wild hogs in the southern Appalachians. *Journal of Wildlife Management* 36:854-860.
- Ickes, K., S. J. DeWalt, S. C. Thomas. (2003). Resprouting of woody saplings following stem snap by wild pigs in a Malaysian rain forest. *Journal of Ecology* 91:222-233.
- Jolley, D. B. (2007). *Reproduction and Herpetofauna Depredation of Feral Hogs at Fort Benning, Georgia*. M. S. Thesis, School of Forestry and Wildlife Sciences, Auburn, Alabama, USA: Auburn University.
- Kaller, M. D., and W. E. Kelso. (2006). Swine activity alters invertebrate and microbial communities in a coastal plain watershed. *American Midland Naturalist* 156:163-177.
- Lipscomb, D. J. (1989). Impacts of feral hogs on longleaf pine regeneration. *Southern Journal of Applied Forestry* 13:177-181.
- Mayer, J. J., E. A. Nelson, and L. D. Wike. (2000). Selective depredation of planted hardwood seedlings by wild pigs in a wetland restoration area. *Ecological Engineering*: 15:S79-S85.
- Mengak, M. T. (2012). 2012 Georgia wild pig survey final report. University of Georgia Cooperative Extension Wildlife Management Series Publication: WMS-12-16.
- Pimental, D. (2007). Environmental and economic costs of vertebrate species invasions into the United States, in G. W. Witmer, W. C. Pitt, and K. A. Fagerstone (Eds.), *Managing Vertebrate Invasive Species: Proceedings of an International Symposium*. Fort Collins, Colorado: USDA APHIS Wildlife Services, National Wildlife Research Center, 2-8.
- Rollins, D., and J. P. Carroll. (2011). Impacts of predation on northern bobwhite and scaled quail. *Wildlife Society Bulletin* 29:39-51.
- Williams, B. L., R. W. Holtfreter, S. S. Ditchkoff, and J. B. Grand. (2011a). Trap style influences wild pig behavior and trapping success. *Journal of Wildlife Management* 75:432-436.
- Williams, B. L., R. W. Holtfreter, S. S. Ditchkoff, and J. B. Grand. (2011b). Efficiency of time-lapse intervals and simple baits for camera surveys of wild pigs. *Journal of Wildlife Management*: 75:655-659.
- Wyckoff, A. C., S. E. Henke, T. A. Campbell, D. G. Hewitt, and K. C. VerCauteren. (2009). Feral swine contact with domestic swine: a serologic survey and assessment of potential for disease transmission. *Journal of Wildlife Management* 45:422-429.

Acknowledgments

This study was funded by the ALFA-Alabama Farmer's Federation and the Auburn University Undergraduate Research Fellowship Program with in-kind contributions from USDA Wildlife Services. D. Beaty, C. Leikvold, V. Langley, and H. Young with USDA Wildlife Services provided substantial in-field support. We thank K. Causey, J. Collet, J. Crowder, J. Hall, D. Harrell, P. Hollis, R. Pierce, F. Thomas, and the Upper State Game Sanctuary of the Alabama Department of Conservation and Natural Resources for property access and field support.

GENERATION OF LIQUID FUEL MICRODROPLETS FOR COMBUSTION IMAGING

STEPHEN GILES, VIGNESH VENKATASUBRAMANIAN, JINGRAN DUAN, STEVE R. DUKE

ABSTRACT

To perform a comparative study of traditional and alternative fuel combustion, microdroplets of liquid fuels are injected into a laboratory-scale drop-tube furnace where their combustion is imaged at high speed and high magnification. This paper describes the development of a device that generates and ejects microdroplets of fuels of interest. The integral components of the droplet generator are a piezoelectric disc that bends when a voltage is applied to it and a small-diameter ejection nozzle. Various conditions, such as amplitude and frequency of the voltage signal, are controlled which in turn allows for control of droplet size in fluids with a wide range of rheological properties (e.g., viscosity, surface tension, and density). Studies were conducted to determine drop size ranges for a number of fluids. For glycerin, a fluid of particular interest for this study, the device was shown to produce droplets in the range of 200-400 μm . Preliminary images are presented showing combustion of microdroplets of glycerin ejected into the drop-tube furnace and cetane, which serves as a traditional fuel comparison.

INTRODUCTION

Due to the negative environmental impacts and costs of fossil fuels, various renewable alternative fuels and energy sources have been under study in recent decades. One possible alternative source of energy receiving consideration is glycerin. A byproduct from both the production of biodiesel and the saponification of vegetable oils, glycerin is a waste fuel which has been shown to be a viable energy source for use in modified diesel engines (Rattray, 2006; Nichols, 2011), swirl burners (Metzger, 2007), etc. Due to the steady increase in production of biodiesel, by the end of this decade the amount of crude glycerin

by-product is expected to increase to over 400 million liters per year (Hao, et al., 2010).

In most liquid fuel systems, the fuel is atomized prior to undergoing combustion. This process facilitates vaporization of less volatile liquid fuels as combustion is a vapor-phase reaction process (Joyce, 1949). Previous studies on atomization sprays for combustion applications revealed that sprays have mean droplet sizes of 100-200 μm (Santoro, 1997; Nam and Alvarado, 2012). To understand the combustion of an atomization spray and how operating parameters affect combustion properties and effectiveness, our approach was to study the combustion of individual fuel microdroplets. To investigate and compare the combustion properties of glycerin to traditional fossil fuel components (e.g., iso-octane, cetane), visualizations were obtained of microdroplets for each liquid fuel undergoing combustion in a laboratory-scale drop-tube furnace. This paper presents the development of the liquid microdroplet generation and ejection system.

There are several actuation methods, such as pneumatic, piezoelectric, thermal bubble, acoustic-wave, electrostatic, and others, which can produce microdroplets of consistent sizes (Gad-el-Hak, 2005). Piezoelectric actuation provides a reliable, cost-effective way to generate microdroplets

in a "drop-on-demand" manner similar to that used in ink-jet printers. Previous research has demonstrated that microdroplets of 50% aqueous glycerin were successfully generated by a piezoelectric droplet generator (Ulmke, et al., 2001). However, due to the high viscosity of glycerin, microdroplet ejection is often limited (Lee, 2002; Fan, et al., 2008).

EXPERIMENTAL METHODS

The Droplet Ejector

The piezoelectric droplet ejector was primarily constructed according to research performed on a microdroplet generator used for filling liquid crystal display (LCD) micro-arrays (Fan, et al., 2008). This method included the fabrication of a glass ejection nozzle from which the microdroplets were ejected and the construction of the stainless steel body of the droplet ejector which housed the piezoelectric disk and contained the test liquid. A Teflon gasket at the base of this main body provided a secure attachment for the glass ejection nozzle. Figure 1a shows a diagram of the droplet ejector components. Figure 1b shows the disassembled droplet ejector. The test liquid was pumped at a constant flowrate through the liquid inlet by a KDSScientific Model 210 syringe pump.

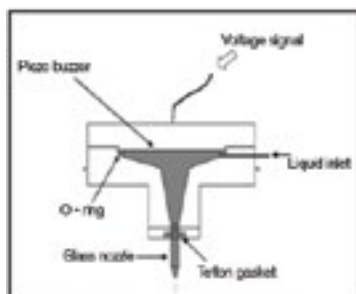


Figure 1a. Schematic of droplet ejector.



Figure 1b. Disassembled droplet ejector.

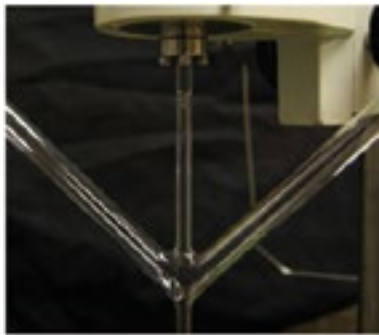


Figure 2a. Liquid fuel injection nozzle.

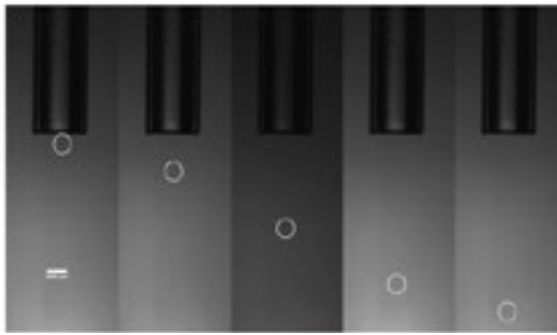


Figure 2b. 50% aqueous glycerin microdroplets being falling through the injection nozzle. Operating conditions: 55 V, 3.0 Hz, constant glycerin flowrate of 0.01 $\mu\text{L}/\text{min}$ – images captured at 143 frames per second.

The piezoelectric component used was a disc bender from APC International, Ltd. The disc has a diameter of 27 mm, overall thickness of 0.45 mm, and is composed of a single layer lead zirconate titanate (PZT) ceramic with an electrode on brass. To enable a voltage signal to be applied to the disc, a wire was soldered onto the central ceramic portion of the disc. When secured within the stainless steel body of the droplet ejector, a rubber O-ring provided a tight seal between the liquid reservoir and the piezoelectric disc.

The voltage signal, which is responsible for bending the piezoelectric disc, originates from a BK Precision 5 MHz function generator, Model 4011. The waveform was then sent through a Tegam Model 2340 high-voltage amplifier, with a gain of $\times 50$. The amplified voltage signal was transferred to the piezoelectric disc via an alligator clip connection. The voltage signal was monitored with a BK Precision 20 MHz oscilloscope, Model 2120B.

Imaging Equipment and Analysis

To image the microdroplets, a Cooke PCO 1200 HS 10-bit CMOS camera was used with a Nikon AF-S Micro Nikkor 105 mm lens. To aid in the image capture of the microdroplets, a Monarch Nova-Strobe stroboscope was used along with a light dispersion panel. After recording images via the PCO software, the images were analyzed

via ImageJ, a Java image analysis software. Because the PCO camera is capable of high-speed imaging, multiple images of the same microdroplet were recorded. The diameter of a microdroplet was estimated by taking the average of the measurements obtained for the microdroplet in each image in which it appeared.

Pendant Droplet Combustion Studies

The laboratory-scale drop-tube furnace environment allows for the study of a free-falling droplet in a dynamic environment, often referred to as the “falling drop technique” for combustion studies (Bolt, 1955). The drop-tube furnace used in these studies was developed by the Duke research group and has been used for studies with alternative solid fuels (Huang, 2010). Slight modifications were made to the fuel injection portion of the furnace apparatus in order to better accommodate the study of liquid fuels. The injection nozzle which was developed for use with liquid fuels is shown in Figure 2a. Microdroplets successfully being ejected from the nozzle are shown in Figure 2b. For the combustion experiments, the furnace was heated to 900 °C. This temperature was chosen because it is a common operating temperature for the pre-heaters of kilns in cement manufacturing (Huang, 2010; Karstensen, 2010). Visualization can be obtained for pendant droplet combustion

occurring in the drop-tube furnace environment. We are currently working on obtaining similar combustion images for falling microdroplets.

EXPERIMENTAL RESULTS

Microdroplet Characteristics

It was hypothesized that drop diameter, drop consistency, and other important microdroplet characteristics would be strong functions of the voltage applied to the piezoelectric disc bender. In Figure 3, drop diameter is plotted as a function of voltage for several aqueous solutions of glycerin. The lowest concentration of glycerin, a 50% aqueous solution, consistently exhibited the largest droplet diameters. The explanation for this result is primarily that water has a higher surface tension than glycerin. In general, higher surface tension will tend to cause larger microdroplets to be formed. However, other important rheological differences between water and glycerin (viscosity, density, etc.) and the effects of operating at higher voltages will cause drop diameter to vary non-linearly over the range of voltage driving forces. It is seen from Figure 3 that the largest drop diameter occurs at the condition of 37.5 V. Under conditions of high voltage (i.e., ≥ 50 V), it was observed that monodisperse droplet ejection often ceases. Instead, the ejector forms microdroplets in an unstable manner. In this unsteady operating mode, the ejector

tends to spray multiple microdroplets instead of ejecting a single microdroplet with each voltage pulse. The images and measurements for multi-drop ejections showed a decrease in average diameters; however, a larger total volume of microdroplets were ejected. For each voltage tested, 60 microdroplets were imaged to determine the average microdroplet diameter for that particular voltage.

Combustion in Furnace Environment

Figure 4a shows an image obtained for the combustion of a 70% aqueous glycerin pendant droplet at a furnace setting of 900 °C. Similarly, Figure 4b depicts the combustion of a cetane pendant droplet at 800 °C. Combustion experiments for cetane were performed at a lower temperature in order to delay combustion from occurring until the cetane droplet entered the furnace. While the visualization studies are still in preliminary stages of development, the expected differences between the combustion of glycerin and cetane can be qualitatively observed. At a furnace operating temperature of 100 °C less than the temperature used to combust 70% glycerin, cetane exhibits a comparatively more vigorous combustion both in terms of brightness of flame and time required to combust. This difference is mainly attributable to the comparatively lower volatility and higher flash point

temperature of glycerin. The images reveal the potential of combustion visualization to understand fuel performance and studies of free-falling microdroplets of liquid fuels produced with the ejector described in this paper are underway.

CONCLUSIONS

A piezoelectric droplet ejector for generating microdroplets of liquid fuels was developed and was capable of producing microdroplets on demand for fuels with various rheological properties. The diameters for glycerin microdroplets were shown to range from 200 to 400 μm in diameter. Microdroplet diameter increased with voltage under stable, monodisperse droplet ejection. At high voltages applied to the droplet ejector, multiple microdroplets were ejected. Combustion images for pendant droplets in a drop-tube furnace show that cetane undergoes more vigorous combustion than glycerin. For future work, our research group will be using the visualization methods to estimate temperature distributions and dynamics for the fuels undergoing combustion.

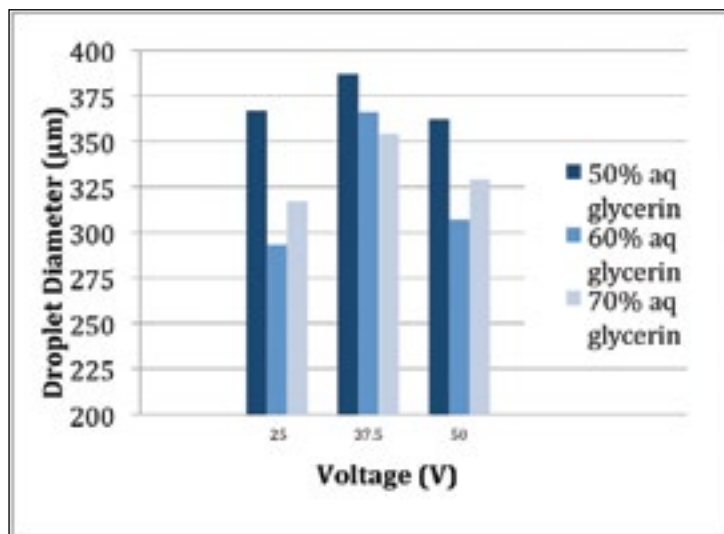


Figure 3. Microdroplet diameter measurements of 50%, 60%, and 70% aqueous glycerin at various voltages. A voltage frequency of 3.5 Hz, and a flowrate of 10 μL/min were used. Sixty droplets were imaged for each voltage to determine the average diameter.



Figure 4a. Combustion of 70% aqueous glycerin pendant droplet at 900 °C.



Figure 4b. Combustion of cetane pendant droplet at 800 °C.

ACKNOWLEDGMENTS

US Department of Energy, Biomass Program. Auburn University Undergraduate Research Program, Wendell Sandlin and Matt Montgomery from the Auburn University Glass Shop. Brian Schweiker of the Auburn University Machine Shop.

REFERENCES

- Bolt, J. A., T. A. Boyle, and W. Mirsky. (1995). The generation and burning of uniform-size liquid fuel drops. *University of Michigan Engineering College Industry Program*.
- Fan, K. C., J. Y. Chen, C. H. Wang, and W. C. Pan. (2008). Development of a drop-on-demand droplet generator for one-drop-fill technology. *Sensors and Actuators A: Physical*: 147 (2): 649-655.
- Gad-el-Hak, M. (2006). *The MEMS Handbook, Second Edition*. Boca Raton, FL: CRC Press.
- Hao, S., W. Peng, N. Zhao, F. Xiao, W. Wei, and Y. Sun. (2010). Hydrogenolysis of glycerol to 1,2-propanediol catalyzed by Cu-H4SiW12O40/Al2O3 in liquid phase. *Journal of Chemical Technology and Biotechnology*: 85 (11): 1499-1503.
- Huang, A. (2010). *The Design and Application of a Drop Tube Furnace for Visualization of Combustion of Alternative Fuel Particles*. M. S. Thesis, Auburn University.
- Joyce, J. R. (1949). The Atomization of liquid fuels for combustion. *Journal of the American Society of Naval Engineers*: 61(3): 650-663.
- Karstensen, K. H., A. M. Mubarak, H. N. Gunadasa, B. Wijagunasekara, N. Ratnayake, N., A. De Alwis, and J. Fernando. (2010). Test burn with PCB-oil in a local cement kiln in Sri Lanka. *Chemosphere*: 78 (6): 717-723.
- Lee, E. R. (2002). *Microdrop Generation*. Boca Raton, FL.: CRC Press.
- Metzger, B. (2007). *Glycerol Combustion*. Ph. D. Dissertation, North Carolina State University.
- Nam, H. and J. L. Alvarado. (2012). Microexplosion detection in hexadecane and vegetable oil blends. *Spring Technical Meeting of the Central States Section of the Combustion Institute*: 1: 1310-1319.
- Nichols, W. (2011, August 3). "Is glycerine primed to end fossil fuel domination?" <<http://www.businessgreen.com/bg/news/2098800/glycerine-primed-fossil-fuel-domination>>. (website accessed 23 Sept. 2012).
- Rattray, J. B. (2006) Glycerin – how sweet it is. *International News on Fats, Oils, and Related Materials*: 17 (5): 285.
- Santoro, R. J. (1997). High pressure combustion studies under combustion-driven oscillatory flow conditions. Final report, *Air Force Office of Scientific Research*. Washington, D.C.: Air Force Office of Scientific Research.
- Ulmke, H., M. Mietschke, and K. Bauckhage. (2001). Piezoelectric single nozzle droplet generator for production of monodisperse droplets of variable diameter. *Chemical Engineering and Technology*: 24 (1): 69-70.

Student Author Bios

Gabrielle Bates

Senior in Creative Writing, Department of English

As an intern for the Auburn Office of University Writing, Gabrielle Bates was given the opportunity to look behind the scenes at some of the exciting opportunities offered to undergraduates by *AUJUS*. After graduating from Auburn, Bates plans to get an MFA in Creative Writing and then pursue her long-term goals of traveling, publishing novels, and teaching English courses at the collegiate level.



Kaitlyn Caraway

Junior in Animal Sciences/Pre-veterinary, Department of Animal Sciences

Kaitlyn initially became interested in research while working in the parasitology lab at the Auburn University College of Veterinary Medicine (AUCVM). This led her to pursue a project with Dr. Robyn Wilborn in the Department of Clinical Sciences at the AUCVM that involved quantifying the concentration of canine spermatozoa using multiple methods. She has recently applied to the AUCVM to pursue a career as a veterinarian.



Patrick Donnan

Senior in Physics and Music, Department of Physics and Department of Music

Patrick became involved with research during the first week of his freshman year at Auburn. He has worked on projects related to the Antihydrogen Laser Physics Apparatus (ALPHA) experiment located at CERN since then. He hopes to continue with research for the rest of his life and intends to pursue a Ph.D. in theoretical atomic physics following the completion of his undergraduate work. He hopes to one day be a physics professor and mentor undergraduates in research.



Heather Eggleston

Senior in Chemistry, Department of Chemistry

In the summer of 2012, Heather interned in the SUCCESS program at The Ohio State University where she worked with Dr. Daniel Wozniak to determine the pathoadaptation of *Pseudomonas aeruginosa*. Inspired by her experience in microbiological research, Heather now works with strains of *Staphylococcus aureus* and *Streptococcus pyogenes* in the lab of Dr. Peter Panizzi in the Department of Pharmacal Sciences. After graduating in May 2013, she plans to attend graduate school in pursuit of a joint MD/Ph.D degree in order to investigate infectious disease in the elderly and immune compromised.

Stephen Giles

Senior in Chemical Engineering, Department of Chemical Engineering

Stephen is currently writing an undergraduate Honors thesis which explores combustion properties of alternative liquid fuel microdroplets. Stephen is also working on the use of cellulose nanocrystal thin films for next-generation, low-cost microelectromechanical systems. He is a 2011-2012 Auburn University Undergraduate Research Fellow, a 2012 National Science Foundation Research Experiences for Undergraduates Fellow at Clemson University, and won 2nd place for a poster presentation at the 2012 American Institute of Chemical Engineers National Conference.

Yvette Jones

Senior in History, Department of History

Yvette has been interested in history for the majority of her life and entered Auburn as a history major. Classes and conversations with her professors have inspired her to pursue academic history, and her current research interests focus on gender, crime, and law in the sixteenth and seventeenth century Atlantic world. After graduating in May 2013, she plans to attend graduate school to pursue her Master's degree and eventually her Ph.D. She has many goals for the future, some of which include traveling, researching, and possibly working in education.



Student Author Bios

William Grant Kirkland

Senior in Mechanical Engineering, Department of Mechanical Engineering

Grant is currently serving as president of the Mechanical Engineering Honor Society and the Society of Tribology and Lubrication Engineers. He will graduate in spring 2013 with a Bachelor's degree in Mechanical Engineering and a minor in Nuclear Power Generation Systems. In the fall, he plans to pursue a Master's degree with a focus on dynamic systems and control theory at Auburn University.



Trenton Smith

Recent Graduate in Wildlife Sciences, School of Forestry and Wildlife Sciences

Trent has had a passion for the outdoors and wildlife since he was a young child. He knew before he arrived at Auburn University that he wanted to study wildlife and manage their populations and habitats for the good of the public and the ecosystem. Therefore, Trent jumped at the opportunity to perform undergraduate research with Dr. Mark Smith and Dana Johnson studying wild pig trapping methods. He is grateful for this experience and for the doors it has opened up for him. Trent is currently in graduate school at the University of Missouri researching elk resource selection and food habits. After receiving his Master's degree, he hopes to pursue a career as a wildlife biologist conducting and implementing research for wildlife conservation.



William McGinnis

Senior in Mechanical Engineering, Department of Mechanical Engineering

Having raced extensively as an elite cyclist, Will McGinnis found cycling to be a natural application for his work. He seeks to use commonly available equipment to estimate dynamic parameters of cyclists. Extensions of this work have led to his development of commercial software and the application of these techniques to automobiles. He plans to attend graduate school after graduating in 2013. He is interested in developing a comprehensive model for enhancement of artificial joints.



Jacob Neil Wadkins

Senior in Biosystems Engineering, Department of Biosystems Engineering

Jacob became interested in renewable energy technologies and research after taking Dr. Fasina's Renewable Energy in Biosystems Process Operations course. This course led him to his research of biomass gasification and more specifically the methods by which the process may be optimized by inducing reliable flow of biomass materials from holding and storage containers. After graduating in May 2013, Jacob's immediate goal is to obtain a position associated with renewable energy, and he is contemplating further education and research at graduate school.



Kimberly Roberts

Senior in Animal Sciences/Pre-veterinary, Department of Animal Sciences

Kimberly is currently writing her undergraduate Honors thesis centered on her research on neonatal uterine development in pigs. She has participated in the AU Cellular and Molecular Biosciences Undergraduate Summer Research Scholars program, and won Best Undergraduate Poster at the 2012 AU Phi Zeta Research Emphasis Day. In addition to her research, she spent one month studying abroad in Belize, and is an Undergraduate Teaching Assistant for Anatomy and Physiology labs. Kimberly is looking forward to pursuing joint degrees in Veterinary Medicine and Public Health this coming year.



AUJUS

Auburn University Journal of Undergraduate Scholarship



AUBURN
UNIVERSITY



UNDERGRADUATE
research
Set Yourself Apart.

The *Auburn University Journal of Undergraduate Scholarship* (AUJUS) is currently accepting scholarly articles for its third issue in Spring 2014.

AUJUS is a refereed journal that showcases the top research and scholarly accomplishments of Auburn University undergraduate students.

Details at www.auburn.edu/undgres/aujus.html

For more information, contact undgres@auburn.edu

Call for Submissions



AUBURN
UNIVERSITY

AUJUS

Auburn University Journal of Undergraduate Scholarship

Undergraduate Research
Office of the Provost
102 Cater Hall
Auburn, AL 36849

